

# **IMPACT BEHAVIOR OF TEXTILE REINFORCED CONCRETE SLABS**

**A Thesis Submitted to  
the Graduate School of Engineering and Sciences of  
İzmir Institute of Technology  
in Partial Fulfillment of the Requirements for the Degree of**

**DOCTOR OF PHILOSOPHY**

**in Civil Engineering**

**by  
Baturay BATARLAR**

**March 2021  
İZMİR**

## ACKNOWLEDGMENTS

This study is composed of two main investigations; experimental and numerical parts. The experimental part was accomplished by using testing facilities at Otto-Mohr Laboratorium of Technische Universität Dresden. To do that, I was supported by the Scientific and Technological Research Council of Turkey (TÜBİTAK) under the grant of 2214/A.

The pathway of my Ph.D. has been quite challenging to me, and the duration of this journey was higher than I expected. During my studies, many people helped me out with their presence and constant supports.

First of all, I would like to thank my supervisor Asst. Prof. Dr. Selçuk Saatçı. He has been always supporting and encouraging me not only academically, but also personally in this journey. It's been a great pleasure and honor to me that I could find a chance to be his student during my graduate studies.

I would like to thank the professors of my dissertation committee, Assoc. Prof. Dr. Cemalettin Dönmez and Prof. Dr. Eray Baran. They gave invaluable support and guidance for this thesis. Also, special thanks go to professors of my defense jury, Assoc. Prof. Dr. Gürsoy Turan and Prof. Dr. İhsan Engin Bal for their advice, comments, and scientific insight.

As I mentioned earlier, this Ph.D. study was a long haul than expected, and so many people made this journey bearable. Firstly, I would like to thank my colleagues, Egemen Sönmez, Alper Çankaya, Mustafa Karaman, Mustafa Vardaroğlu, and Vedat Şenol for a lot of memories and moments we shared.

Impact tests on slabs were conducted at Technische Universität Dresden with the help of many people. Firstly, I would like to thank Univ.-Prof. Dr.-Ing. Dr.-Ing. E.h. Manfred Curbach. He gave me a chance to work in TU Dresden with great researchers and colleagues. Also, I would like to thank Marcus Hering, Franz Bracklow, Tino Kühn, and Petr Máca. Piercing the slabs was quite joyful with them. Very special thanks go to Dr.-Ing. Birgit Beckmann. She put the enormous effort from the very beginning without knowing me personally. The tests could not be realized without her support. I know that I cannot thank her enough. I appreciate every single effort she made for me.

During my education, my family put a lot for me to make me reach my goals in my life. Their endless support made this story possible. I am very thankful to my parents, sister, and brother-in-law for walking this path with me.

And lastly, I am thankful to the one who has been standing with me for all these years from childhood to today. I cannot find a proper word to describe; first a childhood crush, then a high school lover, later on, a close friend, and now a wife. I am deeply grateful to my wife, Hande, who has been always giving her best for me. I am very thankful to you for not only being a patient spouse during this journey but also a friend, a guide, an academic mentor, and support to lean on. Besides many things learned from you, you taught me how to live to fight another day. I appreciate every single moment that I am with you. These pages could not be written without your unconditional love.

# ABSTRACT

## IMPACT BEHAVIOR OF TEXTILE REINFORCED CONCRETE SLABS

Reinforced concrete (RC) technology is still the most preferable and common method to build civil engineering structures. In accordance with design purposes and needs, these structures are built to resist various loading scenarios. Throughout the lifespan of RC structures, they may be subjected to high rate loading scenarios due to either expected or unexpected reasons such as impacts caused by vehicular collisions, debris generated by typhoons, tsunami or floods, rock or object falls to protective shelters. Therefore, understanding of impact behavior of RC members plays a vital role not only for design stages but also retrofitting and strengthening purposes thereafter. For this purpose, an experimental program was carried out to reveal the impact behavior of RC slabs strengthened with carbon textile reinforcements. In this program, four slabs specimens, two unstrengthened and two strengthened with two different carbon textile reinforcements, having dimensions of 1.5 m × 1.5 m × 0.2 m were tested by using an advanced impact testing facility at Otto-Mohr Laboratorium of Technische Universität Dresden. In these tests, all slabs were tested under repeated impact loads by using the same steel striker with a 200 mm - diameter flat contact surface in the velocity range of 25.2 to 30.2 m/s. The results obtained from these tests are presented in terms of midpoint-displacement histories, reaction force histories, slab accelerations, and strain histories of steel reinforcements for each impact. As a result of the test program, it is shown that carbon textile reinforcements have significant effects on enhancing impact capacity as well as limiting maximum and residual midpoint displacements. By using the data obtained from tests, a finite element (FE) modeling study was performed by using the LS-DYNA software tool. In this study, two FE models with different mesh sizes were created and compared with each other to obtain efficient modeling conditions. In the light of the tests and validated models, a parametric study was performed to figure out efficient impact conditions and parameters for carbon textile reinforcements. It is shown that carbon textile reinforcements are more effective for limiting damage levels under low-velocity impacts.

# ÖZET

## TEKSTİL DONATILI BETON DÖŞEMELERİN DARBE DAVRANIŞI

Betonarme teknolojisi, inşaat mühendisliği yapılarında hala en çok tercih edilen ve en yaygın olan teknolojidir. Bu yapılar, tasarım amaçları ve ihtiyaçları doğrultusunda yüklere karşı koymak için tasarlanırlar. Betonarme yapılar, ömürleri boyunca araç çarpması, tayfunlar, tsunamiler ve sellerden dolayı oluşan enkaz çarpması, koruyucu sığınaklara kaya veya cisimlerin çarpması gibi, beklenen ya da beklenmeyen sebeplerle darbelere maruz kalabilirler. Bu yüzden, betonarme elemanların darbe davranışlarını anlamak, sadece tasarım aşamalarında değil, aynı zamanda sonrasında yapılan güçlendirme ve iyileştirme çalışmaları için de önemli bir rol oynamaktadır. Bu amaçla, karbon tekstil donatı ile güçlendirilmiş betonarme döşemelerin darbe davranışını ortaya koymak için deneysel bir çalışma yapılmıştır. Bu çalışmada, ikisi güçlendirilmemiş ve ikisi karbon tekstil donatı ile güçlendirilmiş, 1.5 m × 1.5 m × 0.2 m boyutlarında dört adet betonarme döşeme gelişmiş deney düzeneği kullanılarak Dresden Teknik Üniversitesi Otto-Mohr Laboratuvarlarında test edilmiştir. Bu testlerde, tüm döşemeler, 200 mm çapında düz yüzeye sahip çelik çarpan ile 25.2 ile 30.2 m/s hızlarda tekrarlı darbelere maruz bırakılmıştır. Testlerden elde edilen sonuçlar, her darbe için, orta nokta yer değiştirme, mesnetteki kuvvetler, döşemedeki ivmeler ve çelik donatılardaki gerinim değişimleri olarak sunulmuştur. Deney programının sonucu olarak, karbon tekstil donatıların, darbe kapasitesini artırmasının yanı sıra, orta nokta yer değiştirmelerini sınırlamada çok etkin olduğu gösterilmiştir. Deneylerden elde edilen sonuçlar kullanılarak, sonlu eleman modelleme çalışması LS-DYNA yazılımı kullanılarak gerçekleştirilmiştir. Bu çalışmada, etkin model koşullarını elde edebilmek amacıyla, farklı ağ örgüsü boyutlarına sahip iki adet sonlu eleman modeli oluşturulup incelenmiştir. Gerçekleştirilen deneyler ve doğrulanan modeller ışığında, karbon tekstil donatıları için etkili darbe koşulları ve değişkenlerini ortaya çıkarabilmek için parametrik bir çalışma yapılmıştır. Bu çalışma, karbon tekstil donatıların düşük darbe hızlarında hasar seviyelerini sınırlamakta daha etkin olduğunu göstermiştir.

# TABLE OF CONTENTS

LIST OF FIGURES .....	ix
LIST OF TABLES.....	xiii
CHAPTER 1. INTRODUCTION .....	1
1.1. Motivation.....	2
1.2. Objectives .....	3
1.3. Thesis Outline .....	4
CHAPTER 2. LITERATURE REVIEW .....	5
2.1. Experimental Investigations .....	6
2.2. Numerical Investigations .....	10
2.3. Investigations on RC Members Strengthened with Fabrics.....	14
2.4. Research Significance of the Current Study .....	21
CHAPTER 3. EXPERIMENTAL PROGRAM.....	23
3.1. Test Specimens .....	23
3.1.1. Construction of Specimens.....	25
3.2. Test Facility .....	27
3.3. Materials .....	29
3.3.1. Concrete.....	29
3.3.2. Steel Reinforcement .....	31
3.3.3. Carbon Textile Reinforcements.....	31
3.4. Instrumentation .....	34
3.4.1. Load Cells.....	34
3.4.2. Laser Displacement Sensors.....	35
3.4.3. Accelerometers .....	35
3.4.4. Strain Gauges.....	37
3.4.5. High-Speed Camera.....	38
3.4.6. Data Acquisition System .....	38
3.5. Impact Tests .....	38
3.5.1. S1T0 Specimen.....	39

3.5.2. S2T0 Specimen.....	40
3.5.3. S3T1 Specimen.....	41
3.5.4. S4T2 Specimen.....	42
3.5.5. The Punching Cone Observations .....	44
CHAPTER 4. TEST RESULTS AND DISCUSSION .....	45
4.1. Impact Test Observations .....	45
4.1.1. S1T0 Specimen.....	45
4.1.2. S2T0 Specimen.....	47
4.1.3. S3T1 Specimen.....	47
4.1.4. S4T2 Specimen.....	49
4.2. Digital Signal and Data Analysis.....	50
4.3. Displacements .....	54
4.3.1. Midpoint Displacements.....	54
4.3.2. Edge Displacements .....	59
4.4. Reactions.....	60
4.5. Accelerations .....	64
4.6. Steel Reinforcement Strains.....	66
CHAPTER 5. FINITE ELEMENT MODELING .....	69
5.1. Modeling of Impact Tests .....	69
5.1.1. Material Models.....	71
5.1.2. Erosion Criteria .....	74
5.1.3. Mesh Sensitivity Investigations.....	76
5.1.3.1. S1T0 Specimen .....	78
5.1.3.2. S2T0 Specimen .....	80
5.1.3.3. S3T1 Specimen .....	83
5.1.3.4. S4T2 Specimen .....	86
5.1.3.5. Summary of Finite Element Modeling Investigations .....	90
CHAPTER 6. PARAMETRIC INVESTIGATION .....	96
6.1. Fictitious Specimens for Parametric Investigations.....	96

6.1.1. Specimens in Family #1 .....	98
6.1.2. Specimens in Family #2 .....	99
6.1.3. Theoretical Static Capacities of Specimens.....	101
6.2. Finite Element Modeling Results .....	105
6.2.1. The Midpoint Displacements of the Specimens in Family#1.....	106
6.2.2. The Midpoint Displacements of the Specimens in Family#2.....	109
6.2.2.1. The Midpoint Displacements of the Specimens in Group#1 ..	110
6.2.2.2. The Midpoint Displacements of the Specimens in Group#2 ..	112
6.2.2.3. The Midpoint Displacements of the Specimens in Group#3 ..	114
6.3. Summary of the Parametric Investigations .....	116
 CHAPTER 7. CONCLUSIONS AND RECOMMENDATIONS.....	 118
7.1. Conclusions.....	118
7.2. Recommendations for Future Studies.....	120
 REFERENCES .....	 122
 APPENDICES	
APPENDIX A.....	128
APPENDIX B .....	131
B.1. Yield Line Mechanisms .....	131
B.2. Ultimate Punching Capacity.....	135
B.2.1. TS500 (Turkish Standards Institution, 2000).....	136
B.2.2. EUROCODE 2 (European Committee for Standardization, 2004).....	136
B.2.3. ACI 318M-19 (American Concrete Institute, 2019).....	137
B.2.4. CSA A23.3-04 (Canadian Standards Association, 2004).....	139

# LIST OF FIGURES

<b><u>Figure</u></b>	<b><u>Page</u></b>
Figure 2.1. Damage types caused by impact phenomena (Source: Hering et al., 2020) ..	6
Figure 2.2. Reinforcement layouts (Source: Beckmann, 2012).....	15
Figure 2.3. Slab specimen with steel fabric (on left: B7) and carbon fabric (on right: B9) (Source: Beckmann, 2012).....	15
Figure 2.4. Strengthening layout of specimens (dimensions are given in mm) (Source: Yilmaz et al., 2018).....	17
Figure 2.5. Reinforcement details and dimensions (Source: Soltani et al, 2020).....	18
Figure 2.6. Specimen configurations (Source: Kishi et al., 2020).....	19
Figure 2.7. Test setup (Source: Schladitz et al., 2012) .....	20
Figure 2.8. Schematic representation of assemblages (Source: Al-Salloum et al., 2011) .....	21
Figure 3.1. Typical steel reinforcement layout for all specimens and the cross- sectional view of strengthened specimens (dimensions in mm).....	24
Figure 3.2. Naming conventions for test specimens.....	24
Figure 3.3. Specimen construction .....	25
Figure 3.4. Application of strengthening layer to bottom face of RC slab: a) washing of unset concrete; b) plastering fine-aggregated concrete; c) placing textile reinforcements; d) finished specimen .....	26
Figure 3.5. Testing facility (Batarlar et al., 2020) .....	27
Figure 3.6. Details of support conditions.....	28
Figure 3.7. The support conditions of testing facility: a) without test specimen; b) with test specimen.....	28
Figure 3.8. Standard tests for fine-grained concrete according to the ASTM: a) compressive strength test; b) three-point flexural strength test .....	30
Figure 3.9. The carbon textile reinforcements: a) Type 1, and b) Type 2 .....	31
Figure 3.10. Typical tensile test of textile-reinforced concrete sample.....	32
Figure 3.11. Stress-strain profiles of test samples with Type 1 for uniaxial tensile test	33
Figure 3.12. Stress-strain profiles of test samples with Type 2 for uniaxial tensile test	33
Figure 3.13. Load cell at the support .....	34

<b><u>Figure</u></b>	<b><u>Page</u></b>
Figure 3.14. The measurement points of the laser displacement sensors (all dimensions in mm) .....	35
Figure 3.15. The locations of accelerometers (all dimensions in mm).....	36
Figure 3.16. The application of accelerometer .....	36
Figure 3.17. Final view of a strain gauge .....	37
Figure 3.18. The locations of strain gauges attached on bottom reinforcing mesh (all dimensions in mm).....	37
Figure 3.19. High-speed camera views: a) side view; b) top view .....	38
Figure 3.20. The final state of the S1T0 specimen .....	40
Figure 3.21. The final state of the S2T0 specimen .....	41
Figure 3.22. The final state of the S3T1 specimen .....	42
Figure 3.23. The final state of the S4T2 specimen .....	44
Figure 3.24. Slab specimens after being cut into half.....	44
Figure 4.1. S1T0 specimen bottom face crack profiles after the first and final impacts	46
Figure 4.2. S2T0 specimen bottom face crack profiles after the first and final impacts	47
Figure 4.3. S3T1 specimen bottom face crack profiles after the first and final impacts	48
Figure 4.4. S4T2 specimen bottom face crack profiles after the first and final impacts	49
Figure 4.5. Measured midpoint displacements and developed power spectrum for the first impact test of S4T2.....	52
Figure 4.6. Measured strains and developed power spectrum for strain gauge 1 in the first impact test of S1T0 specimen.....	53
Figure 4.7. Measured reactions and developed spectrum for load cell 1 in the first impact test of S1T0 specimen .....	53
Figure 4.8. Measured accelerations and developed spectrum for accelerometer 1 in the first impact test of S1T0 specimen.....	54
Figure 4.9. Midpoint displacement-time histories of S1T0 and S2T0.....	56
Figure 4.10. Midpoint displacement-time histories of S3T1 and S4T2.....	57
Figure 4.11. Midpoint displacement-time histories of S4T2 .....	58
Figure 4.12. Midpoint displacement-time histories of S1T0, S3T1 and S4T2.....	59
Figure 4.13. Edge displacements for S1T0-1, S3T1-1 and S4T2-1 .....	60
Figure 4.14. The reactions measured from each load cell for S1T0-1 test.....	60
Figure 4.15. The measured total reactions for S1T0 and S2T0 specimens .....	61
Figure 4.16. The measured total reactions for S3T1 and S4T2 specimens .....	62

<b><u>Figure</u></b>	<b><u>Page</u></b>
Figure 4.17. The measured total reactions for S3T1 and S4T2 specimens .....	63
Figure 4.18. The measured accelerations from the midpoint of specimens (Acc4) .....	65
Figure 4.19. The measured accelerations for S4T2-3 .....	65
Figure 4.20. The measured reaction forces at each load cells for S4T2-3.....	66
Figure 4.21. The strain time histories of S1T0 and S2T0 specimens .....	68
Figure 4.22. The strain time histories of S3T1 specimen measured from SG3 .....	68
Figure 5.1. A quadrant of a slab specimen modeled in LS-DYNA .....	71
Figure 5.2. The compaction curves and the shape of Ottosen yield surface employed in Winfrith Concrete Model (source: Alonso (2013)) .....	72
Figure 5.3. Elastic-plastic behavior with kinematic and isotropic hardening (source: LS-DYNA User’s Manual, 2020).....	73
Figure 5.4. The model with Mesh#1 .....	77
Figure 5.5. The model with Mesh#2 .....	77
Figure 5.6. The created models with varied element sizes .....	77
Figure 5.7. The midpoint displacement-time histories of S1T0 for the analyses and tests .....	78
Figure 5.8. The total reaction force-time histories of S1T0 for the analyses and tests..	79
Figure 5.9. Punching cone formations in test and models for S1T0 specimen.....	80
Figure 5.10. The midpoint displacement-time histories of S2T0 for the analyses and tests .....	81
Figure 5.11. The total reaction force-time histories of S2T0 for the analyses and tests.	82
Figure 5.12. Punching cone formations in test and models for S2T0 specimen.....	83
Figure 5.13. The midpoint displacement-time histories of S3T1 for the analyses and tests .....	84
Figure 5.14. The total reaction force-time histories of S3T1 for the analyses and tests.	85
Figure 5.15. Punching cone formations in test and models for S3T1 specimen.....	86
Figure 5.16. The midpoint displacement-time histories of S4T2 for the analyses and tests .....	88
Figure 5.17. The total reaction force-time histories of S4T2 for the analyses and tests.	89
Figure 5.18. Punching cone formations in test and models for S4T2 specimen.....	90
Figure 5.19. The typical energy levels in the models .....	91
Figure 6.1. Naming conventions for fictitious specimens .....	98
Figure 6.2. The cross-section of the specimens in Family#1.....	98

<b><u>Figure</u></b>	<b><u>Page</u></b>
Figure 6.3. The cross-section of the specimens in Family#2.....	100
Figure 6.4. Strain, stress, and force distribution in section. (Redrawn from Chen and Li (2005), and modified for textile reinforcement).....	103
Figure 6.5. The midpoint displacement-time histories of specimens for the first impacts in Family#1 .....	107
Figure 6.6. The midpoint displacement-time histories of specimens for the third impacts in Family#1 .....	109
Figure 6.7. The midpoint displacement-time histories of specimens for the first impacts in Group#1 .....	112
Figure 6.8. The midpoint displacement-time histories of specimens for the first impacts in Group#2.....	114
Figure 6.9. The midpoint displacement-time histories of specimens for the first impacts in Group#3.....	116
Figure A.1. S2T0 specimen bottom face crack profiles for each impact event.....	128
Figure A.2. S3T1 specimen bottom face crack profiles for each impact event.....	129
Figure A.3. S4T2 specimen bottom face crack profiles for each impact event.....	130
Figure B.1. Yield line mechanism - Pattern#1.....	132
Figure B.2. Yield line mechanism - Pattern#2.....	133
Figure B.3. Yield line mechanism - Pattern#3.....	134
Figure B.4. Unit strip illustration for a strengthened RC slab .....	135
Figure B.5. Control perimeters according to the design codes.....	136

# LIST OF TABLES

<b><u>Table</u></b>	<b><u>Page</u></b>
Table 3.1. Specimen details .....	24
Table 3.2. Cylinder tests results .....	29
Table 3.3. Standard test results for fine-grained concrete .....	30
Table 3.4. Material properties of the textile reinforcements.....	34
Table 3.5. Test protocol .....	39
Table 4.1. Measured displacements at the midpoint.....	59
Table 4.2. Measured peak support reactions.....	63
Table 5.1. The midpoint displacements from the FE analyses and tests .....	92
Table 5.2. The penetration depths of the striker from the FE analyses and tests .....	93
Table 5.3. The total peak reactions from the FE analyses and tests .....	94
Table 5.4. The computational demands and sizes of the FE models .....	94
Table 6.1. Specimens in the Family#1 .....	99
Table 6.2. Specimens in the Family#2.....	101
Table 6.3. The calculated capacities of the specimens in the Family#1 .....	104
Table 6.4. The calculated capacities of the specimens in the Family#2 .....	105
Table B.1. Yield patterns of the specimen in the Family#1 .....	135
Table B.2. Yield patterns of the specimen in the Family#2 .....	135
Table B.3. The calculated parameters for the specimen in the Family#1 .....	140
Table B.4. The calculated parameters for the specimen in the Family#2.....	140

# CHAPTER 1

## INTRODUCTION

Civil engineering designs and applications have been developing progressively in the direction of demands from the societies and cultures in the world. In accordance with developments in engineering concepts such as material knowledge, manufacturing methods, and computational capabilities, civil engineering structures with higher complexities have been built for the last few decades. When these engineered structures are considered, reinforced concrete (RC) designs and applications do not only constitute the majority of existing older structures, but they are also still the most preferable technology in civil engineering.

During the design stages of RC structures and members, high rate loading scenarios may need to be taken into account in parallel with design purposes and needs. Therefore, this type of loading scenarios such as impact or blast loads on RC structures and members draw heavy attention from many researchers and designers. For particular demands and purposes, such as military defense needs and protection against terrorist activities, designing stages of RC structures require special procedures and methods. Beside these unusual actions, civil engineering structures may be subjected to extreme dynamic loading conditions more frequently such as vehicular or glacier collisions to bridge piers, debris or object impacts caused by typhoons, floods or tsunami, or rock falls to protective RC shelters in mountainous areas. With the aim of preventing catastrophic consequences of the possible impact events, understanding of the behavior of RC members under impact load is very crucial for not only the designing stages but also retrofitting possibilities thereafter.

Despite numerous studies carried out on the impact behavior of RC members by many researchers and methods and approaches developed for predicting the impact behavior of RC structures, design for impact is still a challenging task. On the other hand, to design an impact-resistant structure, highly generalized empirical formulae and approaches can be used for estimating impact capacities and damage levels. On the other hand, with the developments in high-performance computing technology, non-linear finite element analysis (NLFEA) programs have been developed, and modeling of impact behavior of RC members by using these sophisticated programs is becoming

more attractive for designers and engineers. However, NLFEA simulations of RC structures under impact load often require a high number of input parameters that may not exist or must be assumed.

When the complexity of impact phenomena on RC members is considered, making use of new methods in designing structures under high-rate loading conditions is warranted. Additionally, with the developments in material science and technologies, new reinforcing materials and methods can be used in the course of designing RC members and structures.

The research presented herein is an investigation of the impact behavior of RC slabs strengthened with an additional layer of mesh-form carbon-textile reinforcement embedded in a fine-grained concrete matrix which is a relatively new reinforcing method. This type of fabric reinforcements has been investigated by many researchers under static loading conditions whereas their performances under impacts are not revealed yet.

## **1.1. Motivation**

With the intent of improving the capacity of RC members and structures, different types of materials and techniques are employed by researchers and engineers to obtain more efficient and better methods. As mentioned previously, mesh-form textile-reinforced concrete (TRC) composite is one of the modern techniques that is commonly used for engineering purposes such as strengthening and retrofitting, as well as architectural purposes such as shading, exterior façade elements, and free-form or curved elements. Starting from the beginning of this century, the popularity of TRC elements has been increasing and numerous studies on TRC composites have been carried out by researchers in the last two decades. For instance, experimental studies on TRC composites were presented with the aim of revealing the efficiency as a strengthening method on cyclic behavior of masonry infilled-RC frames (Koutas et al., 2019; Triantafillou, 2010), flexural behavior of slabs (Beckmann et al., 2015; Schladitz et al., 2012) and shear behavior of beams and slabs (Bruckner et al., 2006; Tzoura & Triantafillou, 2016).

In the light of literature on TRC composites, the use of mesh-form of textile reinforcements can be very beneficial to enhance impact capacity of members and

structures. The studies on the alternative strengthening method of fiber-reinforced polymer (FRP) applications and methods for impact behavior of RC members can be found in the literature, whereas the numerical or experimental works on mesh-form TRC members subjected to high-rate loading conditions are almost nonexistent in the literature.

The research presented in this thesis is intended to contribute to the literature by providing a well-documented experimental data on impact behavior of RC slabs strengthened with mesh-form carbon textile reinforcements. Additionally, by using the data from the testing procedure, a three-dimensional finite element (FE) model was validated and used for parametrical study on slab specimens to reveal the efficient conditions and parameters for carbon textile reinforcements under impact loadings. It is believed that the experimental data and created FE model will be beneficial for researchers and engineers in further studies which deal with the impact phenomena on RC structures and members

## **1.2. Objectives**

In this study, three main targets are planned to be reached in the given order:

- I. To carry out an experimental research on the impact behavior of RC slab specimens, for both unstrengthened specimens and specimens strengthened with carbon textile reinforcements, with particular focus on:
  - i. Examining the effect of the striker velocity on the impact behavior of unstrengthened RC slab specimens,
  - ii. Evaluating the influence of carbon textile reinforcements with varied ratios and geometries on impact capacity, crack patterns, and failure modes,
  - iii. Presenting a well-instrumented impact test program accompanied with a well-documented data on the behavior of RC slabs with and without carbon textile reinforcements,
- II. To establish a methodology for three dimensional FE modeling of RC slabs strengthened with carbon textile reinforcements by using LS-DYNA (Livermore STC, 2019) software, focusing on:

- i. Validating the developed FE methodology by investigating different material models, contact types, and element sections,
  - ii. Investigating the numerical erosion parameters in comparison with the literature,
  - iii. Investigating the mesh sensitivity problems and computational costs
- III. To present a parametrical study on impact behavior of slab specimens investigating contributions of carbon textile reinforcement under different impact loading conditions such as striker velocity, mass, and diameter

### **1.3. Thesis Outline**

The performed investigations are structured and presented in seven chapters.

In Chapter 2, relevant experimental and numerical investigations available in literature on the impact response of RC members are summarized and explained.

Chapter 3 presents the experimental program of the study, testing facility, instrumentations, and the testing protocol in detail.

In Chapter 4, impact test results are discussed both qualitatively and quantitatively. Measured data and observations made from the impact tests are documented in this chapter.

Chapter 5 describes the development of FE models. Created models are compared and validated with data obtained from tests.

In Chapter 6, performed parametrical study by using the verified FE simulations are presented. In this chapter, contributions of carbon textile reinforcements under impact loads are examined case by case.

Chapter 7 presents the conclusions and outcomes of this study, including suggestions and recommendations for further works.

## CHAPTER 2

### LITERATURE REVIEW

The behavior of RC structures under extreme loading conditions has been investigated by many researchers in the literature. Understanding of impact behavior of RC members plays a crucial role to avoid catastrophic consequences in particular cases such as impacts caused by hard or soft objects. In soft impact events, impacting object can deform significantly during impact, whereas deformation of impacting object is negligible or minor in hard impact events. Additionally, in the course of these impact events, targets may respond in different manners, causing different modes of suffering from impact loads. Depending on impact parameters and loading scenarios, impact phenomena are classified according to the failure modes as (i) local and (ii) global response, in general. In local response mechanisms, imparted impact energy is dissipated at the vicinity of impact zone, which may lead to a localized damage such as (a) scabbing of concrete at impacted surface, (b) concrete spalling at back face of target, (c) perforation of striker or (d) punching cone plugging. In the case of global response, the target deforms globally under impact load that may cause flexural, shear, or shear-flexural combined failure. The classified failure modes of RC targets are depicted in Figure 2.1.

The research presented in this thesis focuses on the impact possibilities that may be encountered mostly in civil engineering structures. For this reason, in this literature survey, the studies and investigations performed for military cases or purposes are not presented. To provide filtered information relevant to the presented study, investigations on the impact response of RC members are briefly described. Therefore, these investigations are categorized as three main groups: 1) experimental; 2) numerical investigations on RC members; and, 3) investigations on RC members strengthened with fabrics.

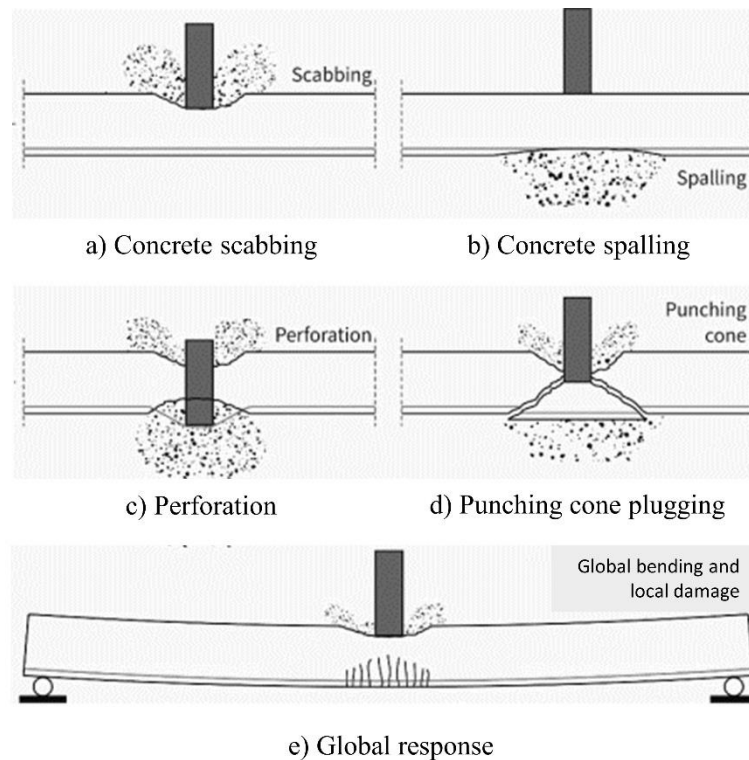


Figure 2.1. Damage types caused by impact phenomena (Source: Hering et al., 2020)

## 2.1. Experimental Investigations

As mentioned earlier, numerous studies were performed with the aim of understanding both local and overall response of RC members under impact loads. In accordance with the subject of this study, experimental studies from literature are presented herein, excluding studies for military purposes and perforation limit investigations, and also limiting the studies to the hard-impact phenomenon on RC members.

Dinic and Perry (1990) carried out a study on 20 circular flat RC slabs with 1.5 m diameter and varying thicknesses in the range of 60 to 80 mm. Impact loading was applied to the specimens by means of free fall of impactors with varied mass from predefined height. To define damage modes and failure types, mechanical and material parameters used for slabs were kept constant, whereas the mass and the velocity of strikers were varying, in the range of 31.30-75.25 kilograms and 3.0-10.0 m/s, respectively. It was reported that shear plug formation during impact was governed by the imparted impact energy.

Dancygier and Yankelevsky (1996) performed high-velocity impact test series on high strength and normal strength concrete plates with different reinforcing types

such as woven steel mesh and steel fibers to avoid severe scabbing at the rear face of the specimens. The family of plate specimens consisted of 21 plates with dimensions of 40 cm x 40 cm and varying thicknesses. These specimens were hit by a conical nose steel projectile with different velocities in the range of 85 to 230 m/s. Responses of the tested plates under high-velocity impacts were evaluated in terms of the dimensions of craters on both faces and penetration depth of the steel projectile. Authors concluded that the high-strength concrete enhanced impact resistance. Also, the use of steel fibers and woven steel mesh increases the impact resistance in particular to limit localized effects. They were able to minimize the damage at both faces of the elements.

To propose a new method for the rock-shed protection, Mougin et al. (2005) conducted an experimental investigation on an RC slab with a 1/3 scale of an actual structure. The slab specimen with the dimensions of 12.00 m × 4.80 m × 0.28 m was tested by using a 450 kg block which was mimicking a rockfall from 30 m height, resulting in 24.5 m/s contact velocity. In this study, specially designed supports were used for absorbing energy during impact. Authors reported that the slab specimen suffered from localized damage around the impact region. Also, it is concluded that the slab specimen could continue to serve after local restoration of concrete in impact area owing to energy absorbing capacities of the support conditions.

Another experimental test series on high mass-low velocity behavior on RC members, including beams and slabs, were conducted by Y. Chen and May (2009). Four 0.80 m x 0.80 m x 0.76 m slab specimens and two 2.30 m × 2.30 m × 0.15 m slab specimens were tested by means of a free-falling drop weight. In this extensive experimental study, slab specimens were subjected to drop-weight impact with varied contact velocity in the range of 6.5-8.7 m/s and varied masses between 98.7 to 382 kilograms. Additionally, the effects of concrete strength and steel reinforcement ratio on impact behavior of the slab specimens were investigated. The authors presented a comparative study by means of the test results and predictions from the empirical formulae obtained from the literature.

A series of impact tests on RC slabs was conducted at the Izmir Institute of Technology Structural Mechanics Laboratory between the years of 2013-2015. In these well-instrumented impact test series, 2150 mm × 2150 mm × 150 mm slab specimens were tested under free falling-weight impacts by using the same impact test setup. This innovative test setup provided simply supported conditions at 20 locations along the perimeter of slab specimens, accompanying the load cells at each location to measure

reactions. To obtain displacement profiles during the impacts, slab specimens were densely instrumented with displacement transducers. Additionally, accelerometers were employed to measure accelerations both on slabs and falling weights to obtain inertial and impact forces developed in the course of impacts. As a start of the test series, Batarlar (2013) conducted a study on RC slab specimens with varied conventional steel reinforcement ratios. In this study, slabs were subjected to impact loads by using free fall of 210 kilograms and 320 kilograms of mass from 2.5 meters, resulting in 7.0 m/s contact velocity. It is revealed that impact forces were resisted by inertial forces at the initial phases during impacts, and forces at the supports were developed at the post-impact stages. It is also reported that all specimens were failed under punching shear mechanisms, even though they were designed as a flexural-critical member. In pursuit of these tests, Arsan (2014) carried out impact tests on steel fiber RC slabs, and RC slabs with additional shear stud reinforcements around the impact vicinity by using the same test setup. In these tests, slab specimens were subjected to impact loads by means of 320 and 555 kilograms of free-falling masses with 7.0 m/s contact velocity. It is reported that steel fiber RC slabs showed higher impact capacities compared to the specimens with shear studs. Additionally, steel fibers were more effective than the shear studs to limit scabbing of concrete during impacts. In the light of these tests on steel fiber RC slabs, Yasayanlar (2015) investigated the effects of steel fiber ratios on impact resistance of RC slabs by using the same testing facility. In these tests, RC slab specimens having varied steel fiber volume content in the range of 0.5 % to 1.5 % were tested under free-falling masses of 320 and 555 kilograms. It is reported that the steel fibers were able to limit the crack profile and width developed during the impacts. It is also concluded that presence of steel fibers were able to prevent punching cone failure and prominent global failure mechanisms were observed during tests.

To show the performance of steel fiber RC slabs for the impact-resistant designs, Hrynyk and Vecchio (2014) carried out an experimental study on seven RC slabs with varied steel fiber contents subjected to repeated drop-weight impacts.  $1.80\text{ m} \times 1.80\text{ m} \times 0.13\text{ m}$  RC slabs with and without additional fiber reinforcements were subjected to sequential impacts by means of free fall of varied masses ranging from 150 to 300 kg, resulting in the 8 m/s velocity. In their well-instrumented testing program, accelerometers, strain gauges, load cells and potentiometers were used to determine the impact characteristics such as impact loads from drop weights, reaction forces, and crack and displacement profiles of the specimens. Authors concluded that steel fibers

were successful to reduce the crack spacing, penetration of striker and mitigate the local damage level such as scabbing. Additionally, despite the employed slabs were designed to fail in flexure, failure of the slabs was controlled by the punching shear mechanisms.

To enhance the impact capacity of RC members, researchers were also seeking to employ a combination of high-performance materials and extra reinforcing methods. For instance, Othman and Marzouk (2016) tested six reinforced plates with the dimensions of 1.95 m × 1.95 m × 0.10 m by dropping a 475 kg of mass with varying contact velocity (8.55-9.00 m/s) multiple times until failure. In this study, the effects of concrete strength, steel fiber, and conventional steel reinforcement ratios were investigated. Similar to the previous study, sophisticated instrumentations such as accelerometers for drop weights and specimens, load cells for the reaction forces, and contactless laser sensors to measure displacements at two points were used to provide qualitative outcomes after each impact. In addition to these qualitative results, quantitative observations were also presented such as crack patterns of the specimens that suffered from impact loads. Authors concluded that the specimens produced with ultra-high-performance fiber reinforced concrete (UHP-FRC) showed superior performance compared to the high-strength concrete plates in terms of damage level. Moreover, the failure modes of the specimens were changed from shear to pure flexural form by means of UHP-FRC under sequential low-velocity impact loadings. Besides, it is reported that the amount of conventional steel reinforcement ratio has an important role on the overall impact behavior of the specimens, limiting the peak and residual midpoint displacements.

Xiao et al. (2016) presented a study consisted of two testing phases on 1200 mm × 1200 mm × 150 mm slab specimens with different steel reinforcement ratios. In the first testing part of this study, slab specimens were tested at different loading rates, starting from 0.0004 m/s to 2 m/s. Then, in the second part of the study, six slab specimens were subjected to impact loads by means of free fall of a 500 kg drop hammer with a flat contact surface in 200 mm diameter, resulting in 5.425 m/s contact velocity. Displacements, load measurements, and accelerations captured in both testing phases were presented. Researchers aimed to present a comparative study to make a comparison between specimens tested under low-velocity impact loads and different loading rates in terms of energy absorption capacities and crack patterns. It is reported that high-loading rate tests can be considered as an alternative approach for low-

velocity impact tests when the load and energy capacities of the tested slabs were compared.

Hering et al. (2020) carried out an experimental test series of fifteen 1500 mm  $\times$  1500 mm square RC plates with varied thicknesses under impact loads by means of 21.67 kg of a steel striker with a 100 mm flat surface. With the help of an advanced testing facility, the striker can be accelerated and the slabs were tested under varied contact velocities, ranging from 9.2 m/s to 73.9 m/s. All tested plates had the same steel longitudinal reinforcements with 100 mm spacing whereas the thickness of the plates varied as 100 mm, 200 mm, and 300 mm. In these tests, displacements were captured by using two contactless sensors, and accelerations were measured at four points on the plates. After tests, employed specimens were cut into two pieces to expose the punching cone geometry. Researchers concluded that both bending and punching cone failure were observed in the tests, yet the punching cone failure was the dominant failure pattern.

## **2.2. Numerical Investigations**

Different approaches for investigating the response of RC members under different impact loading conditions draw interest from many researchers. When limitations on testing structures under fast loading conditions such as cost, specimen scaling, instrumentation are considered, numerical, analytical, or empirical methods can be attractive solutions for researchers and engineers. With developments in computer technology, modeling and simulating structures subjected to fast loading conditions are becoming more efficient and more cost-friendly day by day compared to testing. The most common numerical technique, Finite Element Method (FEM), is employed by many researchers to analyze structures under various types of dynamic loading conditions such as blast, impact, and wind. Therefore, the FEM investigations performed by researchers are presented herein. In accordance with the thesis topic, the finite element studies from the literature were limited to hard impact studies on RC members.

Tai (2009) presented a study on 240 mm  $\times$  240 mm  $\times$  50 mm ultra-high-strength and normal concrete plate specimens reinforced with steel fibers subjected to 0.3 kg steel projectile with varied velocities in the range of 27 m/s -104.1 m/s. Afterward, the

employed plate specimens were modeled by using LS-DYNA software. In these models, due to axisymmetric testing conditions, only one-quarter of the test arrangement was created. To model ultra-high-strength and normal concrete plates, an elastic-viscoplastic model of Johnson-Holmquist Concrete (JHC) Model was employed. Models were compared with the outputs from the testing phase of the study in terms of damage patterns and the type of projectile during impacts. It is reported that the models employed in the finite element code showed reasonably good agreement with data obtained from experiments.

Sangi (2011) presented an extensive study on modeling and analyzing RC beams and slabs tested under low-velocity impact loads by using LS-DYNA finite element software. In these simulations, Winfrith Model (Broadhouse & Attwood, 1993) and Concrete Damage Model (Malvar et al., 1997) for concrete, Plastic Kinematic Model for steel reinforcements, and Rigid Model for striker and boundaries were used. Fourteen beams previously tested by Y. Chen and May (2009) were modeled and analyzed under free falling of a 98 kg mass with the 7.3 m/s contact velocity. All tested beams had the same cross-sections as 100 x 200 mm, whereas the lengths of the specimens were varying as 3 m and 1.8 m. Additionally, in the testing program, support conditions (pin-ended or simply-supported), contact surface geometry of striker (hemispherical or flat), impact interface (direct or indirect contact between striker and beams) were investigated. The simulated beams were compared quantitatively and qualitatively with the test results. The impact force-time histories, transient acceleration-time histories, and strain-time histories as well as the damage patterns of the beams were presented. It is reported that the created models and the material models used for the simulations showed good agreement with the test outcomes. In addition to finite element analyses of these beams, four previously-tested (Chen & May, 2009) 760 mm × 760 mm × 76 mm slab specimens and two 2320 mm × 2320 mm × 150 mm slab specimens were modeled and analyzed. The slab specimens were subjected to free fall of drop weights with varied masses (98.7 – 380.0 kg) and varied contact velocities (6.5 - 8.3 m/s). Similar to beam tests, the striker contact surface types were varied from flat to hemispherical. The response of the simulated slabs showed good agreement with the test results in general. It is reported that the material models and modeling parameters provided consistent and sufficient results with the test data of the specimens subjected to low-velocity drop weight impacts.

Alkloub (2015) carried out an experimental and numerical study on impact behavior of RC panels subjected to non-deformable projectile. In this study, 53 small-scale RC plates (250 mm × 250 mm × 25 mm) with changing longitudinal reinforcement ratio and spacing were tested under impacts. Impact loads were applied to the specimens by means of two 0.23 kg and 0.07 kg steel ball bearings with the contact velocity in the range of 18.3 m/s to 137.2 m/s. Data obtained from tests were presented as damage patterns of specimens, penetration depth or exit velocity of the strikers, and the crater volume of scabbed concrete at the back face of specimens. In the second part of this study, the finite element simulations were created by using the same material models with Sangi (2011) existing in LS-DYNA and the results were compared with the test results. It is concluded that longitudinal reinforcing ratios and spacing between bars must be considered in the design process of RC panels with the aim of preventing the scabbing of concrete or the perforation of striker. Also, the simulations analyzed by LS-DYNA were capable of catching similar results with the tests. The finite element models were able to predict punching shear crater as well as penetration or perforation of striker and scabbing of concrete.

Othman and Marzouk (2017) performed finite-element analyses of RC plates that were previously tested under repeated free fall of drop-weight impacts by the authors. The testing phase of this study was explained in the previous section of this literature review. Tested plate specimens were modeled by using ABAQUS finite element software. In the models, nonlinear behavior of concrete was provided by the built-in concrete model of CDP. Similarly, a built-in metal plasticity model provided by the software was employed for the steel reinforcements. Lastly, elastic material properties of steel were selected for modeling the supports at the boundaries and drop weights. The results from the analyses and tests were compared in terms of histories of impact forces, reaction forces, strains, and displacements. Additionally, the influence of damping ratios was examined in the finite element models and compared with the midpoint displacement responses obtained from the tests. Final damage patterns observed from tests and predicted by the FEM software were also presented. Authors concluded that the proposed model was able to satisfy good accuracy for predicting low-velocity impact behavior of RC plates. However, the selected concrete model was mesh dependent which was expected to be independent. It is also reported that the proposed numerical study could be employed for further studies in the future.

Xiao et al. (2017) carried out a study on fifteen 1200 mm square RC slabs with 150 mm thickness tested under low-velocity impacts. These specimens were subjected to the strikers with different contact surface geometries (flat or hemispherical) and varied masses (200-500 kg) and falling heights with identical impact momentum or energy. In addition to the experimental part of this study, a parametrical investigation was carried out by using LS-DYNA software. In the created models, the Continuous Surface Cap Model (CSCM) for concrete sections, the Piecewise Linear Isotropic Plasticity Model for steel reinforcements, and rigid material model were used for supports and striker. In this parametric investigation, different slab thicknesses, concrete strengths, steel reinforcement ratios, striker contact surface diameters, and impact energies were investigated. Afterward, by using results from finite element analyses, dimensionless empirical equations based on impact energy were proposed with the aim of providing an initial design or check for the impact response of the lightly-reinforced slabs subjected to low-velocity impacts.

Thai et al. (2018) performed a parametrical numerical study by using LS-DYNA on RC panels with varied longitudinal and shear reinforcement ratios to present their influences on penetration depth of striker and perforation thickness of panels. Afterward, modified empirical formulae were proposed by authors. To carry out finite element analyses, ten RC plate specimens performed by other researchers in the literature were selected. These selected RC specimens were tested under impact loads by means of 47.5 kg hard missile with different velocities in the range of 99.7 m/s to 144 m/s. To model specimens, Winfrith Concrete Model, Plastic Kinematic Model, and rigid material model were used for concrete, steel reinforcements, and striker, respectively. Employed models were compared with tested panels as damage patterns at both faces, crack profiles, penetration depth, and residual velocity of striker. It is reported that numerical results, generally, were in good agreement with test results. The prediction of the local damage by the models was accurate. In the light of the employed models, a parametric study was carried out to present the effects of longitudinal and shear reinforcement ratio in the plates subjected to hard impacts with varied velocities, from 50 m/s to 250 m/s. By using these analyses, modified empirical formulae were proposed to predict the penetration and perforation performances of the RC plates. Authors concluded that the modeling parameters provided good results when compared with tests. Also, influences of shear reinforcement on perforation thickness and penetration depth were presented.

### **2.3. Investigations on RC Members Strengthened with Fabrics**

As mentioned in the previous chapter, only a few studies on impact response of RC members with textile reinforcement strengthening can be found in the literature. However, fabric reinforced polymers (FRP) have been widely studied by researchers to enhance the capacity of RC sections. Therefore, studies in an effort to enhance impact capacity of RC members by using FRP applications filtered from literature are presented in this section.

Beckmann et al. (2012) performed drop tower experiments on RC slabs to present the strain behavior of slabs under impact loads. In this study, fifteen RC slabs with dimensions of 1.0 m × 1.0 m × 0.15 m were subjected to drop weights with varied velocities in the range of 7.7 to 13.3 m/s and masses of 183 and 290 kilograms. To reveal the contributions of different reinforcements, steel stirrups as shear reinforcement, and steel and carbon fabrics as additional strengthening layers were used (see Figure 2.2). Moreover, three different types of concrete, standard concrete, high-performance concrete, and ultra-high-performance concrete were used to reveal the concrete strength influence on impact behavior. According to the qualitative outcomes of this study, researchers reported that with the increase in concrete strength, damage levels of slabs were decreasing as expected. Surprisingly, steel stirrups used as shear reinforcement showed minor influence on the impact resistance and did not prevent the total perforation of the striker. Contrary to steel stirrups, steel and carbon fabric reinforcements used for strengthening layer performed better for the protection performance and prevented the total perforation under hard impact cases which can be seen in Figure 2.3.

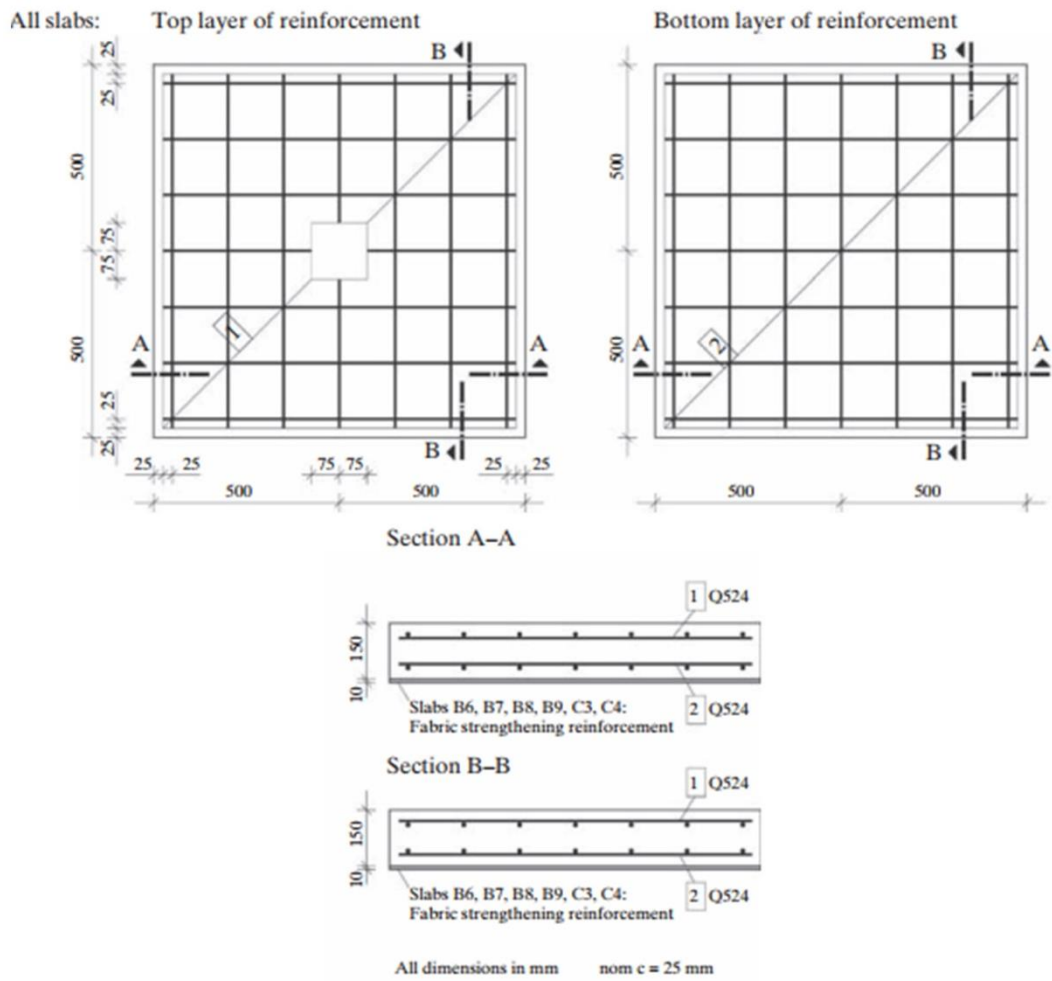


Figure 2.2. Reinforcement layouts (Source: Beckmann, 2012)

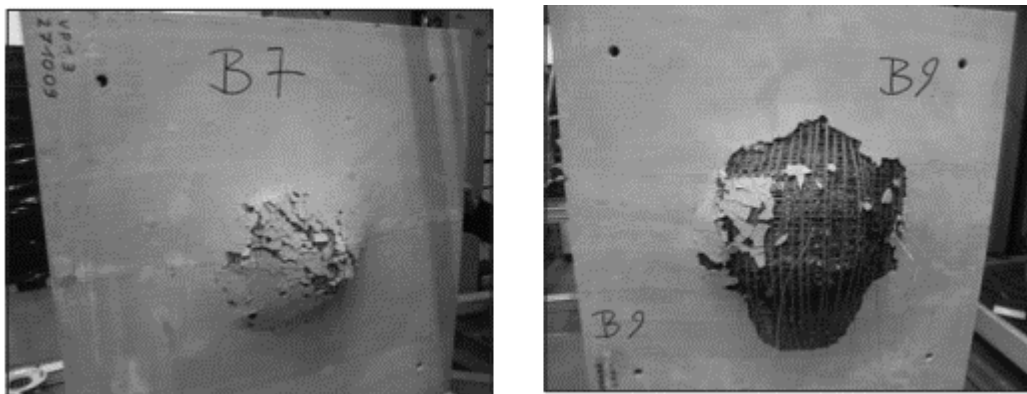


Figure 2.3. Slab specimen with steel fabric (on left: B7) and carbon fabric (on right: B9)  
(Source: Beckmann, 2012)

Yilmaz et al. (2018) carried out experimental and numerical investigations on impact behavior of eight RC slab specimens strengthened with carbon fiber reinforced polymers (CFRP) strips. In this study, all 1000 mm × 1000 mm × 80 mm slab specimens had an identical single layer of  $\phi 6$  steel reinforcing bars at the bottom with 150 mm spacing whereas the orientation and amount of CFRP strips were varying (see Figure 2.4). All specimens were tested under the same impact energy by means of free fall of 84 kg drop hammer from 1.5 m. Additionally, FEM analyses of tested specimens were performed by using ABAQUS FEM software. The results from tests and analyses were compared in terms of accelerations, maximum and minimum deformations. It is reported that strengthening slab specimens with CFRP strips was effective to improve low-velocity impact behavior, resulting in lower residual displacement and strains.

Soltani et al. (2020) presented a comparative study on impact behavior of RC slabs externally reinforced with glass fiber reinforced polymer (GFRP) sheets and internally reinforced with steel fibers. In this research, 1000 mm × 1000 mm × 75 mm slab specimens with different steel fiber ratios and externally bonded GFRP strips (see Figure 2.5) were tested under 105 kg drop weight impact by means of free fall from 2.5 m height, resulting in 7.0 m/s theoretical contact velocity. As a result of this comparative study, specimens strengthened with GFRP strips performed better than steel fiber reinforced concrete slabs, in general. Additionally, the specimens with more distributed GFRP strip on specimens showed lower maximum and residual displacement compared to other reinforcing combinations.

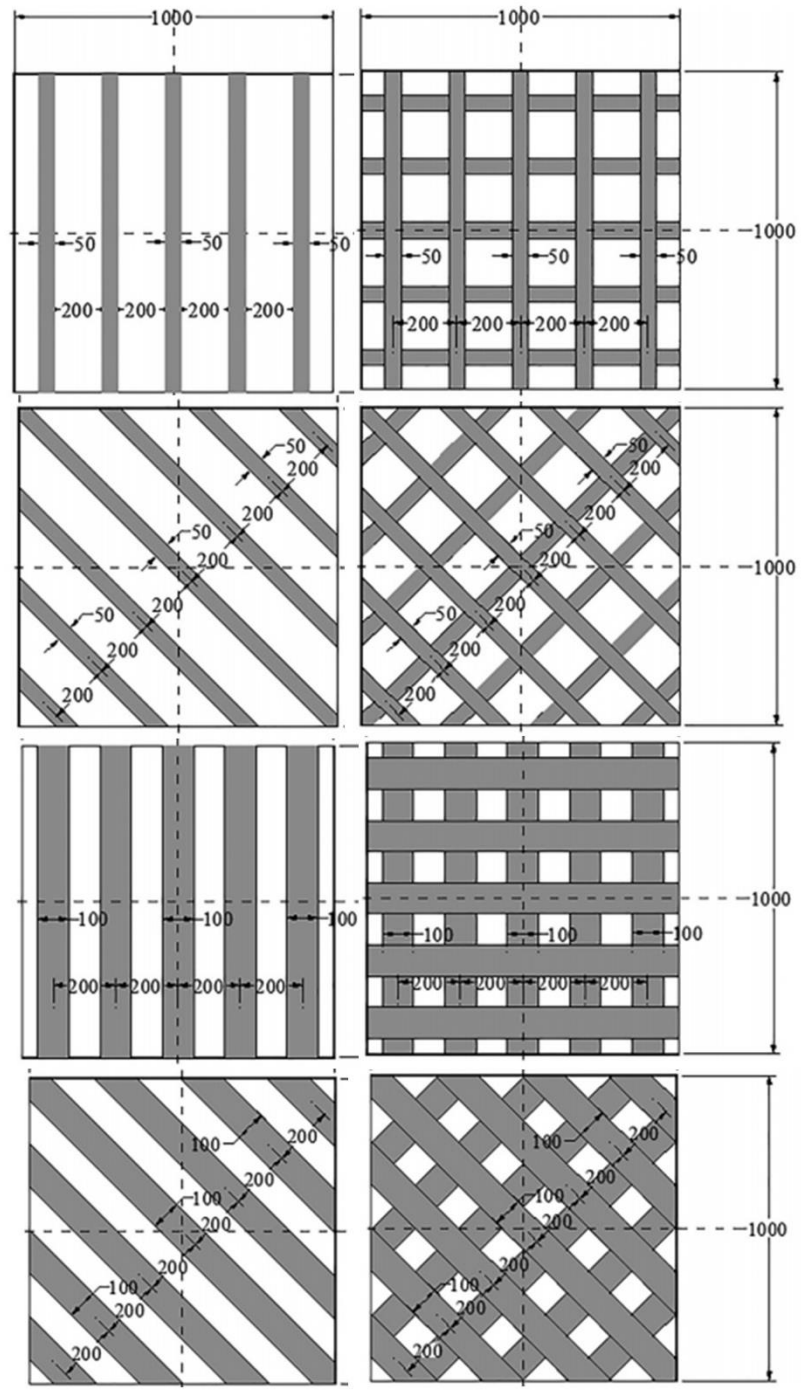


Figure 2.4. Strengthening layout of specimens (dimensions are given in mm)  
 (Source: Yilmaz et al., 2018)

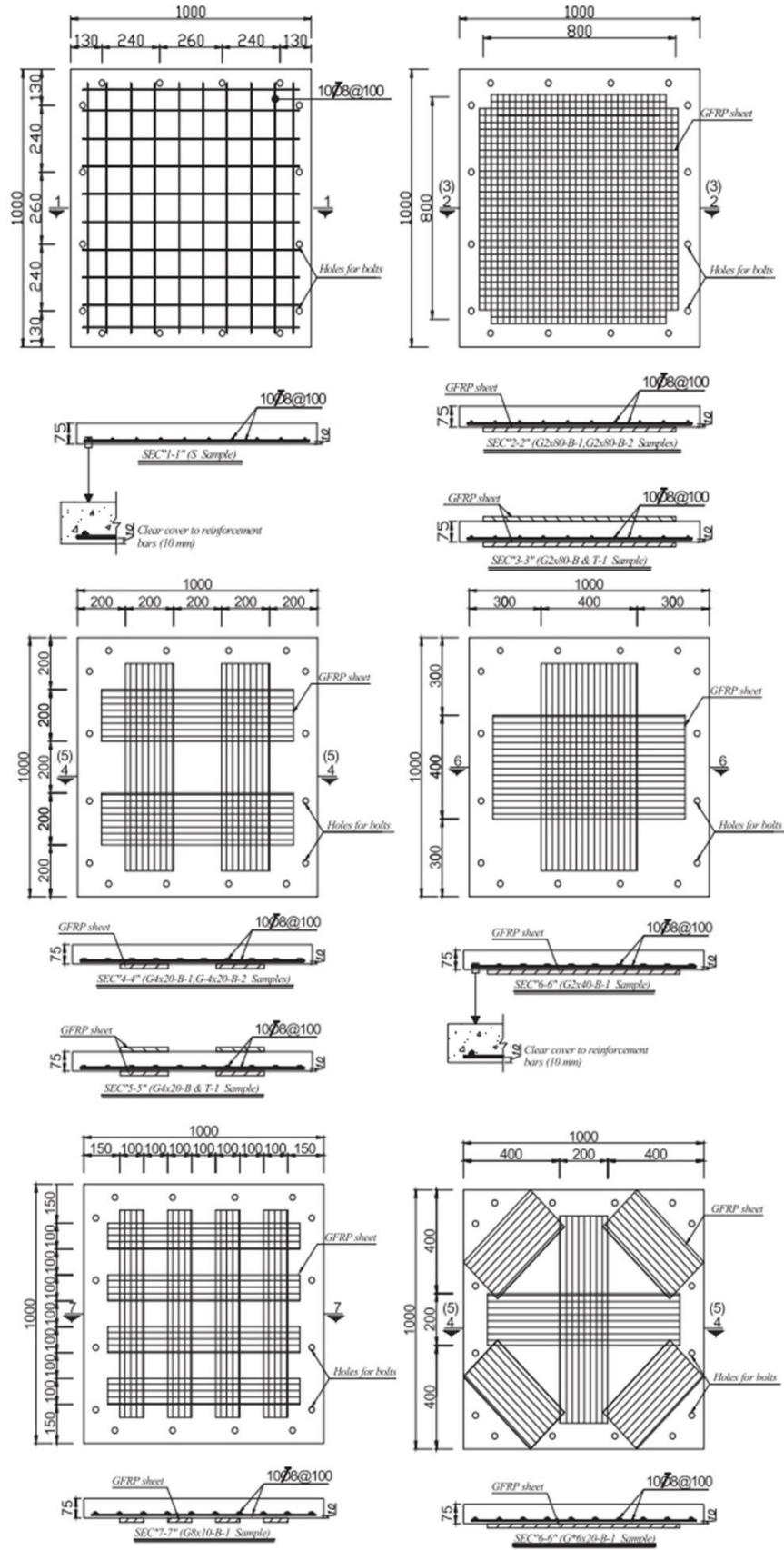


Figure 2.5. Reinforcement details and dimensions (Source: Soltani et al, 2020)

Kishi et al. (2020) carried out an experimental study on RC beams strengthened in flexure with aramid fiber reinforced polymers (ARFP) and CFRP sheets. In this study, nine beams with 200 mm × 250 mm cross-section and 3 m clear span length were tested under 300 kg of drop weight, falling from different heights with the range of 1.1 m to 3.2 m until the FRP sheets were debonded. The employed FRP sheets were applied only to the tension side of the beam surfaces (Figure 2.6). Researchers reported that both types of FRP sheets were successful to reduce the maximum and residual displacements of the specimens tested under low-velocity impact loads. Also, it is reported that energy-caused debonding in both FRP sheets was similar. The dissipated energy decreased by flexural strengthening on the beams was dependent upon FRP material characteristics.

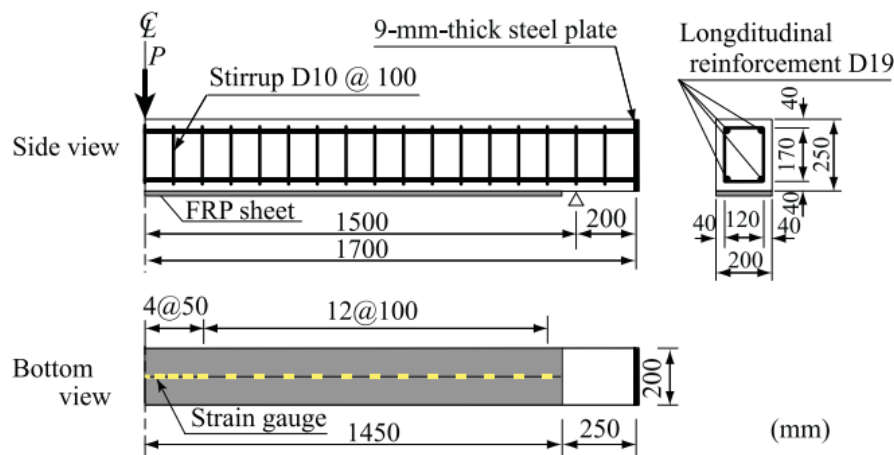


Figure 2.6. Specimen configurations (Source: Kishi et al., 2020)

As summarized here, different types of fabric reinforcements were investigated by researchers to reveal the contributions of these fabric reinforcements to impact behavior of RC members. With the intent to enhance impact capacity of RC members, alternative reinforcing methods and applications draw attention from researchers, and more studies can be found in the literature on strengthening or reinforcing methods with fabrics. However, as mentioned earlier, a few studies exist in the literature on the impact behavior of RC members strengthened with mesh-form carbon textile reinforcements. On the other hand, studies on textile reinforcement concrete composites (TRC) have been investigated by researchers for different types of loadings and purposes. In the literature, it can be found several studies that present the benefits of carbon textile reinforcements on the behavior of RC members under different loading types. For

example, Schladitz et al. (2012) performed an experimental study on RC slabs strengthened with additional carbon TRC composite. In this study, five slab specimens with dimensions of 7.00 m  $\times$  1.00 m  $\times$  0.23 m were manufactured and tested under four-point bending test (Figure 2.7). As a reference specimen, one of the slab specimen was kept unstrengthened, whereas others were strengthened with an increasing number of carbon TRC layers. It is reported that bending load capacity increased significantly in parallel with an increasing number of TRC layers.

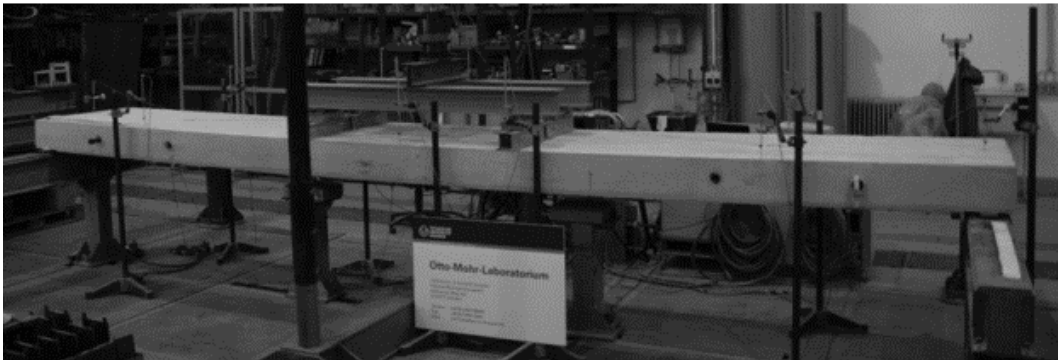


Figure 2.7. Test setup (Source: Schladitz et al., 2012)

Al-Salloum et al. (2011) performed an experimental study on seismic retrofitting of beam-column joints by using carbon-textile reinforced mortar (TRM), CFRP, and GFRP jackets. In this study, retrofitting methods were examined on seismically-deficient beam-column joints and compared with the unstrengthened reference specimens. The TRM and CFRP jackets were employed to increase the shear capacity of assemblages under quasi-static cyclic lateral loads (Figure 2.8). It is reported that TRM jackets were able to enhance the shear capacity and deformation capacity of inadequately reinforced beam-column joints for seismic loads. It is also reported that the energy dissipation capacity of specimens strengthened with the TRM jacket was significantly higher than the other members.

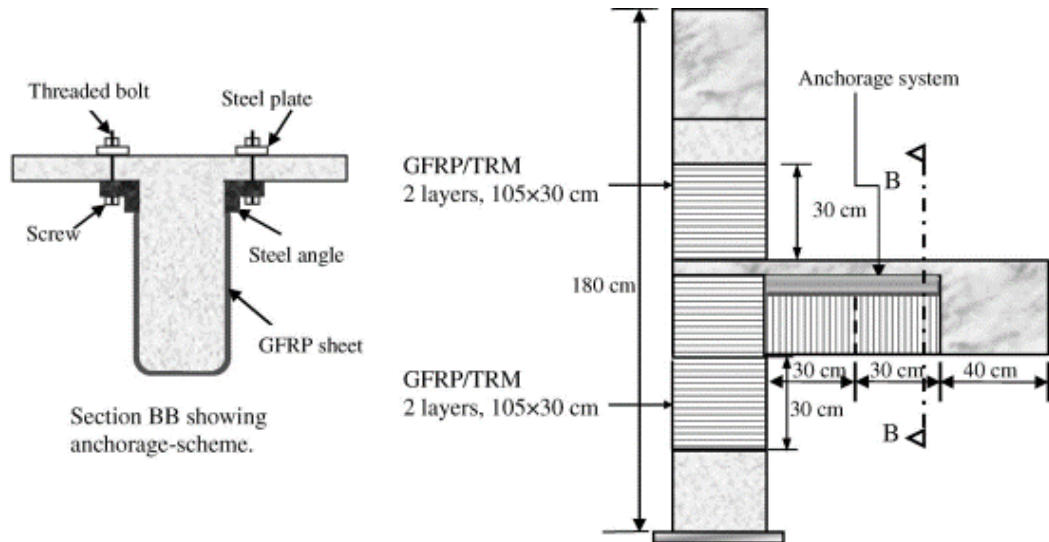


Figure 2.8. Schematic representation of assemblages (Source: Al-Salloum et al., 2011)

## 2.4. Research Significance of the Current Study

This literature review aims to provide an overview of the state-of-the-art studies related to the hard-impact behavior of RC structures, excluding studies with high-velocity impact conditions for military purposes. Therefore, experimental and numerical investigations on RC members with and without extra strengthening components are explained with the stated limitations.

In the literature, numerous experimental studies on impact behavior of RC structures were performed by researchers in a wide spectrum. When facilities at laboratories and institutions are considered for medium and large-scale testing capabilities in particular, most of the studies in the literature are set apart from each other and distinguished as high velocity-low mass impact and low velocity-high mass impact testing scenarios. Due to the limitations on medium and large-scale impact testing, a small number of such studies exist in the literature. Therefore, this presented study herein is attempting to provide an experimental work that situates in between these two testing scenarios, owing to an advanced impact testing facility. Moreover, studies on the low velocity-high mass impact scenarios were performed for overall behavior until excessive damage occurs, whereas high velocity-low mass scenario studies dealt with perforation limits at the first impact, in general. In addition to impact scenario of the presented experimental program in this thesis, RC slab specimens were

subjected to subsequent impact loads until the specimens were perforated which is rarely seen in the literature.

With the developments in material science and engineering, innovative solutions were started to take a stage in civil engineering applications and structures to create efficient, smart, and aesthetic structures for both civil engineering and architectural aspects. Textile reinforced concrete (TRC) is one of the relatively recent composites used for strengthening or retrofitting, as well as architectural purposes. Since research and studies on textile reinforced composites have been performed under other types of loadings such as static and cyclic loadings, the TRC elements and composites are started to be used for retrofitting, strengthening, or architectural purposes. However, hard impact behavior of TRC composites as strengthening or retrofitting layers is not investigated in detail yet. Therefore, it is believed that the presented study herein will contribute to the database of impact experiments, serving as either retrofitting or strengthening methods.

In addition to experimental work, a finite element analysis study was performed by using LS-DYNA software. Created models were examined by employing mesh sensitivity analyses and varied numerical erosion parameters. In the light of FE models verified by experimental data, a parametrical study is presented for different impact conditions to introduce impact scenarios where the textile reinforcements can play an efficient role. It is believed that these presented investigations will play a significant role in further studies on impact behavior of RC sections with textile reinforcements.

## CHAPTER 3

### EXPERIMENTAL PROGRAM

In the experimental program of this study, four reinforced concrete (RC) slabs, two unstrengthened and two strengthened with two different carbon textile reinforcements, were tested under repeated impact loads by means of the same steel striker. To assess the damage level induced by the striker with different velocities, two unstrengthened RC specimens were tested. In the light of these tests, the RC specimens with carbon textile strengthening layers were tested. The performed test program was aimed to design not only to reveal impact performance of RC slabs with and without strengthening, but to present detailed data sets with the help of advanced instrumentation and testing facility at Otto-Mohr Laboratorium of Technische Universität Dresden (TU Dresden).

#### 3.1. Test Specimens

All slab specimens were designed in uniform geometry with the same steel reinforcing ratios. These slab specimens with the dimensions of 1500 mm × 1500 mm × 200 mm were manufactured in Otto-Mohr Laboratorium of TU Dresden.  $\phi 8$  steel bars with 50.3 mm<sup>2</sup> cross-sectional area and 8 mm diameter were used. Spacing between steel reinforcements in both orthogonal directions was kept constant as 100 mm for all specimens. Strengthened specimens were reinforced with two different types of carbon textile reinforcements embedded in the additional 20 mm-thick fine-grained concrete layer, increasing the specimens' thickness to 220 mm in total. Figure 3.1 depicts the typical steel reinforcement layout for all slab specimens and a cross-sectional view for the strengthened specimens.

Specimens in the testing program were named in accordance with their textile reinforcement types when a strengthening layer was present. Figure 3.2 shows the convention for the specimen naming and the reinforcing details were given in Table 3.1. It should be noted here that the “T0” denotes the specimens without strengthening layers.

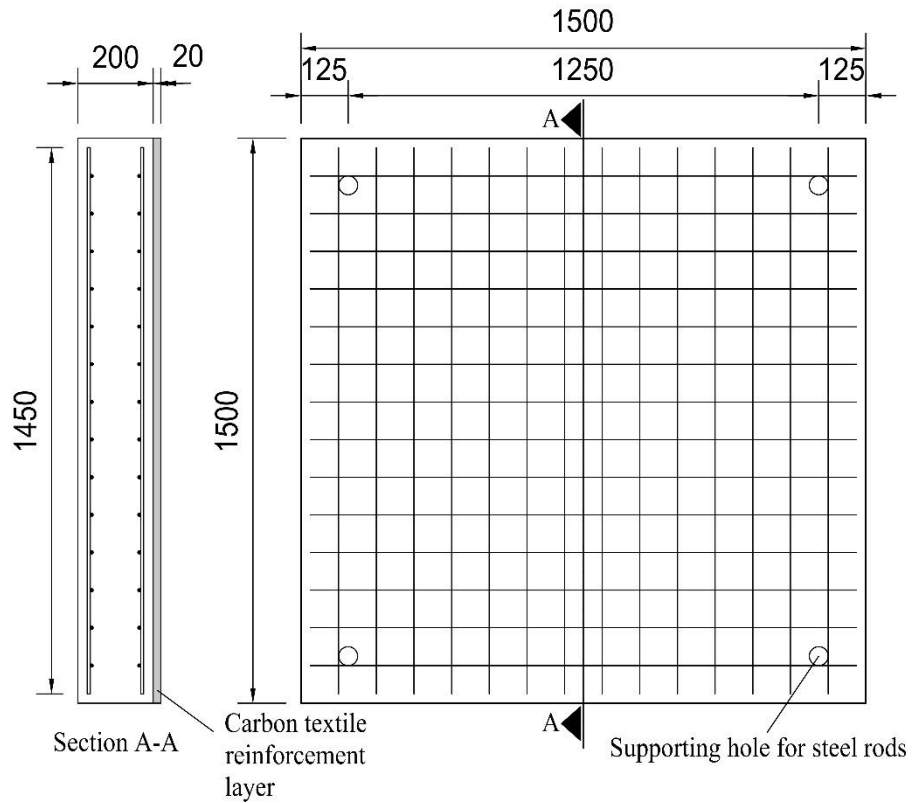


Figure 3.1. Typical steel reinforcement layout for all specimens and the cross-sectional view of strengthened specimens (dimensions in mm)

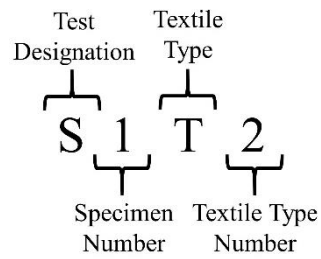


Figure 3.2. Naming conventions for test specimens

Table 3.1. Specimen details

Slab	Long. steel rebars / Spacing (mm)	Textile reinforcement / Number of layers
S1T0	$\phi 8 / 100$	None / None
S2T0	$\phi 8 / 100$	None / None
S3T1	$\phi 8 / 100$	Type1 / 1
S4T2	$\phi 8 / 100$	Type2 / 2 orthogonal

### 3.1.1. Construction of Specimens

As mentioned previously, the slab specimens were manufactured at the Otto-Mohr Laboratorium of TU Dresden. Steel reinforcement meshes were arranged by using  $\phi 8$  bars with equal spacing of 100 mm in each direction for the bottom and top layers. Bottom and top steel reinforcement meshes were formed separately and held together with the help of hangers placed at four corners of the specimens. Steel formworks were assembled at the backyard of the Otto-Mohr Laboratorium and all specimens were cast at the same time using the same batch ordered from a local company (see Figure 3.3). To specify concrete strength at testing dates, cylindrical test samples were taken into molds from the same batch and kept nearby the slab specimens under the same environmental conditions.



Figure 3.3. Specimen construction

As it can be seen from Figure 3.3, the bottom surface of the formwork for the strengthened specimens was covered with a retarder paper to apply strengthening layers of textile reinforcements. This paper has a plastic-coated, water-proof reverse side and the front side is coated with deactivator components which significantly decreases

setting time of concrete. After 24 hours past casting concrete, two specimens were lifted and the retarder papers were peeled off from their bottom surfaces. To obtain a rough surface for bonding between RC slabs and strengthening layers, the unset concrete at the bottom surfaces of the specimens was washed off by using a pressurized water nozzle (Figure 3.4a). After obtaining the rough surfaces for strengthening layers, these two specimens were strengthened with 2 cm-thick fine-grained concrete layers after seven days from the concrete casting date. Firstly, fine-grained concrete was plastered on the roughened bottom surfaces of specimens (Figure 3.4b). Then, textile reinforcements were placed on the fine-grained concrete layer (Figure 3.4c). Finally, the last layer of fine-grained concrete was plastered and 2 cm-thick strengthening layers were obtained as depicted in Figure 3.4d. The textile reinforcement with identical properties in both orthogonal directions (Type 1) was applied as a single reinforcing layer and embedded in two equal layers of fine-grained concrete. However, the amount of the textile reinforcement that has different properties in orthogonal directions (Type 2) was doubled as two reinforcing layers and embedded in three equal layers of fine-grained concrete. In this specimen, two layers of textile reinforcements were placed orthogonally in between three equal layers to provide symmetrical reinforcing ratios in both directions.

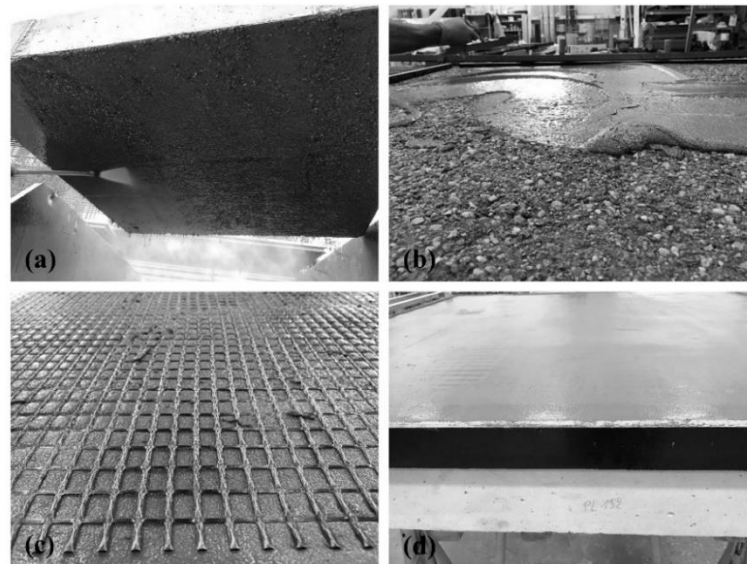


Figure 3.4. Application of strengthening layer to bottom face of RC slab: a) washing of unset concrete; b) plastering fine-aggregated concrete; c) placing textile reinforcements; d) finished specimen

### 3.2. Test Facility

As mentioned before, the experimental phase of this study was carried out by using an advanced testing facility that was designed and manufactured for the Institute of Concrete Structures, TU Dresden. Owing to its design, the testing facility can be run for two types of impact loadings, free fall of weights (Kühn & Curbach, 2015) and accelerated strikers (Hering et al., 2020). In this experimental investigation, manufactured specimens were subjected to a steel striker accelerated via controllable air pressure stored in the tanks from the top of the testing tower. An illustration of the testing facility can be seen in Figure 3.5.

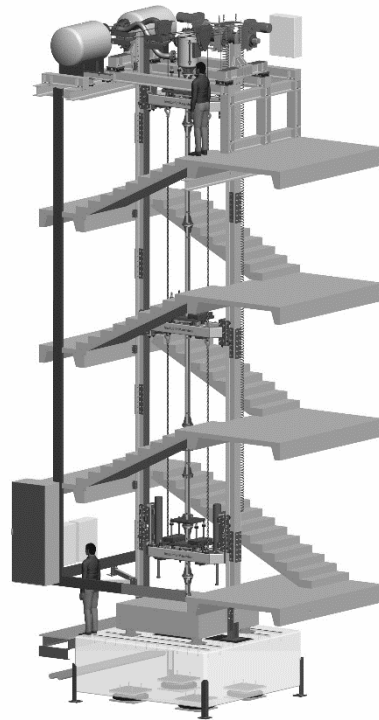


Figure 3.5. Testing facility (Batarlar et al., 2020)

The support conditions of the testing facility were designed as fixed-supports at four corners of specimens, providing a 1250 mm clear span for each edge of specimens. Specimens were placed on supports with circular rigid steel plate and fixed by  $\phi 28$  steel connection rods passing through slab specimens (Figure 3.6). Support conditions of the test facility with and without test specimen can be seen in Figure 3.7.

All slab specimens were tested by using the same cylindrical flat-surface steel striker with the 380 mm length and 21.67 kg mass. The diameter of striker was selected in accordance with the pipe diameter of testing facility, which is 100 mm. Contact velocity of striker was measured by using two light barriers, one installed at the exit point and the other installed 380 mm above the exit in the pipeline where the striker traveled through during impacts.

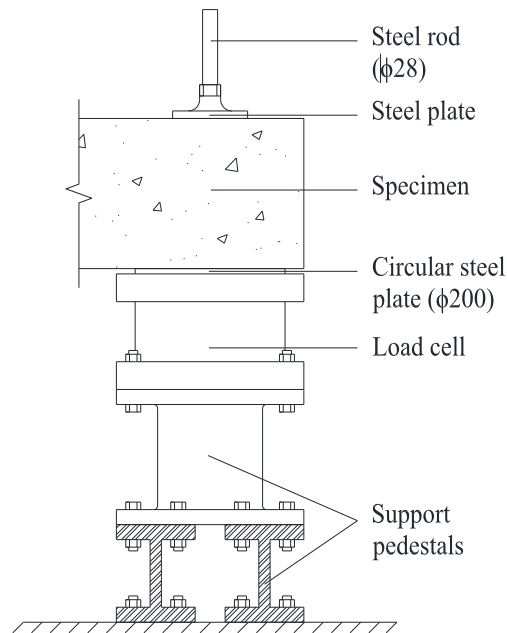


Figure 3.6. Details of support conditions

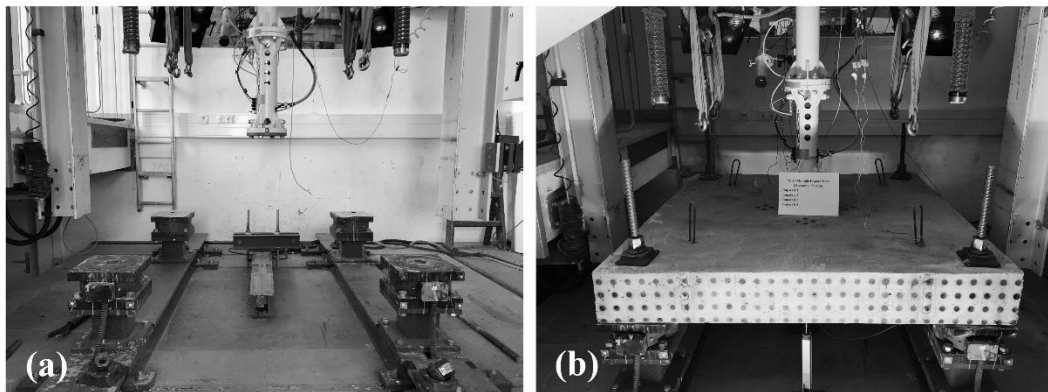


Figure 3.7. The support conditions of testing facility: a) without test specimen; b) with test specimen

### 3.3. Materials

The materials used for manufacturing RC slab specimens were explained in this section. To evaluate the mechanical properties of the materials, testing methods were performed according to universal standards.

#### 3.3.1. Concrete

As mentioned previously, concrete used in manufacturing slab specimens was ordered from a local concrete company with concrete class of C35/45. During casting, standard cylinder samples with dimensions of 150 mm in diameter and 300 mm in height were taken and kept alongside slab specimens, exposing them to same conditions. These samples were tested on the 28<sup>th</sup> and 42<sup>nd</sup> day of casting. Compressive strength and elastic modulus of these samples were presented in Table 3.2. It should be noted here that the splitting tests to evaluate the tensile strength of concrete were performed only on the 42<sup>nd</sup> day.

Table 3.2. Cylinder tests results

	28 <sup>th</sup> day		42 <sup>nd</sup> day		
	Peak Compressive Strength, $f'_c$ (MPa)	Elastic Modulus (MPa)	Peak Compressive Strength, $f'_c$ (MPa)	Elastic Modulus (MPa)	Splitting Tensile Strength, $f_r$ (MPa)
Standard cylinder samples	34.9	24500	31.5	23300	1.85
	34.2	24800	33.0	23900	1.65
	34.6	26400	33.6	23900	2.01
	33.5	N/A	31.8	N/A	N/A
<i>Mean</i>	<i>34.3</i>	<i>25233</i>	<i>32.5</i>	<i>23700</i>	<i>1.84</i>

Strengthened specimens were externally reinforced with carbon textile reinforcements embedded in a fine-grained concrete matrix. To obtain the matrix, a ready-mix mortar with a brand name of TF 10 PAGEL (a product of PAGEL Spezial-Beton GMBH & Co.) with a maximum aggregate size of 1 mm was used. To specify the mechanical properties of fine-grained concrete, prism samples with the dimensions of 40 mm × 40 mm × 160 mm were taken and tested to define the compressive and

flexural strength of fine-grained concrete according to ASTM C109 and ASTM C348, respectively (Figure 3.8). Results of these tests are tabulated in Table 3.3.

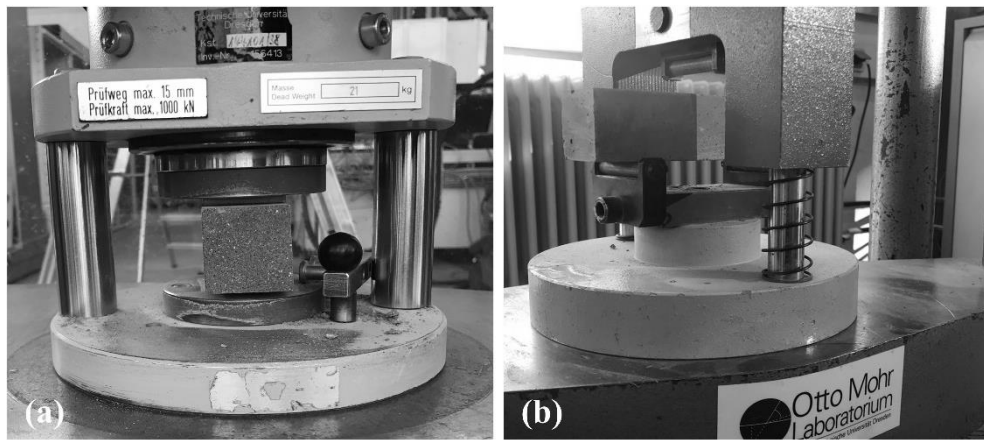


Figure 3.8. Standard tests for fine-grained concrete according to the ASTM: a) compressive strength test; b) three-point flexural strength test

Table 3.3. Standard test results for fine-grained concrete

	28 <sup>th</sup> day	
	Peak Compressive Strength, $f'_c$ (MPa)	Peak Flexural Strength, $f_f$ (MPa)
Standard test samples	90.1	6.1
	90.7	6.3
	82.6	7.1
	85.9	8.0
	81.7	8.0
	83.9	7.6
	86.3	N/A
	93.4	N/A
	85.7	N/A
	93.4	N/A
	87.3	N/A
87.1	N/A	
<i>Mean</i>	87.3	7.2

### 3.3.2. Steel Reinforcement

Steel reinforcements used in slab specimens were ordered from a local company. Mechanical properties of steel reinforcements were provided by the company according to DIN 488-1:2009. Accordingly, yield stress, rupture stress, and modulus of elasticity were 500 MPa, 650 MPa and 200000 MPa, respectively.

### 3.3.3. Carbon Textile Reinforcements

As explained before, strengthening layers were applied only to the bottom face of RC slab specimens externally by means of carbon textile reinforcements embedded in a 2 cm-thick fine-grained concrete matrix. Two types of carbon textile reinforcements were selected for strengthening layers. These textile reinforcements depicted in Figure 3.9 differ from each other according to their geometry in weft and warp directions as well as their mechanical properties.

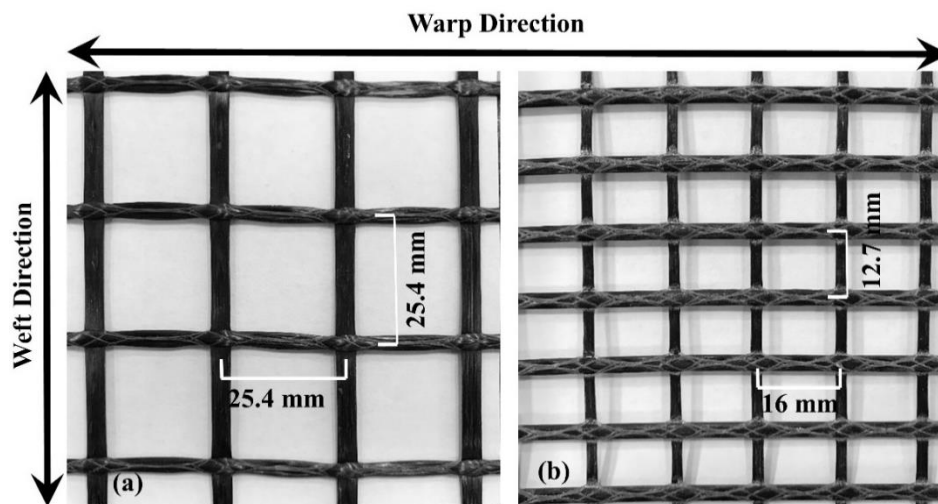


Figure 3.9. The carbon textile reinforcements: a) Type 1, and b) Type 2

As it can be clearly seen from Figure 3.9, Type 1 textile reinforcement has uniform geometrical properties (25.4 mm in both directions), whereas Type 2 textile reinforcement has different spacing between strands (16 mm in warp directions and 12.7 mm in weft directions). Therefore, to provide equal textile reinforcement ratios in each direction, two layers of Type 2 textile reinforcement, positioned orthogonal to each other, were embedded in between three equal depth fine-grained matrix layers. In

addition to its geometrical asymmetry, number of filaments in warp and weft directions also varies in each strand. Number of carbon filaments in warp directions for Type 2 textile is 48000, whereas filament number in weft direction is one-fourth of the warp direction, 12000. It should be reminded here that other strengthened slab specimen was strengthened by using only one layer of the Type 1 carbon textile reinforcement owing to its uniform geometry and filament number in each direction which is 48000.

To specify tensile properties of carbon textile concrete composites such as modulus of elasticity, tensile strength, and strain, ten test samples of carbon textile reinforcements embedded in fine-grained concrete were produced with dimensions of 15 mm × 75 mm × 1100 mm for each type of carbon textile reinforcement, and tested in accordance with the ACI 549.4R-13 and AC 434 specifications. Additionally, recommendations for testing methods of carbon textile-reinforced concrete conducted by Schutze et al. (2018) were taken into considerations to obtain tensile load bearing behavior of textile-reinforced concrete (see Figure 3.10).

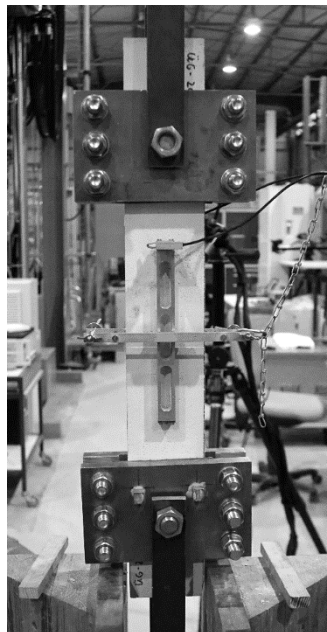


Figure 3.10. Typical tensile test of textile-reinforced concrete sample

Stress-strain profiles of test specimens under uniaxial tensile load were presented in Figure 3.11 and Figure 3.12. It should be noted here that the presented profiles belong to the specimens tested under uniaxial loads in the warp directions of textile reinforcement. As it can be seen from the profiles, stress-strain profiles showed steeper curve until cracks in concrete matrix occurred. After multiple cracking governed

in the sections, pure strand behavior was observed until rupture. The modulus of elasticity, tensile strength and strain values are tabulated in Table 3.4.

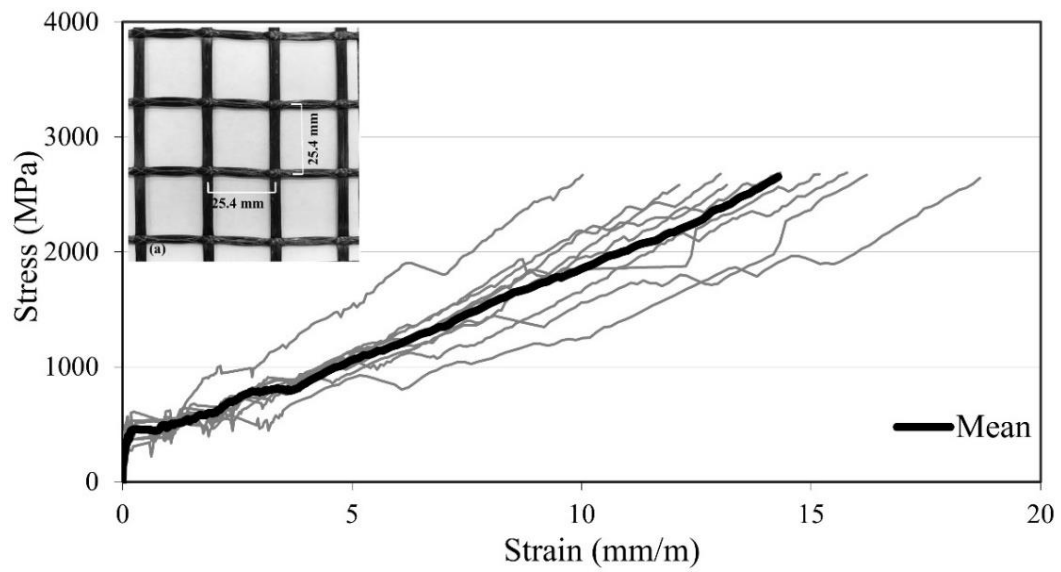


Figure 3.11. Stress-strain profiles of test samples with Type 1 for uniaxial tensile test

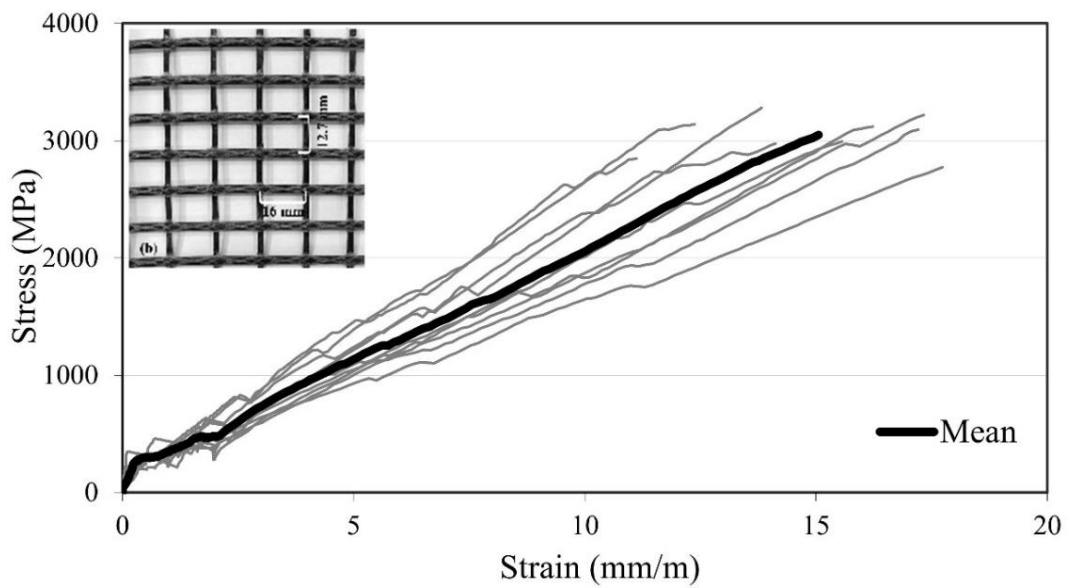


Figure 3.12. Stress-strain profiles of test samples with Type 2 for uniaxial tensile test

Table 3.4. Material properties of the textile reinforcements

Carbon textile reinf.	Filament # in warp/weft directions	Area of a strand in warp/weft directions (mm <sup>2</sup> )	Mean tensile strength & strain in warp direction (MPa / mm/m)	Elastic modulus in warp direction (MPa)
Type 1	48 K / 48 K	1.83 / 1.83	2660 / 14.28	187000
Type 2	48 K / 12 K	1.83 / 0.92	3052 / 15.40	198000

### 3.4. Instrumentation

To present a well-documented behavior of slab specimens under impacts, instrumentation layout was meticulously designed. In this section, employed instrumentations were presented used for measuring the reaction forces, displacements, accelerations, and strains.

#### 3.4.1. Load Cells

As explained in section 3.2, slab specimens were supported at the corners by means of steel plates and connection rods passing through specimens and fixed by steel plates. With aim of measuring the reaction profiles during impact events, load cells were developed by using full-bridge semi-conductor strain gauges and located beneath the supporting steel plates (Hering et al., 2020). These self-developed load cells were fixed to the rigid foundation with the help of steel support pedestals ( see Figure 3.13). Each load cell located at the support has a 10000 kN capacity.

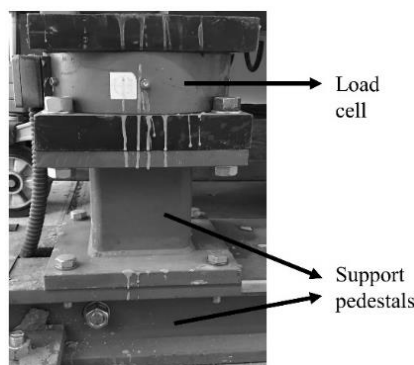


Figure 3.13. Load cell at the support

### 3.4.2. Laser Displacement Sensors

To capture displacement-time histories during impacts, two contactless laser displacement sensors were located on the rigid foundation of the testing facility with transparent protective covers, facing the bottom surface of slab specimens. Measurement points, the midpoint of specimen (L1) and the middle point between supports (L2), were presented in Figure 3.14. These laser sensors were the products of WayCon Positionmesstechnik GmbH with a measurement range of 0.5 mm to 200 mm and 400 kHz measuring frequency capacity.

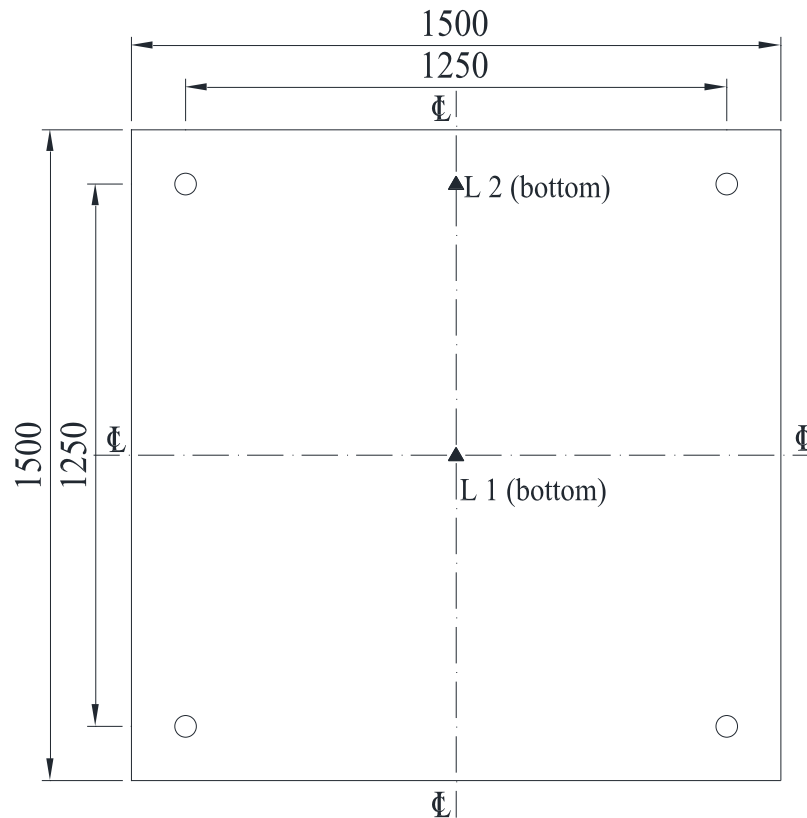


Figure 3.14. The measurement points of the laser displacement sensors (all dimensions in mm)

### 3.4.3. Accelerometers

Accelerations during impact tests were captured by using PCB Piezotronics Inc. accelerometers with a capacity of  $\pm 5000g$ . Acceleration data were gathered from four points in total, three points on the top of the specimen, and one point in the middle of

the specimen on the bottom face (Figure 3.15). All accelerometers were mounted on a metal base before attaching to the specimens. Then, this metal base was glued to the specimens by using a super adhesive material to avoid detachment during impact (Figure 3.16).

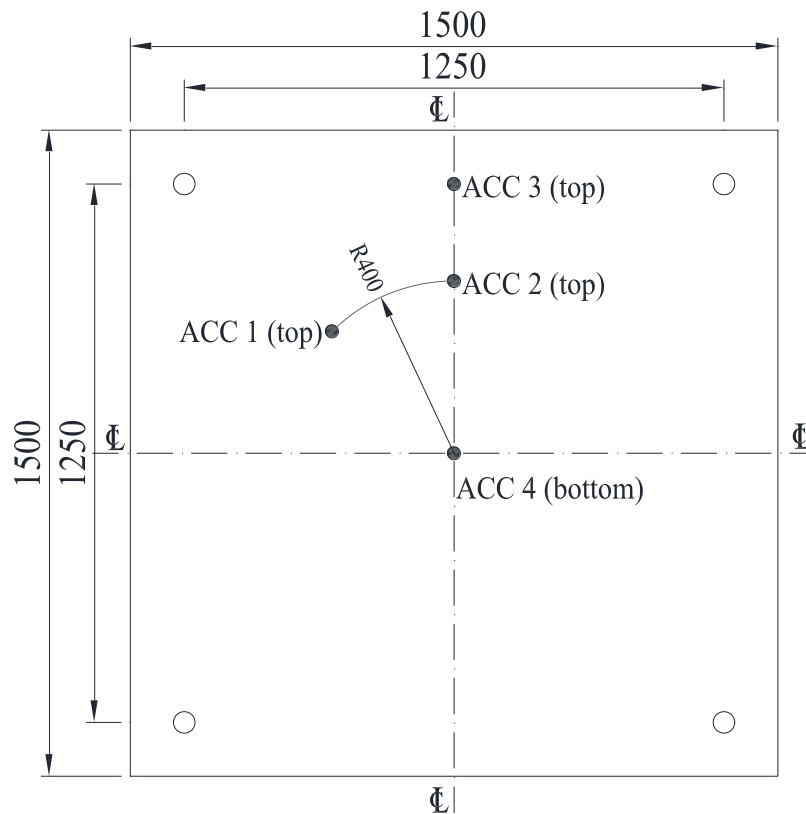


Figure 3.15. The locations of accelerometers (all dimensions in mm)

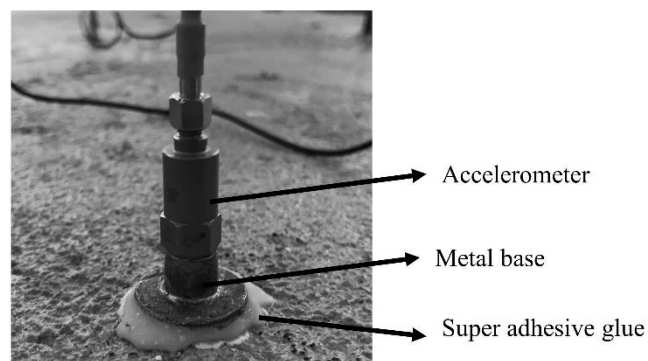


Figure 3.16. The application of accelerometer

### 3.4.4. Strain Gauges

Four strain gauges were attached to steel bars of the bottom reinforcing mesh around the impact vicinity. Attachment points on steel reinforcing bars were lightly ground and cleaned. All strain gauges were coated after they were glued to steel reinforcing bars to make them fully isolated (Figure 3.17). Strain gauges used were products of BCM sensor Technologies BVBA with a capacity of  $6000 \mu\epsilon$ . Locations of the attached strain gauges on the bottom reinforcements are displayed in Figure 3.18.



Figure 3.17. Final view of a strain gauge

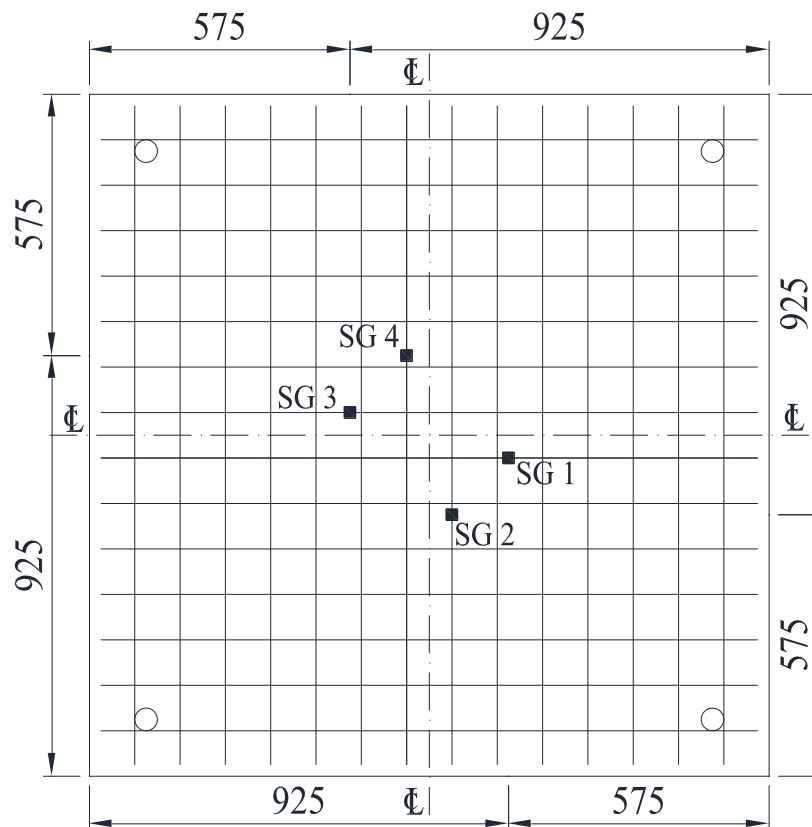


Figure 3.18. The locations of strain gauges attached on bottom reinforcing mesh (all dimensions in mm)

### 3.4.5. High-Speed Camera

During tests, the entire impact event was recorded by using two high-speed cameras with different shooting angles. One of these high-speed cameras was located across specimen to capture impact behavior of specimen from side (Figure 3.19a), and another high-speed camera was diagonally placed above specimen to capture impact from the top (Figure 3.19b). Both employed high-speed cameras have a capacity of 10000 fps sampling rate.

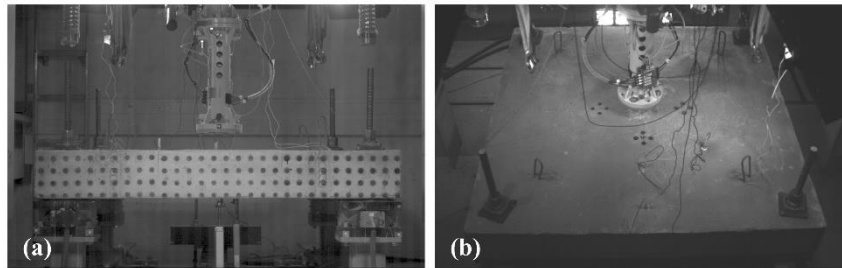


Figure 3.19. High-speed camera views: a) side view; b) top view

### 3.4.6. Data Acquisition System

To capture data that occurred in impact tests, a high-speed data acquisition system with a 200 kHz measuring rate for each channel was used for recording and capturing data.

## 3.5. Impact Tests

As previously mentioned, one of the aims of this testing program was to reveal carbon textile reinforcements' contributions to hard-impact behavior of RC slab specimens by providing a well-documented data. To do that, velocity of the striker was determined with the intent of avoiding total perforation of the specimens at the first impact. Therefore, the bottom limit of the testing facility was configured for accelerating the steel striker. The unstrengthened specimens, S1T0 and S2T0, were employed to determine the damage levels under impacts by using the same steel striker with two different velocities. In the light of these tests, specimens strengthened with carbon textile reinforcements were subjected to the same steel striker with the same

contact velocity several times until total perforation occurred. During subsequent impact tests of each slab specimen, the velocity of the striker was kept same. Table 3.5 presents the specimens subjected to several impacts by the steel striker with average velocity and final damage levels after the impacts.

Table 3.5. Test protocol

Slab	Number of impacts	Avg. contact velocity (m/s)	Final damage level
S1T0	2	25.6	Shear plug failure
S2T0	2	30.0	Excessive damage
S3T1	4	26.0	Total perforation
S4T2	6	25.8	Total perforation

### 3.5.1. S1T0 Specimen

The S1T0 was one of the unstrengthened specimens that was subjected to two impacts until plugging of the punching cone was observed.

#### S1T0-1 Test

In the first impact test, the specimen was subjected to the steel striker with a 25.9 m/s contact velocity. Visible cracks were observed, marked, and photographed after the impact event. Concrete scabbing from bottom and top faces of the specimen was not observed whereas a 5 mm of striker penetration was measured.

#### S1T0-2 Test

In the second impact test, the steel striker with 25.3 m/s contact velocity caused 4 kg of concrete scabbing at the bottom face. The steel reinforcements at the bottom face were visible and the punching cone formation became apparent after the impact. The striker penetration was observed as 20 mm, in total. The final state of the S1T0 specimen can be seen in Figure 3.20.

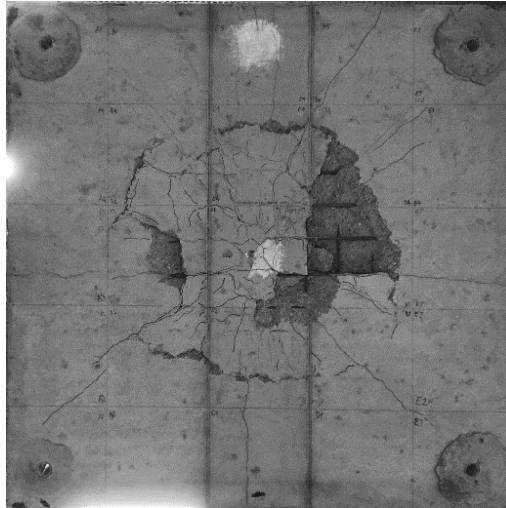


Figure 3.20. The final state of the S1T0 specimen

### **3.5.2. S2T0 Specimen**

Another unstrengthened specimen, S2T0, was subjected to impacts by using the same steel striker with increased contact velocity. Similar to the previous specimen, S2T0 was tested under two consecutive impacts.

#### **S2T0-1 Test**

The specimen S2T0 was subjected to impact of the steel striker with 30.2 m/s contact velocity. Apparent crack formation and slight concrete scabbing were observed on the punching cone boundaries. The penetration depth of striker was measured as 7 mm.

#### **S2T0-2 Test**

In the subsequent impact test of S2T0 specimen, the contact velocity of striker was 29.7 m/s, causing excessive scabbing on the bottom surface. The total mass of the scabbed concrete from the bottom and top surface of specimen was 14.6 kilograms. Most of the steel reinforcing bars at the vicinity of punching cone became visible. The total penetration of steel striker was measured as 63 mm after the second impact event. The final state of the S2T0 specimen was depicted in Figure 3.21

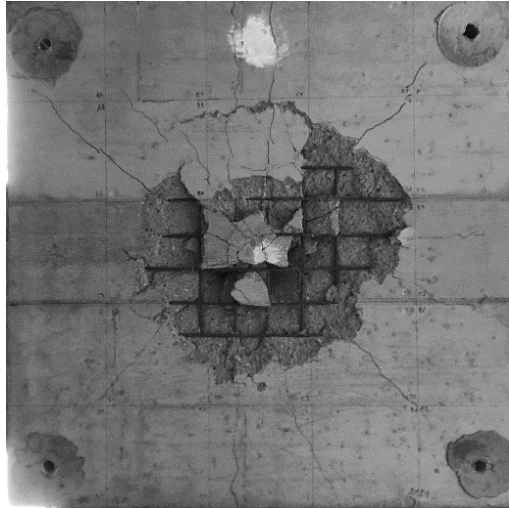


Figure 3.21. The final state of the S2T0 specimen

### **3.5.3. S3T1 Specimen**

The specimen strengthened with Type1 carbon textile reinforcement was subjected to impacts until it was perforated by the steel striker. This specimen survived three consecutive impacts and total perforation occurred at the fourth impact.

#### **S3T1-1 Test**

In the first impact test of S3T1 specimen, the contact velocity of striker was measured as 26.0 m/s, resulting in a 5 mm penetration depth. Visible crack formations were observed at the bottom face similar to unstrengthened specimens. Also, circumferential cracks around the punching cone were apparent. Concrete scabbing was not observed.

#### **S3T1-2 Test**

In this test, the contact velocity of steel striker and its penetration depth were identical with the previous test, 26.0 m/s and 10 mm in total, respectively. Some concrete parts scabbed slightly at the punching cone boundaries. A few number of new cracks formed in the punching cone area.

#### **S3T1-3 Test**

At the third impact, more than half of the fine-grained concrete parts scabbed from the punching cone area, and strands of carbon textile reinforcement became

visible. Total mass of scabbed fine-grained concrete was 3.9 kilograms. The striker contact velocity was 26.2 m/s and the penetration depth was measured as 29 mm in total.

#### **S3T1-4 Test**

The S3T1 specimen was totally perforated by the steel striker with 25.4 m/s contact velocity at the fourth impact. The mass of scabbed concrete was 4.5 kg in this impact event. The final state of the S3T1 specimen after tests can be seen in Figure 3.22.

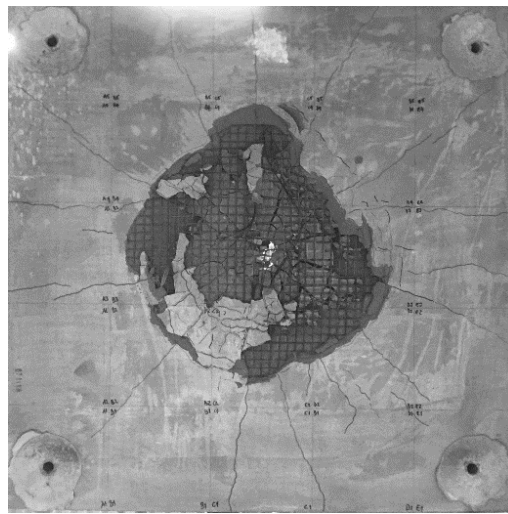


Figure 3.22. The final state of the S3T1 specimen

#### **3.5.4. S4T2 Specimen**

Similar to specimen S3T1, specimen S4T2 was tested under consecutive impacts until total perforation occurred. Owing to its higher carbon textile reinforcement ratio compared to S3T1 specimen, it resisted five consecutive impacts and perforation occurred at the sixth impact test.

#### **S4T2-1 Test**

Specimen S4T2 was subjected to the steel striker with 26 m/s contact velocity, causing 6 mm of penetration depth. Numerous visible cracks were observed and marked. Similar to other specimens, circumferential cracks were observed around punching cone perimeter.

#### **S4T2-2 Test**

Similar to the previous impact event, steel striker with 25.9 m/s contact velocity could penetrate 10 mm, in total. No concrete scabbing on either face of the specimen was observed in the second test.

#### **S4T2-3 Test**

In the third subsequent impact test, S4T2 specimen was subjected to the steel striker with a 25.9 m/s contact velocity. As in previous tests, no concrete scabbing was observed and the penetration depth increased to 18 mm, in total.

#### **S4T2-4 Test**

At the fourth impact, the steel striker with a 25.4 m/s contact velocity could cause only slight concrete scabbing on the punching cone perimeter. The mass of scabbed concrete was 2.1 kilograms. The penetration depth was measured as 34 mm, in total.

#### **S4T2-5 Test**

S4T2 was the strongest specimen owing to its higher carbon textile reinforcement ratio and it resisted the fifth impact of the steel striker with a 26 m/s contact velocity. However, the penetration depth increased significantly to 110 mm, in total. A little amount of concrete scabbing, 0.3 kilograms, was observed.

#### **S4T2-6 Test**

S4T2 could not stand the impact load imparted by the steel striker with a 25.9 m/s contact velocity at the sixth test, and it was finally perforated. At the last test, the mass of scabbed concrete from the bottom face was increased to 7 kg. The final state of the specimen S4T2 is depicted in Figure 3.23.

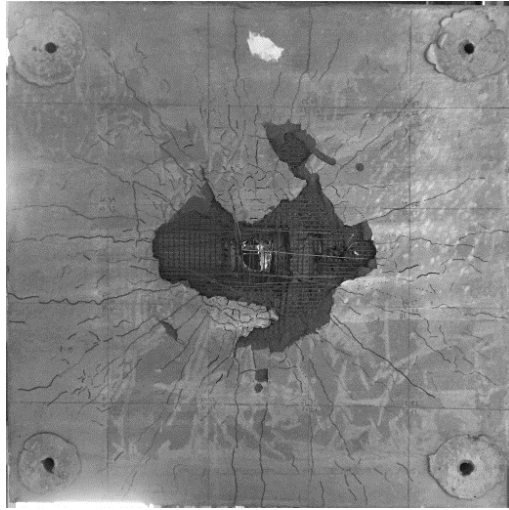


Figure 3.23. The final state of the S4T2 specimen

### 3.5.5. The Punching Cone Observations

As mentioned earlier, each employed slab specimen was cut into two equal pieces from their middle axes to present the punching cone geometry. The cross-sectional views of all slab specimens can be seen in Figure 3.24.

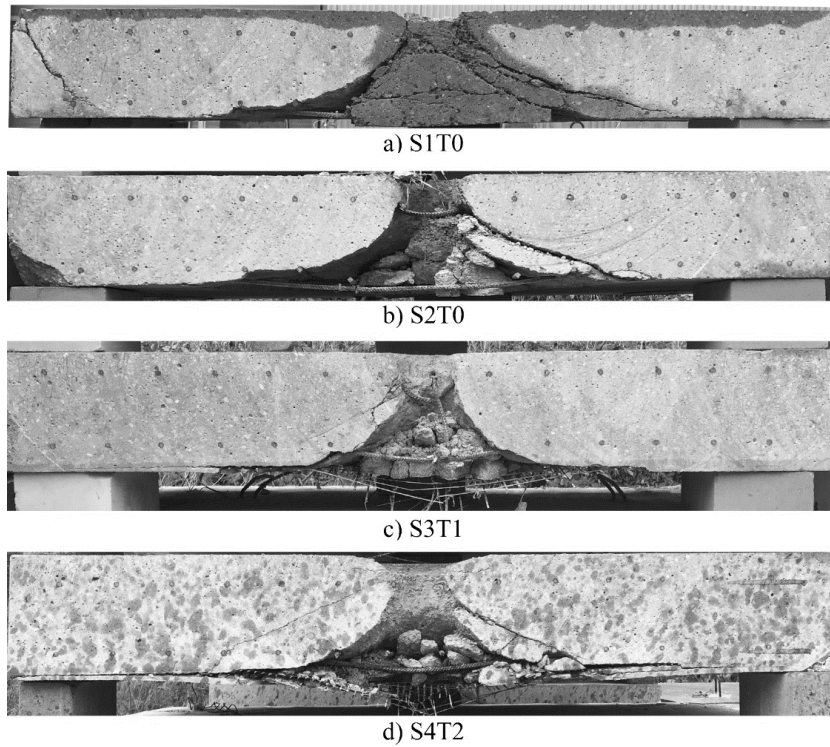


Figure 3.24. Slab specimens after being cut into half

## **CHAPTER 4**

### **TEST RESULTS AND DISCUSSION**

The methods, techniques, and instrumentation used in the experimental stages of this study are explained in the previous chapter. As mentioned earlier, the experimental program was designed to gather information with the aim of presenting well-documented data sets on the impact behavior of RC slabs strengthened with carbon textile reinforcements. Hence, in this chapter, collected data from the experimental program were analyzed and the results and outcomes are discussed.

#### **4.1. Impact Test Observations**

To assess the damage state of the specimens after each impact, specimens were examined and visual observations were made carefully. To obtain crack profiles of specimens, developed cracks were marked and photographed after each impact event. During tests, crack formations were observed only for the bottom face of the specimens. Therefore, here, only crack patterns belonging to the bottom surface were illustrated. Due to supporting conditions, the cracks formed at the support regions were not visible until the testing protocol was completed. In addition to the crack profiles of the specimens, the penetration depths of striker were measured in each impact test. After testing the specimens according to loading protocol, each specimen was cut along its middle axis to observe the punching cone formation and its boundaries which are presented in the previous chapter.

In this section, observations from each impact event were presented referring to the selected crack profile illustrations of tested specimens. Crack profiles of specimens for each impact test can be also found in Appendix A.

##### **4.1.1. S1T0 Specimen**

The series of impact tests were initiated by employing the S1T0 specimen which was remained unstrengthened. As explained before, this specimen was employed to

observe damage levels caused by the steel striker and to decide the striker velocity accordingly for further impacts.

In the first impact test, the steel striker with 25.9 m/s contact velocity caused barely visible hairline cracks on the bottom surface of the specimen. These observed cracks on the bottom surface were mostly located at the middle and a few circular crack formation was observed as a sign of punching cone geometry. In addition to these cracks, visible crack formation developed on the diagonals and middle axes on the bottom surface of S1T0 specimen which can be seen from Figure 4.1a. After the first impact, no cracks were observed on the top surface, whereas 5 mm of penetration depth was measured.

The following impact via the same striker with 25.3 m/s contact velocity caused concrete scabbing in the punching cone area. In addition to newer crack formations in the punching cone vicinity. Inherited cracks both in the punching cone region and along the axes were widened (Figure 4.1b). Due to concrete scabbing, steel reinforcements became apparent. Similar to the previous test, no cracks were observed on the top, however, 20 mm of penetration depth was observed, in total.

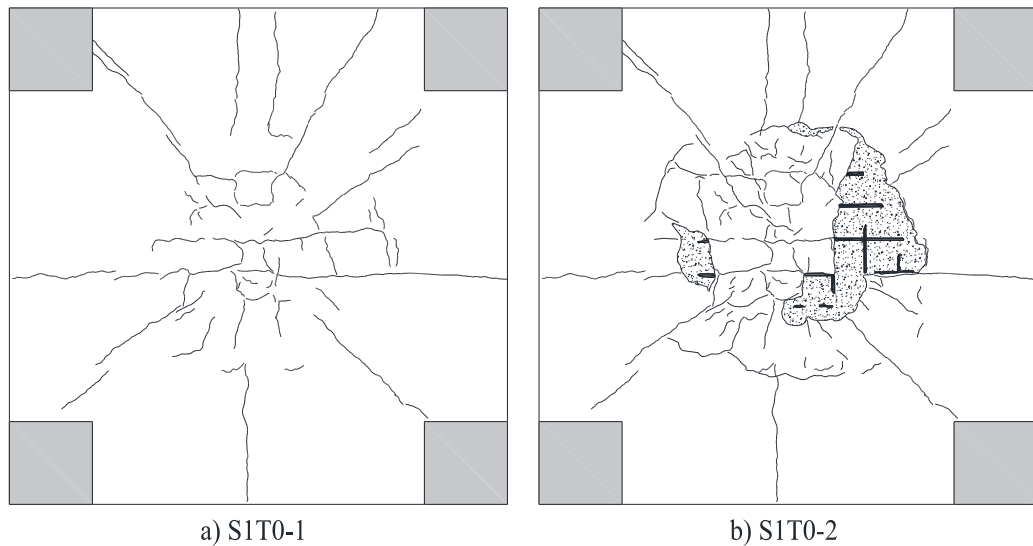


Figure 4.1. S1T0 specimen bottom face crack profiles after the first and final impacts

### 4.1.2. S2T0 Specimen

The impact test series was followed by employing the other unstrengthened specimen which was subjected to two consecutive impacts by the same steel striker with the increased contact velocity. In the first test, S2T0 specimen was hit by the striker with 30.2 m/s contact velocity. Similar to the first impact test of S1T0 specimen, the cracks were mostly developed at the punching cone region. Also, the crack formations on the diagonals and middle axes were observed analogously to the previous specimen. As a result of increased impact energy, wider cracks were observed and the punching cone geometry was more prominent at the bottom surface of S2T0 specimen compared to S1T0 (Figure 4.2a) at the first impact test.

At the second impact test, the steel striker with 29.7 m/s contact velocity could penetrate 63 mm into the specimen in total and caused excessive scabbing at the back face. As it can be seen from Figure 4.2b, concrete at the punching cone region scabbed considerably and the steel reinforcing bars became apparent. Newer crack formation was not observed. Similar to the previous specimen, inherited cracks became wider.

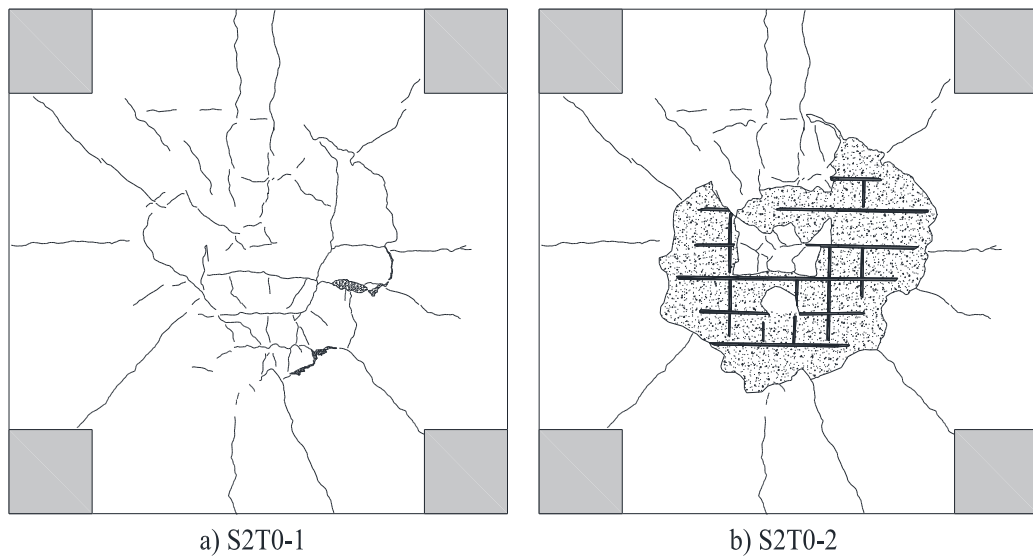


Figure 4.2. S2T0 specimen bottom face crack profiles after the first and final impacts

### 4.1.3. S3T1 Specimen

As mentioned earlier, in the light of unstrengthened specimens' tests, the specimens strengthened with carbon-textile reinforcements were decided to be tested by

using the same steel striker with the same contact velocity as in the tests of S1T0 with the aim of preventing excessive damage in the second impact test. The S3T1 specimen was subjected to impact loads until total perforation occurred. At the first impact test, hairline cracks were developed at the bottom face of the specimen. As it can be seen from Figure 4.3a, the circular cracks and the cracks on diagonals and middle axes were developed similar to unstrengthened specimens. In addition to this similarity, circular crack formation as a sign of punching cone geometry was explicit and trackable. Also, developed cracks on diagonals and middle axes were obvious, originating from the midpoint and reaching to the edges continuously.

The second and third impacts did not cause any newer crack formation, however, the inherited cracks from the first test were wider. Concrete scabbed slightly on the boundaries of the outer circular crack formations at the second impact, whereas most of the concrete in punching cone scabbed after the third impact. The crack formations for the second and third impact tests were presented in Appendix A.

The S3T1 specimen could be perforated at the fourth impact by the steel striker with 25.4 m/s contact velocity. Similarly, newer cracks were not observed and the major part of concrete in the punching cone region scabbed, exposing the carbon textile reinforcements.

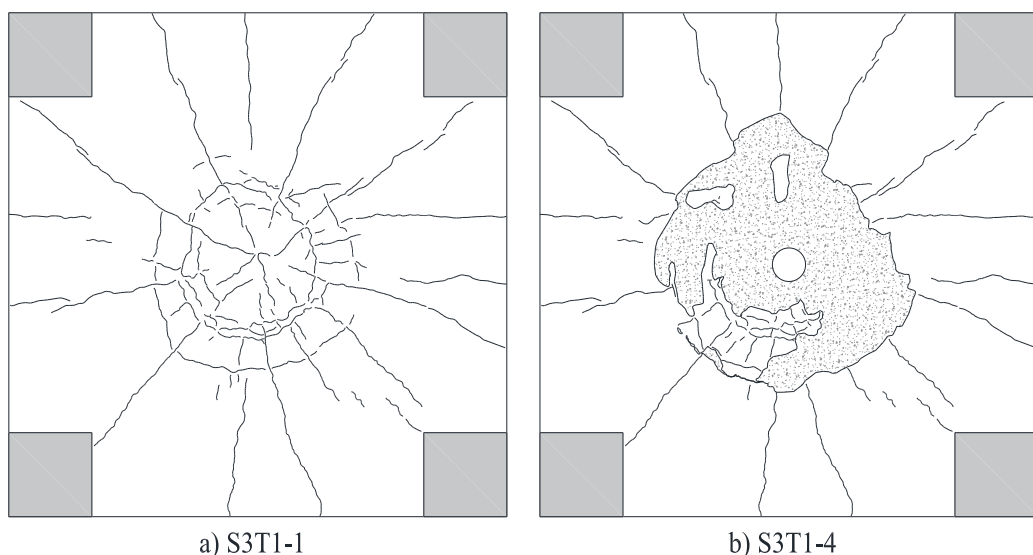


Figure 4.3. S3T1 specimen bottom face crack profiles after the first and final impacts

#### 4.1.4. S4T2 Specimen

The last one, S4T2 specimen, with the highest textile reinforcement ratio was subjected to six consecutive impacts until the total perforation failure occurred. At the first impact test of this specimen, hairline cracks were developed similarly to the others. However, the crack formation was more distributed and denser compared to the previous specimens. As it can be seen from Figure 4.4a, crack on diagonals and middle axes formed as well as circular cracks in the punching cone region similar to the other specimens. In addition to these cracks, various discontinuous cracks scatter on the bottom face of the specimen. Most of the developed cracks were barely visible and very narrow.

Starting from the following impact test, the cracks were widening and they became apparent. Similar to other impact tests, newer cracks were not observed in the subsequent impacts. No concrete scabbing occurred until the fourth impact. At the fourth impact, concrete parts scabbed around the punching cone perimeter. Even though the fifth impact caused excessive bulging in the punching cone region, the amount of scabbed concrete slightly increased. Finally, the steel striker could pierce the specimen at the sixth impact and caused major concrete scabbing in the punching cone region (Figure 4.4b). The crack formations belonging to each impact event for S4T2 specimen can be seen in Appendix A.

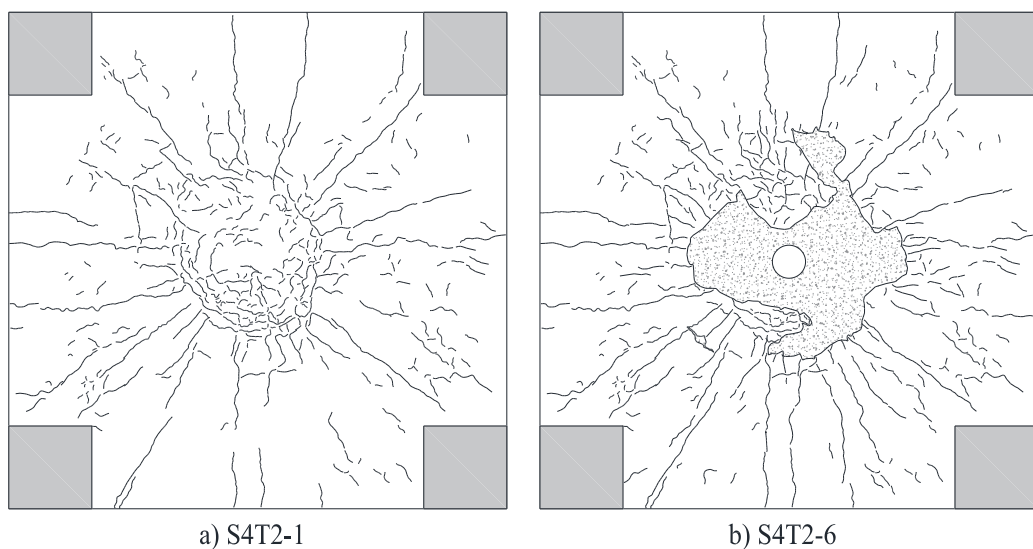


Figure 4.4. S4T2 specimen bottom face crack profiles after the first and final impacts

## 4.2. Digital Signal and Data Analysis

As mentioned earlier, one of the objects of this experimental research is to present a well-documented data recorded during the impact tests. For this purpose, a well-instrumented experimental program was designed and the data collected via instrumentation was examined for presenting the results as response-time histories.

Dynamic loading cases such as blast, impact or shock happen in the blink of an eye due to their nature of the event. As a result of this quick event, structural response generally takes place in extremely short time interval. Therefore, the instrumentation become more of an issue to present reliable and accurate measurements and results. Thus, the reliability and accuracy of instrumentation were investigated by Saatci (2006) and Hrynyk (2013), regarding their impact studies on RC members. Similarly, in this study, the capability of instrumentation was assessed by using the same signal processing method.

Since the duration of impact event is extremely short, higher sampling rates are employed in testing. As a result, a very large amount of data is recorded with redundant portions in data sets. To handle the recorded data to a reasonable extent, unnecessary portions were manually scanned and clipped for each impact event to reduce data size. With the help of the MATLAB (Mathworks, 2018) program, collected data were trimmed, starting from just prior to impact event and until the specimens become still.

To investigate the frequency content of the collected data, power spectra were derived by a simple code written in the MATLAB environment using the Fast Fourier Transform (FFT) method. Evaluation of the developed spectrums revealed that the high-frequency content of collected data is quite insignificant and low-frequency content that belongs to major vibrations of the specimens were successfully captured within the sampling rate limitations of the data acquisition system. Power spectra were also used to define the filtering frequencies of each measurement signal. In signal processing, filtering can be sometimes unavoidable due to noisy data sets. Therefore, a simple code was written in the MATLAB environment by employing the *'filtfilt'* function that enables a zero-phase difference filter design with a variety of bandpass, cut-off frequency, and filtering order. The outcomes and the filtering process of signals are explained particularly for each data measurement.

One of the noisy signals was the data collected from the laser sensors to measure displacements during the impact tests. As depicted in Figure 4.5a and Figure 4.5b, the collected raw signals shown in gray lines were significantly noisy and the filtering process was inevitable. According to the developed power spectrum, the contribution of the measured signals was significantly dropping beyond the 0.2 kHz and the amplitude reached the peak at 0.01 kHz. Therefore, a filter design was constructed by using MATLAB function in the light of the developed power spectrum. After employing many trials performed in filter design with various built-in parameters, a second-order low-pass Butterworth filter with 0.5 kHz cut-off frequency was applied to the displacement signals. When the maximum frequency and the dominant frequencies are considered in collecting displacement signals, it can be said that the sampling rate of 200 kHz in the data acquisition system is adequate for capturing the displacement response during the impact events.

Another signal set required filtering process was the strain data collected for steel reinforcing bars strains measurements during the impacts. Similar to displacement signals, the collected data was significantly noisy, as depicted in Figure 4.6a and Figure 4.6b. By employing the same trials as in the displacement data filtering process, a second-order low-pass Butterworth filter with 10 kHz cut-off frequency was applied to measured signals. As it can be seen from Figure 4.6c, the cut-off frequency was significantly far from the dominant frequency region, as well as the frequency where the amplitude reached the peak. It should be noted here that the sampling frequency of strain data was collected by a faster acquisition system with a 2000 kHz that is accepted sufficient enough according to the developed power spectrum.

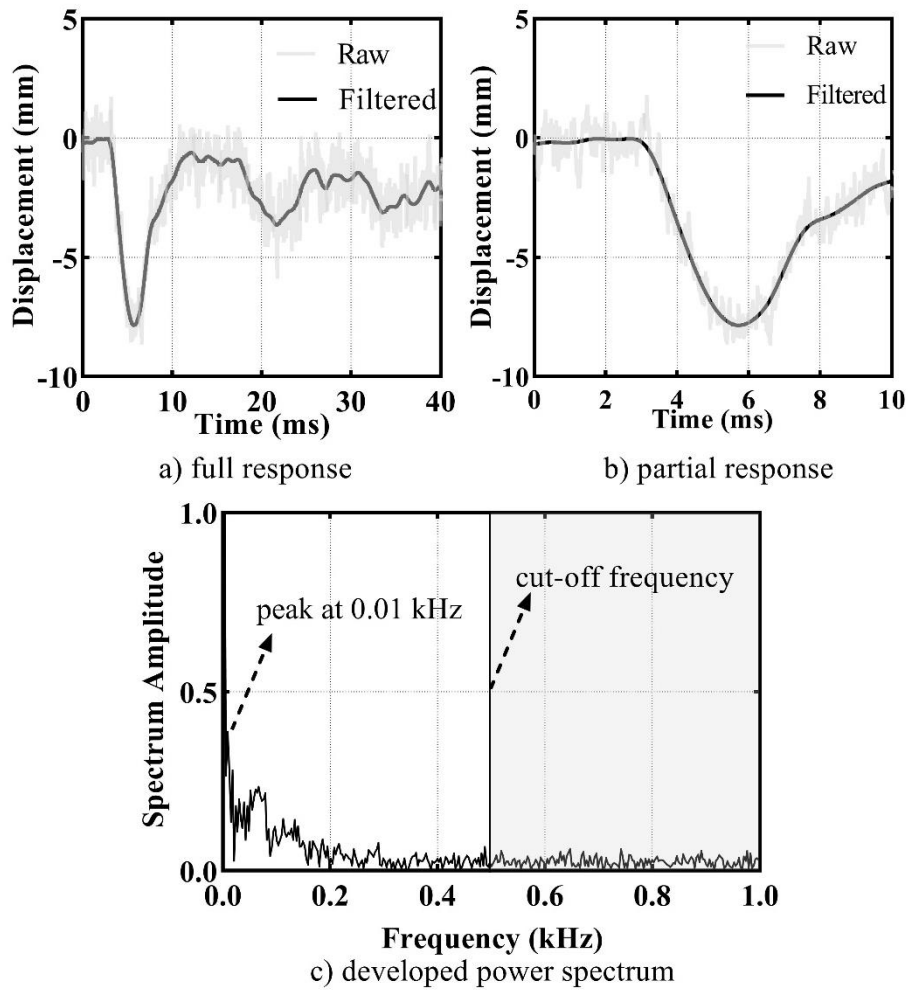


Figure 4.5. Measured midpoint displacements and developed power spectrum for the first impact test of S4T2

The signals collected from accelerometers and load cells were not filtered since they were not as noisy as laser displacement sensors and strain gauges, and they were used directly for evaluation of the response-time histories of slab specimens in impact tests. Power spectrums constructed for measured reactions and measured accelerations are shown in Figure 4.7a and Figure 4.8a, respectively. As depicted in Figure 4.7b and Figure 4.8b, the maximum amplitudes of the collected data reached the peaks at very low frequencies. Therefore, it can be said that the 200 kHz of the sampling rate of data acquisition system was capable of gathering accurate and reliable data sets.

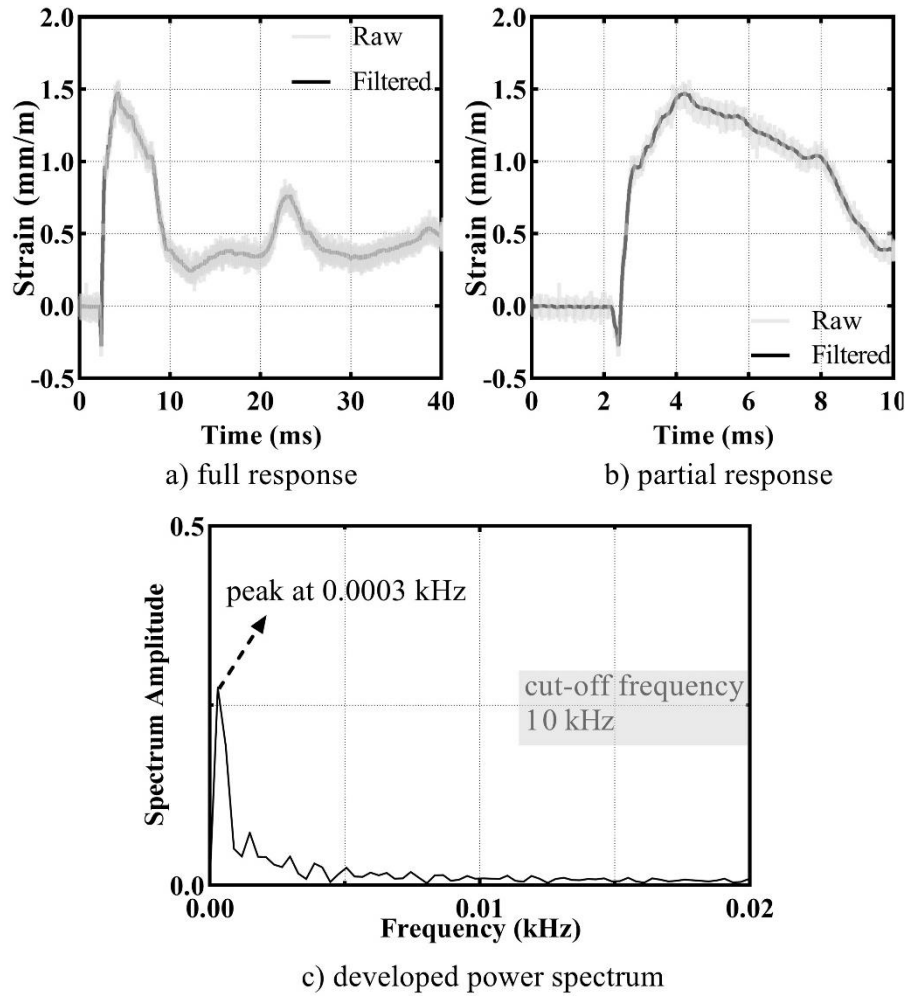


Figure 4.6. Measured strains and developed power spectrum for strain gauge 1 in the first impact test of S1T0 specimen

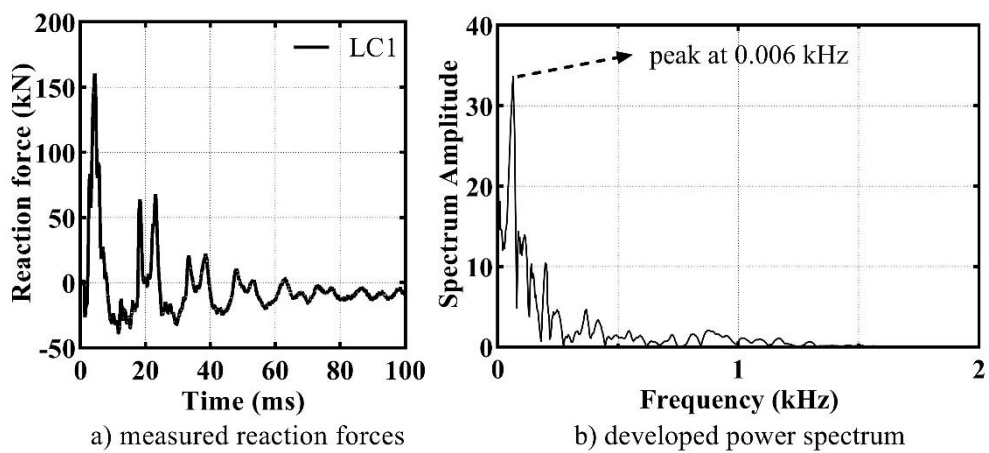


Figure 4.7. Measured reactions and developed spectrum for load cell 1 in the first impact test of S1T0 specimen

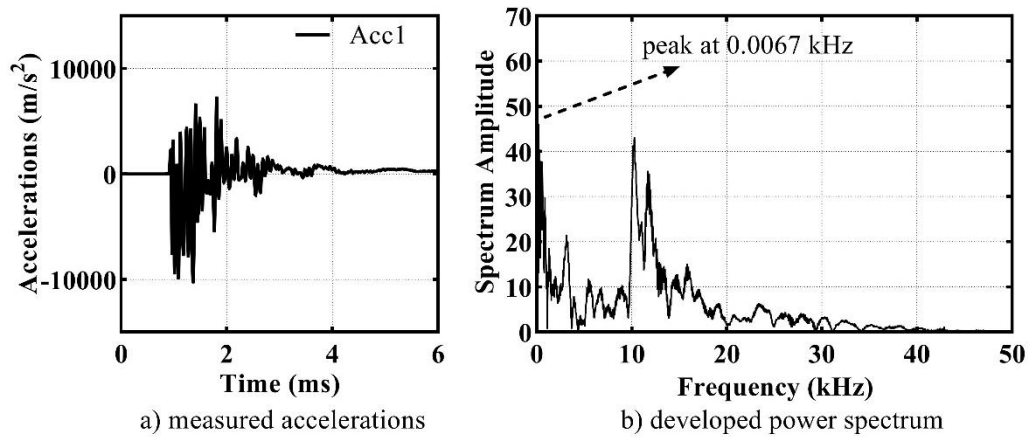


Figure 4.8. Measured accelerations and developed spectrum for accelerometer 1 in the first impact test of S1T0 specimen

### 4.3. Displacements

In the analysis of an RC member or structure, the displacement response is very important with respect to its design purposes. In particular to high-rate loading events, the displacement history of a member is very helpful to understand the deformation capabilities in designing stages. Moreover, the displacement response is one of the direct measurements to make comparisons between different types of analyses or methods (i.e. experimental data vs analytical data vs numerical data). Therefore, to serve functional outcomes, the displacement-time histories acquired from the impact tests are presented in this section.

#### 4.3.1. Midpoint Displacements

As explained in the previous chapter, the midpoint displacement data was collected by contactless laser sensors from the bottom surface of specimens. Beginning from the first impacts, cracks on the bottom surface of specimens were observed as presented previously. Subsequent impacts caused widening in inherited cracks or concrete scabbing at the bottom surfaces. Therefore, it is observed that there were some barriers or blockage between laser light and sensor, causing misinterpretations or complete faults in signaling information due to crack development at the measurement point or scabbed concrete parts from surface. These faults were depicted in dotted lines as measuring faults in the measured displacement-time histories.

As previously explained, with the aim of deciding the striker velocity, the unstrengthened slabs were subjected to the same steel striker impacts with different contact velocities. The measured midpoint displacement-time histories of these identical slabs tested under different impact loads are presented in Figure 4.9. In these tests, both specimens were tested under two repeated impact loads. To make a comparison between displacement profiles, the displacement-time histories of the specimens were shown for the first and second impacts in Figure 4.9a and Figure 4.9b, respectively.

As it is shown in Figure 4.9a, the peak displacement of specimen S1T0 was reaching 11.2 mm, whereas the peak displacement of specimen S2T0 was measured as approximately one and a half times higher than specimen S1T0. In the first tests, both peaks were recorded approximately at the same time at 4 ms. It should be reminded here that the striker velocities were designated as 25.9 m/s and 30.2 m/s in the first tests for S1T0 and S2T0 specimens, respectively. Even though the peaks are different in the impacts, the oscillation regimes are quite similar, up to 40 milliseconds. Beyond that time, unreasonable data were recorded by contactless laser sensor for S1T0 specimen up to 100 ms, shown as dotted line in graphs. When imparted kinetic energies to the specimens are considered, the energy difference between the two tests can be expected to dissipate in the specimen body, causing more damage. As expected, the measured residual displacement of S2T0 was slightly lower than twice the residual displacement of S1T0 specimen as a result of a higher damage level.

Due to the difference in damage levels between these specimens after the first impacts, the gap between measured peak displacements in the second impact tests increased (Figure 4.9b). It should be noted here due to faults in measuring signal caused by scabbed concrete, the measured displacements are not trustworthy beyond 15 ms which was double-checked with the help of the footages recorded by the high-speed camera.

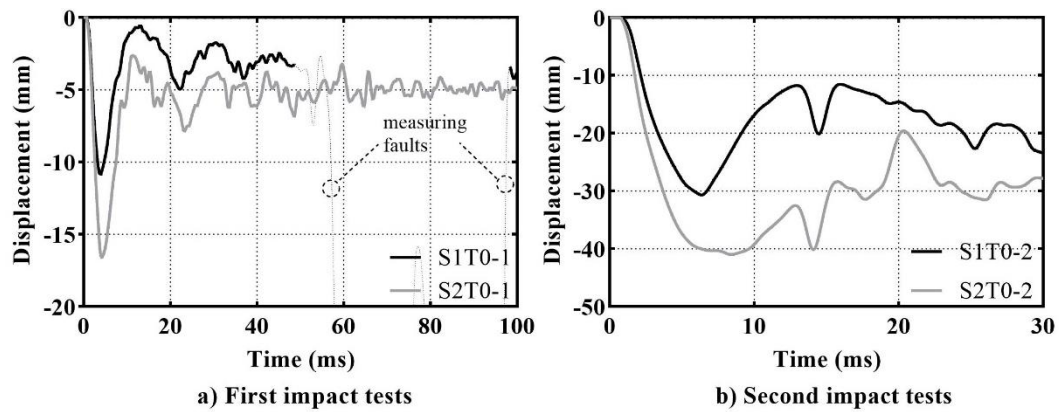


Figure 4.9. Midpoint displacement-time histories of S1T0 and S2T0

Measured displacement-time histories related to the strengthened S3T1 and S4T2 specimens are displayed in Figure 4.10a and Figure 4.10b for the first and second impacts, respectively. It should be reminded here that the strengthened specimens were subjected to the same impact loads until total perforation occurred. At the first impacts, the measured displacement responses of the specimens were approximately the same with a slight difference in the first negative peaks, even though they had different carbon textile reinforcement ratios. It can be interpreted as the textile reinforcement ratio did not have a leading role in the first impact loading. However, as it can be seen from Figure 4.10b, the effect of carbon textile reinforcement ratio became prominent in the following impacts, limiting the peak displacements as 27.0 mm for S3T1 specimen and 18.6 mm for S4T2 specimen. Moreover, an increase in the carbon textile reinforcement ratio was very effective on the residual displacement, decreasing from 10.1 mm to 4.0 mm in S3T1 and S4T2 specimens, respectively. As it is shown on previous measured displacement-time histories, some discrepancies were observed in the data which are shown as dotted lines in Figure 4.10.

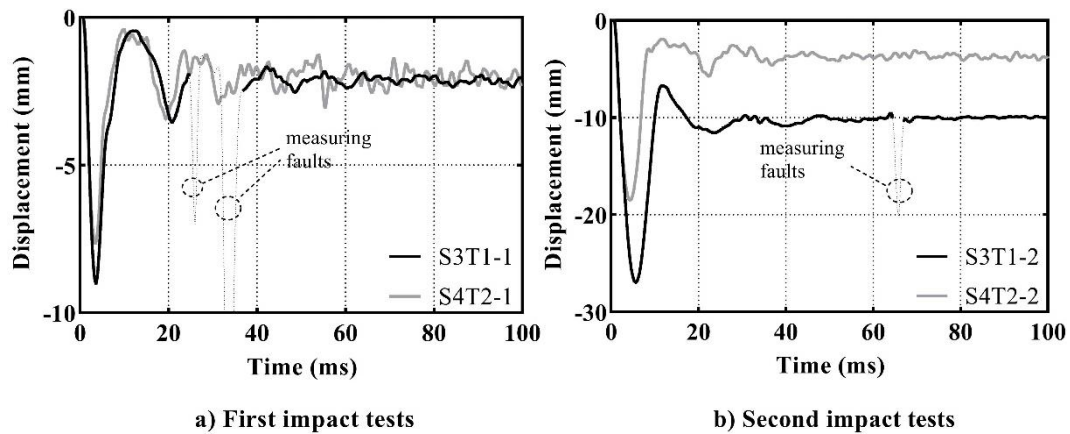


Figure 4.10. Midpoint displacement-time histories of S3T1 and S4T2

In the following impacts for S3T1 specimen, the laser sensors could not succeed to collect meaningful signals due to the formed cracks at the midpoint. It should be reminded here this specimen was perforated at the fourth impact test. However, in the subsequent impact tests of S4T2, the measured displacement-time histories are presentable. It should be noted here that the specimen S4T2 could withstand five subsequent impacts and the perforation occurred at the sixth impact. The displacement-time histories belonging to the third and fifth impacts of S4T2 specimen were depicted in Figure 4.11. As it can be seen from Figure 4.11a, the carbon textile reinforcements were still effective for limiting the displacements at third impact. The peak displacement was approximately the same as the previous tests, whereas the residual displacement increased to 6 mm. For brevity, the fourth impact test of S4T2 specimen is not presented herein. Instead, the fifth impact was preferred to be depicted in Figure 4.10b where the behavior differentiated. Despite the peak displacement at the midpoint decreased in the fifth impact test, the member lost the ability to recover as in former tests, and the highest residual displacement was observed with the excessive bulging. Yet, the specimen kept its integrity and survived after the fifth impact. As expected, S4T2 was the strongest specimen among others, owing to embody the highest carbon textile reinforcement ratio.

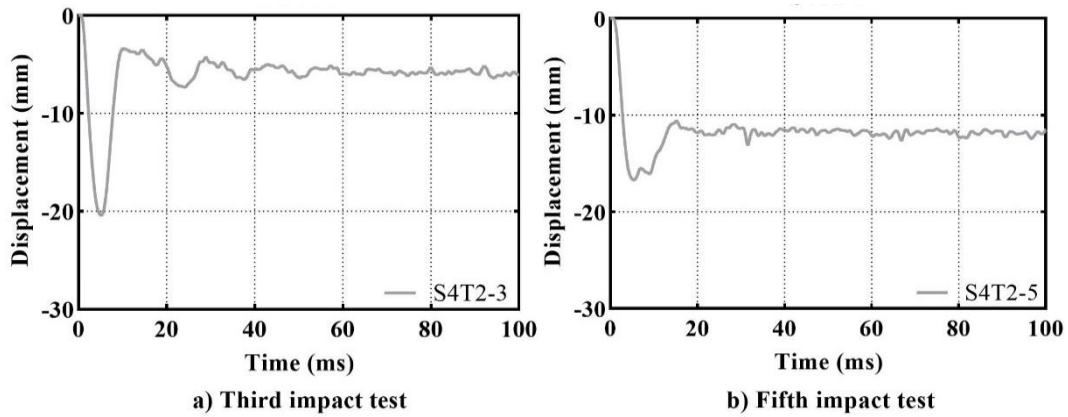


Figure 4.11. Midpoint displacement-time histories of S4T2

With the intent to make a comparison between the displacement responses of unstrengthened and strengthened specimens under the identical impact loading, the measured displacement-time histories of S1T0, S3T1, and S4T2 specimens were presented in Figure 4.12a and Figure 4.12b for the first and second impact tests, respectively. As it can be clearly seen from Figure 4.12a, the specimens strengthened with carbon textile layers exhibited lower maximum and residual displacements than the unstrengthened one. However, it can be said that the decrease in the maximum and residual displacements is a result of higher stiffness due to the increase in thickness for additional strengthening layers. On the other hand, it's seen that the contribution of carbon textile reinforcements became more considerable for the following impacts (Figure 4.12b). In the second impacts, the peak deformation of S3T1 specimen was relatively lower than the S1T0 specimen, whereas the textile reinforcements showed better performance for limiting the residual deformation. Additionally, increase in the textile reinforcement ratio played a vital role to reduce the peak displacement and residual deformation when the strengthened specimens are compared to each other.

The peak and residual displacements are tabulated and presented in Table 4.1. It should be noted that the presented displacements in the tests belong to each impact event and the total displacements are accumulated from previous tests.

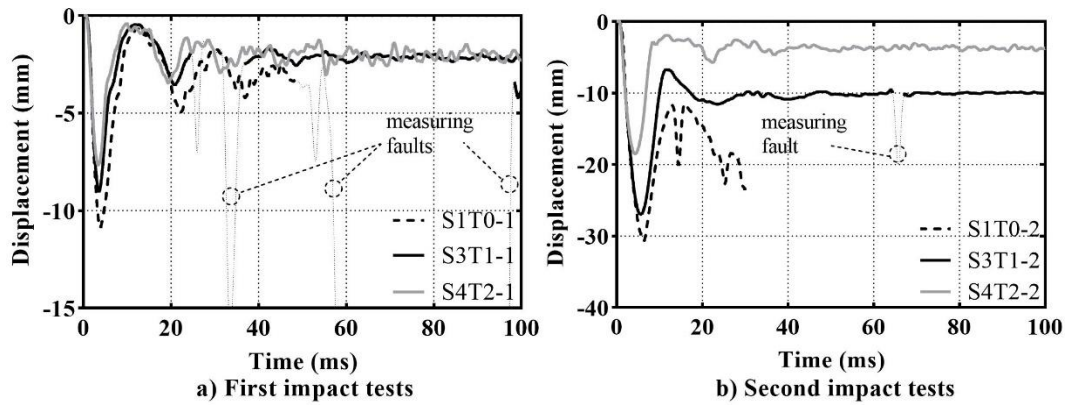


Figure 4.12. Midpoint displacement-time histories of S1T0, S3T1 and S4T2

Table 4.1. Measured displacements at the midpoint

Slab - Impact #	Striker velocity (m/s)	Disp. in test		Disp. in total	
		Peak (mm)	Residual (mm)	Peak (mm)	Residual (mm)
S1T0-1	25.9	8.9	1.5	8.9	1.5
S1T0-2	25.3	27.9	N/A	36.8	N/A
S2T0-1	30.2	16.0	5.0	16.0	5.0
S2T0-2	29.7	40.7	N/A	56.7	N/A
S3T1-1	26.0	5.0	0.9	5.0	0.9
S3T1-2	26.0	25.9	9.2	30.9	10.1
S3T1-3	26.2	N/A	N/A	N/A	N/A
S3T1-4	25.4	N/A	N/A	N/A	N/A
S4T2-1	26.0	5.7	0.9	5.7	0.9
S4T2-2	25.9	16.5	2.3	22.2	3.2
S4T2-3	25.9	20.4	6.2	42.6	9.4
S4T2-4	25.4	21.3	8.4	63.9	17.8
S4T2-5	26.0	17.2	12.5	81.1	30.3
S4T2-6	25.9	N/A	N/A	N/A	N/A

### 4.3.2. Edge Displacements

To measure the displacements at the intersection point of the middle axis of specimen and the axis of supports as depicted in the previous chapter, another laser sensor was placed under the specimens. The acquired signals for all impact tests were examined and filtered with the same methods as employed for the midpoint displacements. However, as depicted in Figure 4.13, the signals were extremely noisy

even after filtration and it cannot be used for meaningful discussion due to the constant oscillations throughout the recorded full data.

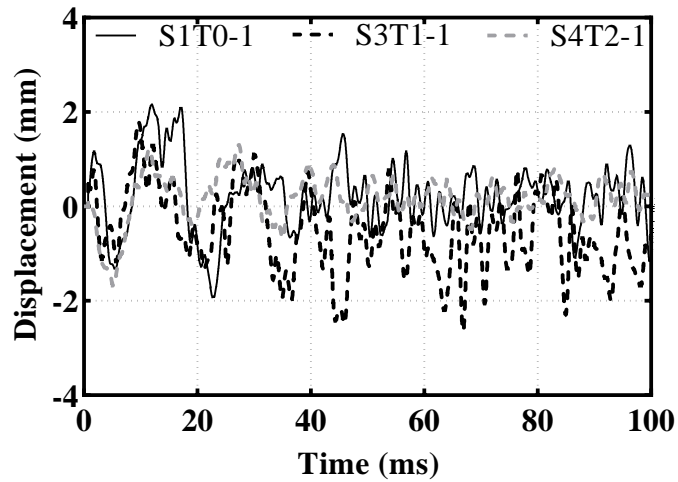


Figure 4.13. Edge displacements for S1T0-1, S3T1-1 and S4T2-1

#### 4.4. Reactions

As previously explained, the reaction forces were measured by self-developed load cells located at the four corner supports for each specimen. Measured reactions for each cell showed similar response histories. The typical measured reaction-time histories from each load cell are presented in Figure 4.14. To obtain total measured reaction forces, reactions from the load cells were summed up. The accumulated reaction forces from the test are presented as total reaction-time histories in this section.

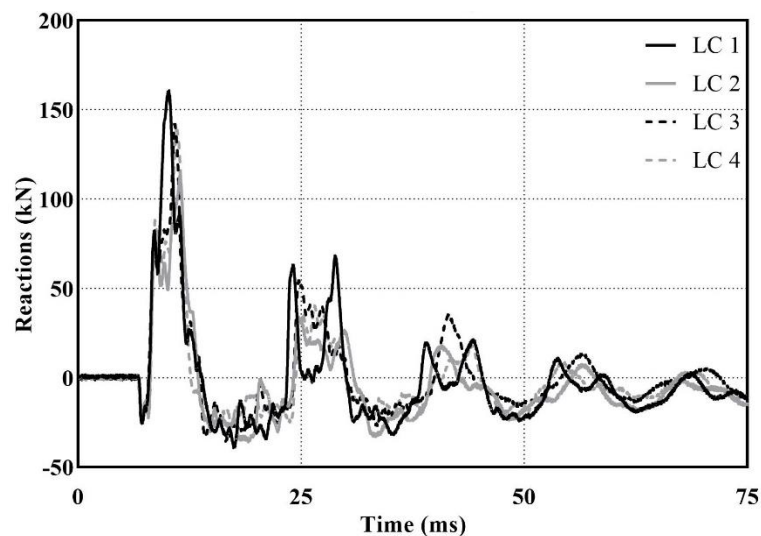


Figure 4.14. The reactions measured from each load cell for S1T0-1 test

The measured total reaction-time histories obtained from the tests are depicted for the first and second impacts in Figure 4.15a and Figure 4.15b, respectively. As it can be seen from Figure 4.15a, the unstrengthened specimens had very similar reaction-time histories in spite of the different striker velocities in the tests. When the conservation of energy is considered, the dissipated energy in S2T0 specimen was higher than S1T0 specimen, causing higher damage levels such as wider cracks, higher penetration depth, and scabbing of concrete.

In the second impact tests of unstrengthened specimens, the numbers of cycles in the measured reaction-time histories were lower than previous tests for both specimens (see Figure 4.15b). The measured peak reactions were similar in the first and second impact tests for S1T0 specimen, whereas, for specimen S2T0, the measured peaks were lower in the second impact test and the reaction forces decay more quickly. It can be said that with the increase in damage levels, the transmission of applied loads to the supports is diminishing. This can cause more localization effects in the sequential impacts.

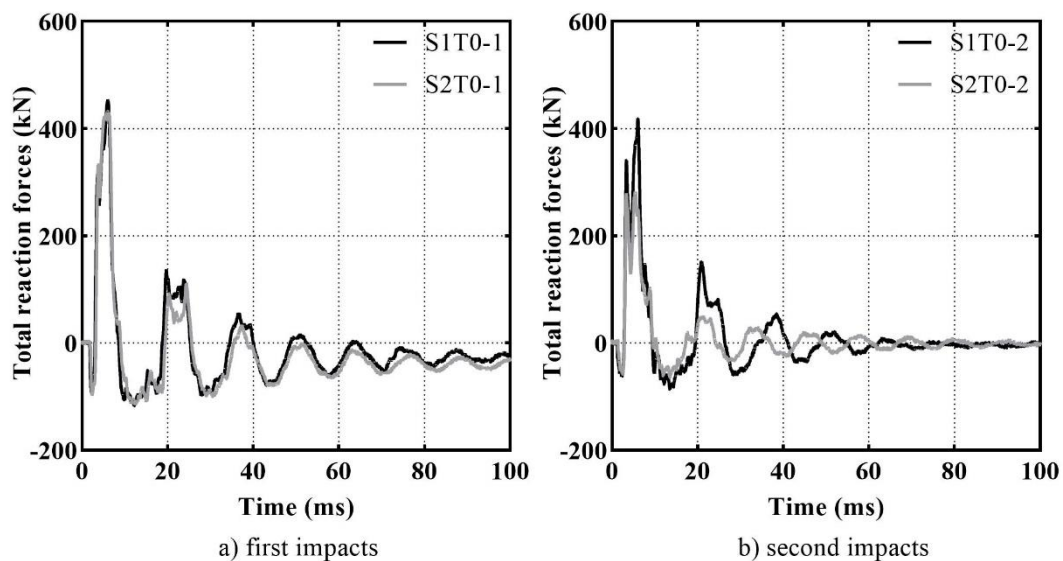


Figure 4.15. The measured total reactions for S1T0 and S2T0 specimens

The measured total reaction-time histories of strengthened specimens are presented in Figure 4.16 and Figure 4.17. In the first impact tests of S3T1 and S4T2 specimens, the peak reaction forces are slightly higher than the S1T0 specimen which were subjected to the same striker with the same contact velocities (Figure 4.16a). However, the number of cycles in the reaction-time histories of strengthened specimens

were higher than the unstrengthened specimen. An increase in the number of cycles can be attributed to two causes: the increase in specimen stiffness due to an increase in thickness, and more effective load distribution owing to carbon textile reinforcements even after damage. The latter, in fact, is observable in the following impacts of strengthened specimens. As depicted in Figure 4.16b and Figure 4.17a, the total reaction force-time histories were found to be similar for the second and third impact tests of strengthened specimens, accounting for punching cones already developed in the first impacts. It can be said that the carbon textile reinforcements are functional for transmitting the applied loads and providing the member integrity in the second and third impact tests. It should be noted here that the S3T1 specimen which had the least carbon-textile reinforcement ratio was totally perforated at the fourth impact. The reaction force-time history of S4T2 showed similarities to previous impact tests. However, with the excessive damaging and bulging of the punching cone, the strengthening efficiency was fading away and the majority of impact load could not be transferred at the fifth impact test of S4T2 specimen (Figure 4.17b). According to the reaction force responses and observations from impact tests, it can be deduced that the carbon textile reinforcements can be effective for strengthening or retrofitting purposes in accordance with the load transmitting capabilities in the range of certain damage levels.

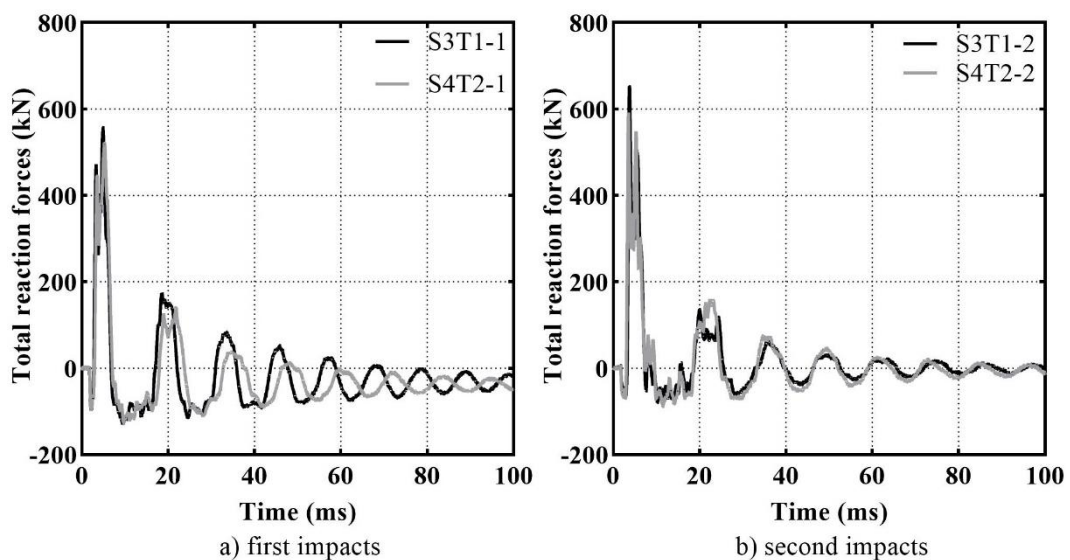


Figure 4.16. The measured total reactions for S3T1 and S4T2 specimens

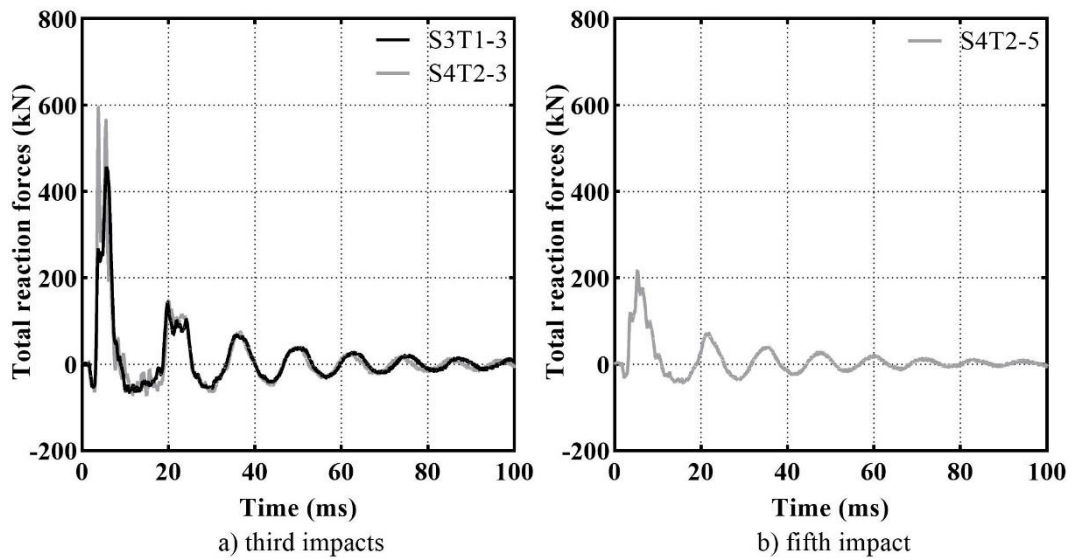


Figure 4.17. The measured total reactions for S3T1 and S4T2 specimens

The measured peaks in the total reaction-time histories are tabulated as compression and tension and presented in Table 4.2.

Table 4.2. Measured peak support reactions

Slab - Impact #	Striker velocity (m/s)	Peak reactions (kN)	
		Compression	Tension
S1T0-1	25.9	117.8	450.1
S1T0-2	25.3	86.7	417.5
S2T0-1	30.2	115.0	431.5
S2T0-2	29.7	64.9	280.2
S3T1-1	26.0	128.5	520.7
S3T1-2	26.0	79.9	650.6
S3T1-3	26.2	64.9	456.6
S3T1-4	25.4	46.2	182.3
S4T2-1	26.0	131.2	555.5
S4T2-2	25.9	87.9	592.2
S4T2-3	25.9	73.0	892.7
S4T2-4	25.4	69.2	444.7
S4T2-5	26.0	43.5	215.2
S4T2-6	25.9	34.8	46.7

## 4.5. Accelerations

To obtain specimens' accelerations in the course of impact tests, four accelerometers with  $\pm 5000g$  were placed on the surface of specimens at different points which are illustrated in the previous chapter. With the intent to capture punching cone accelerations for the impacts, one of the accelerometers was mounted on a point very close to the midpoint. Unfortunately, the captured data from the tests exceeded the capacity of the accelerometer. The acceleration-time history captured by Acc4 from the midpoint for the first impact tests of unstrengthened and strengthened specimens were depicted as a representative for the accelerations recorded at the midpoint. (Figure 4.18).

As explained in the previous chapter, three of the accelerometers were placed on the top surface of specimens. Two of these accelerometers were placed on the perimeter of a circle with a 400 mm radius: one on the diagonal axis (Acc1); one on the middle axis (Acc2). The last accelerometer was placed at the middle of the point between supports on the top surface (Acc3). The acceleration-time histories of the accelerometer 1 (Acc1) and accelerometer 2 (Acc2) are expected to be the same or quite similar when the distances of the accelerometers to the origin of stress wave propagation (impact point) are considered. However, this theoretical assumption is not supported by the data recorded by the accelerometers in equidistance to the origin of wave propagation. As it can be seen from Figure 4.19a, measured accelerations were dissimilar. On the other hand, these dissimilarities can be caused by supporting conditions at the supports. As presented in Figure 4.20, the reaction force-time histories measured from load cells for each supports are different from each other which can be interpreted as asymmetric oscillations in the parts of the specimen body. Additionally, the accelerations measured by the accelerometer 3 (Acc3) which was the utmost accelerometer to the impact point are relatively lower than the others (Figure 4.19b). This was observed typically for each impact test.

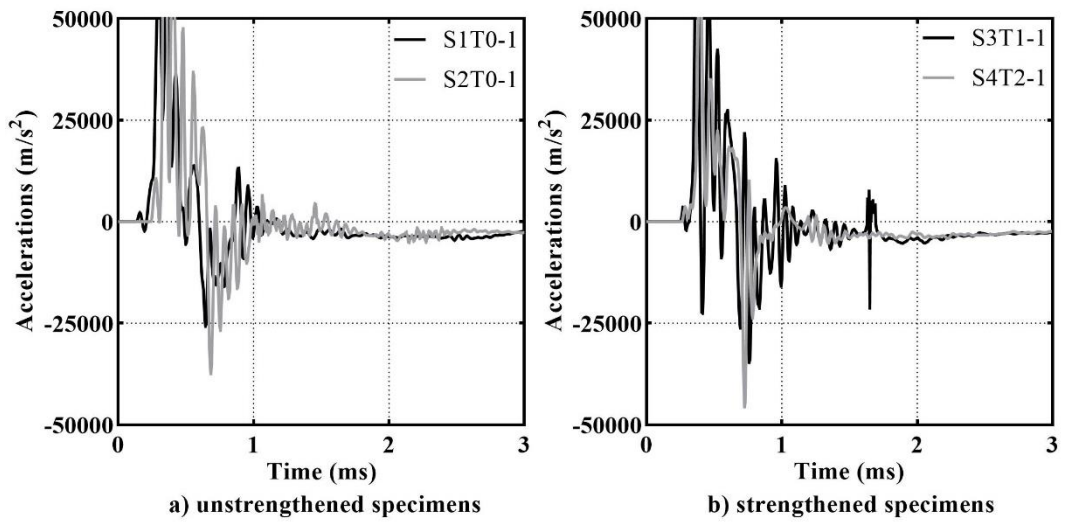


Figure 4.18. The measured accelerations from the midpoint of specimens (Acc4)

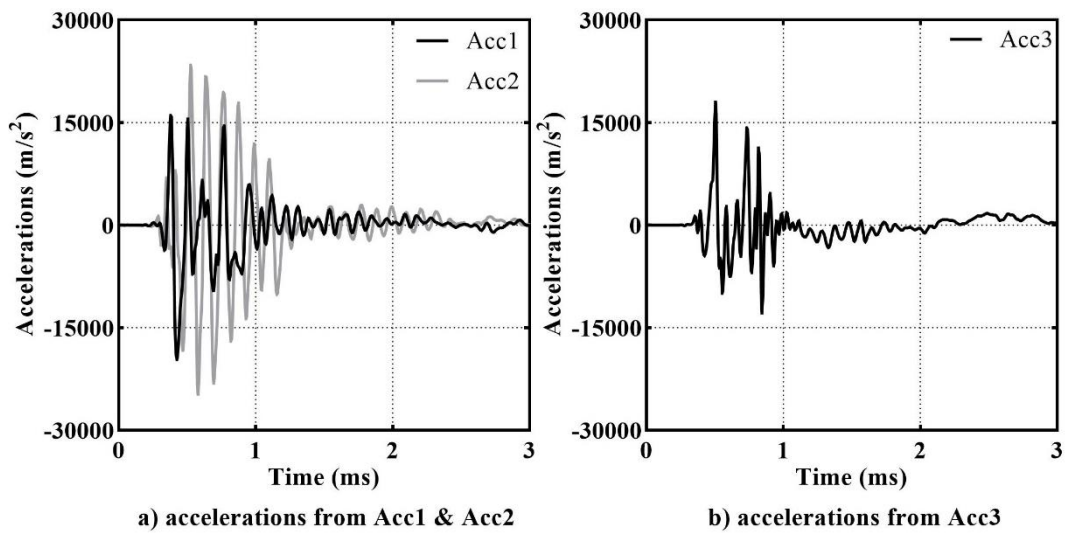


Figure 4.19. The measured accelerations for S4T2-3

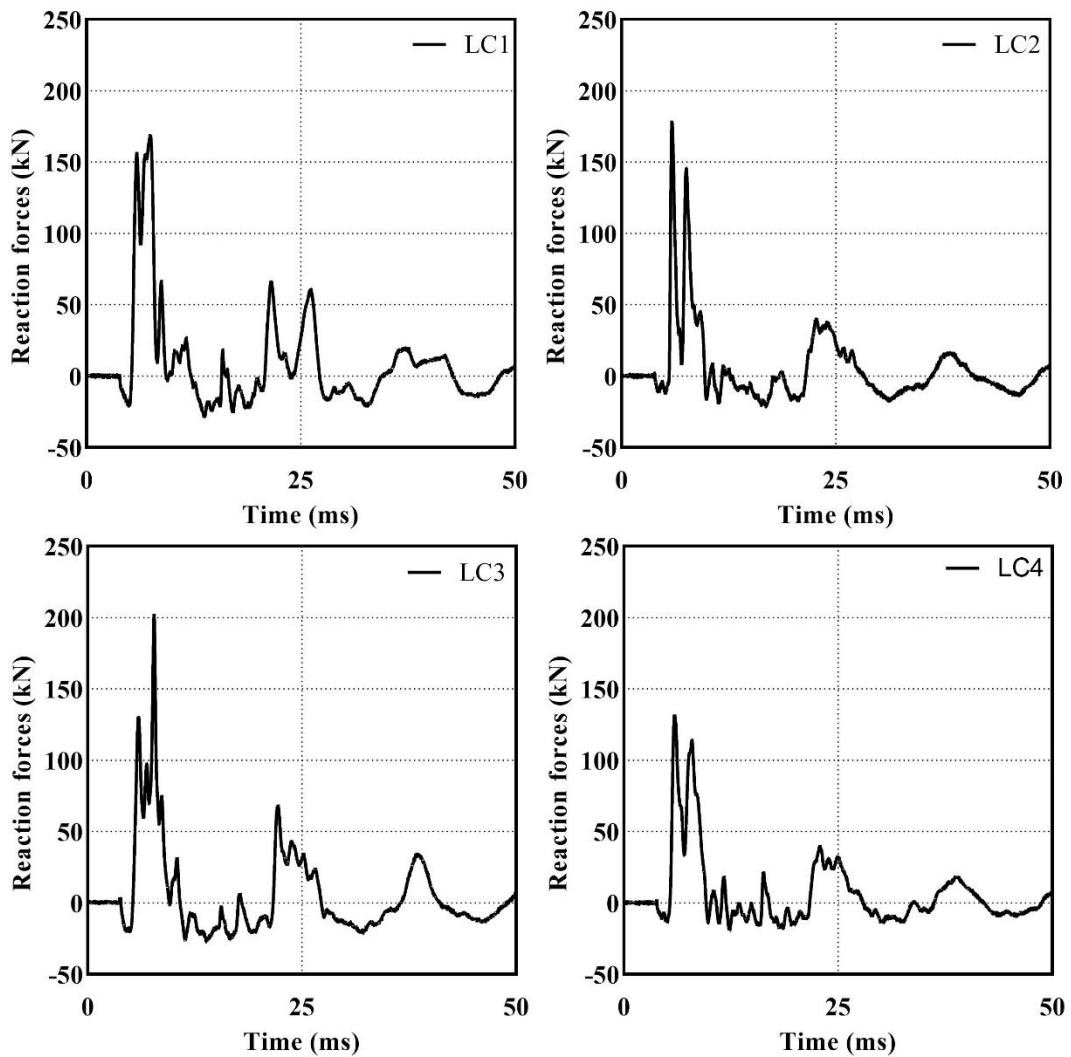


Figure 4.20. The measured reaction forces at each load cells for S4T2-3

#### 4.6. Steel Reinforcement Strains

As explained in the previous chapter, four strain gauges were attached to the steel reinforcing bars equidistantly to the midpoint of specimens to measure the acceleration-time histories during the impacts. It should be reminded here that the attached strain gauges were situated to reside in the assumed punching cone region. After the tests, all strain data were examined and it was seen that only a limited number of strain gauges were able to record fair data to present. Therefore, in this section, the strain values measured by the selected strain gauges are presented. Before presenting the strain-time histories, it should be reminded here that the steel reinforcing bars were ordered from a local steel company, providing the material characteristics such as yield strength and modulus of elasticity, 500 MPa, and 200000 MPa, respectively, as

mentioned in the previous chapter. Therefore, it is assumed that the steel reinforcing bars yield at 2.5 mm/m strain. Lastly, keep in mind that all measured strain-time histories in this section are presented for the particular impact events, not accumulated from previous events.

The measured strain values in the impact tests of unstrengthened specimens, S1T0 and S2T0, are shown in Figure 4.21 for strain gauge 2 and strain gauge 3. As it can be clearly seen, the peak strain values in the first impacts did not reach the yield strains. It should be reminded here S2T0 specimen was subjected to higher impact loads with higher striker velocities. Despite it was tested under higher impact loads, the measured residual strain was surprisingly lower than the residual strain measured from the S1T0 impact test.

The only presentable measured strain-time history for the second impact tests of unstrengthened specimens was obtained from strain gauge 2 employed for S1T0 specimen. As it is obviously seen from Figure 4.21b, the steel reinforcing bar exceeded the yielding point, peaked at 8 mm/m, and resulted in permanent deformation with 6.8 mm/m strain.

The only reasonable strain data in the impact tests of the strengthened specimen was only provided by the strain gauge 3 used in S3T1 tests. As it can be seen from

Figure 4.22, the strain values are depicted for three subsequent impacts. It should be reminded here that the S3T1 specimen was perforated at the fourth impact and the strain data belonging to the final test was unreasonable. The peak and residual strains at the first impact were lower than the strains obtained from the first impact test of S1T0, as expected. For the sake of a 2 cm additional strengthening layer, the displacements in the tests of S3T1 specimen were limited due to the reasons previously discussed in this chapter. Therefore, in agreement with the displacement profiles of S3T1 in the tests, strain gauge 3 did not measure yielding strains for three consecutive impact tests. Additionally, the residual strains were very limited until the fourth impact where the perforation failure occurred in the specimen.

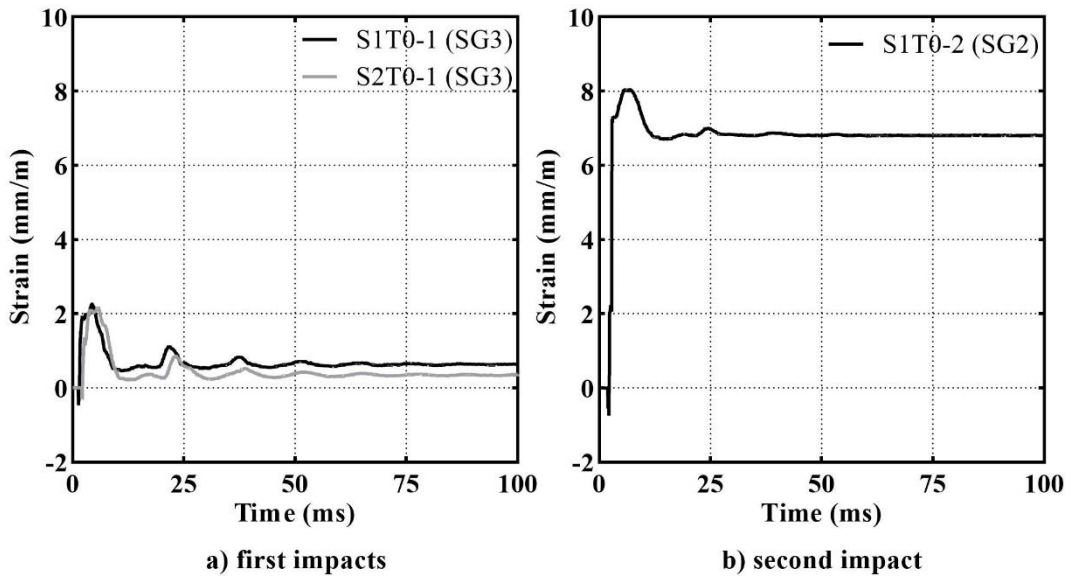


Figure 4.21. The strain time histories of S1T0 and S2T0 specimens

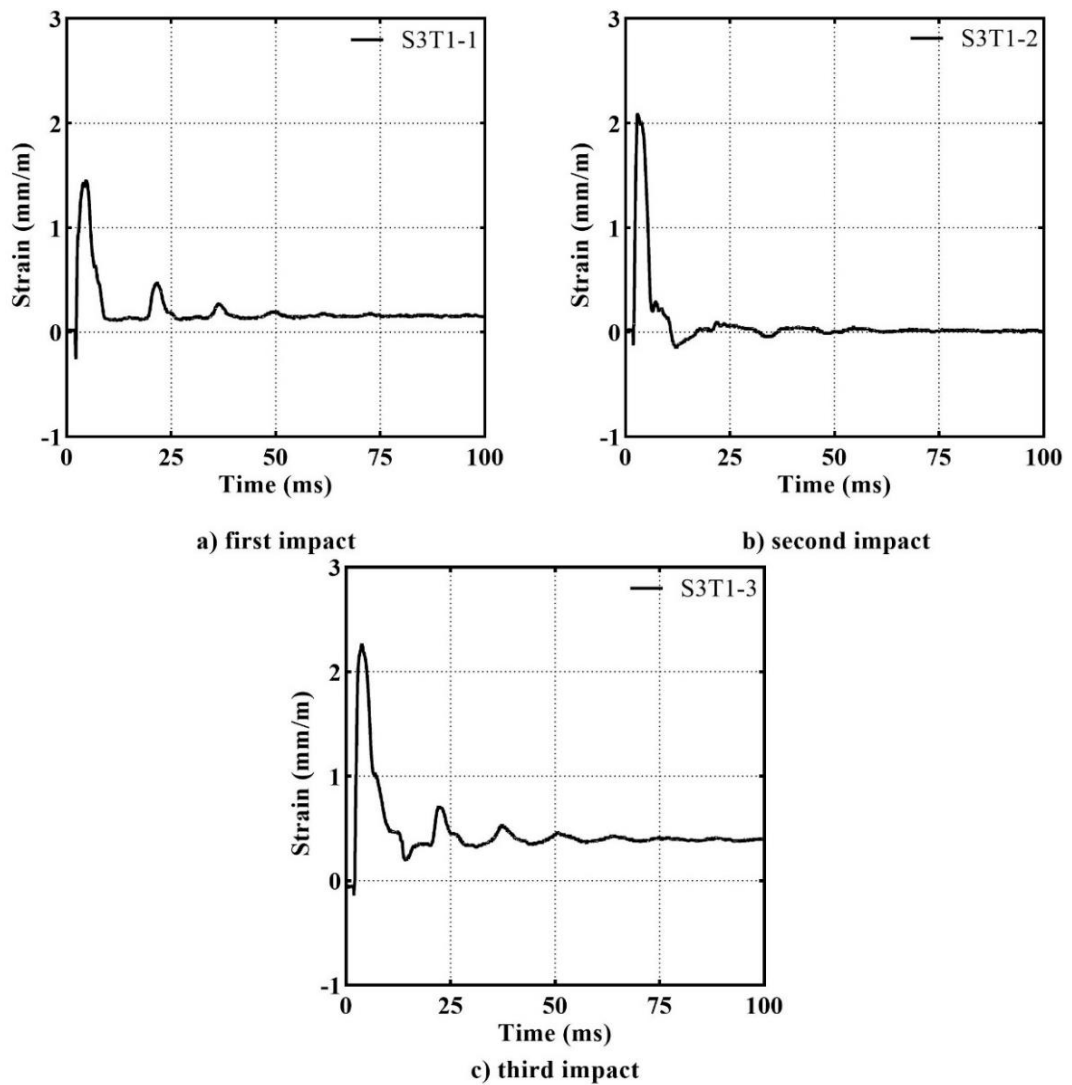


Figure 4.22. The strain time histories of S3T1 specimen measured from SG3

## CHAPTER 5

### FINITE ELEMENT MODELING

The capability of conducting experiments, particularly large-scale laboratory tests, on the behavior of members under high-rate loadings is a great asset. However, performing a well-instrumented experimental program in this area is not an easy task. In addition to the complexity of testing, it can be very expensive, time-consuming, and demanding for the workforce. In contrary to complex test methods, some challenges such as scaling problems from experiment to reality can be confronted in more basic test methods. These drawbacks in both complicated and simplified experimental investigations can be overcome by using numerical approaches. Broadly, numerical methods set designers and engineers free by eliminating a great majority of limitations of experimental investigations. However, the freedom arises with its price such as computational power and time demands, and, most importantly, data requirements ranging from simple to specific. Especially, when the impact dynamics and uncertainties in material behavior under high-strain conditions are considered, computational tools can evolve from a savior angel to a demon. Therefore, reliable data from experiments play a vital role in validating numerical techniques and take part as a guide for further steps.

As explained previously, one of the targets of this thesis is to introduce experimental data sets for the RC slab specimens strengthened with carbon textile reinforcements under impact loads for the numerical investigations. As a next step of conducting impact tests, numerical investigations were performed by using the LS-DYNA finite element (FE) software to present a numerical model validated by collected data sets. In this section, created FE models are explained first, and then, comparisons between analyses and test results are presented in terms of displacement responses, reaction force responses, and observable damage patterns.

#### 5.1. Modeling of Impact Tests

LS-DYNA is one of the powerful finite element codes, and its applications are widely used by engineers and researchers to model and analyze several automobile,

aerospace, civil, and mechanical engineering problems and complexities. It was created to simulate the impact events, and it has been developed and upgraded until today. When the software's abilities and user-controlled parameter families are considered, LS-DYNA is one of the most distinguished software used for non-linear dynamic analysis such as impact and blast events.

In the numerical investigations of this study, the tested slab specimens were modeled in LS-DYNA. One quadrant of the specimens and test setup were modeled considering the two-axis symmetry of the specimens, support, and loading conditions. To model slab specimens, eight-node hexahedral solid elements were used for both steel-reinforced and textile-reinforced concrete sections. With the intent of obtaining the most effective mesh, several FE analyses were performed with different mesh sizes for the sections used in the models. As a result of these trials, two models with different mesh sizes were employed for the comparison and mesh sensitivity analysis. These models are presented and explained in this section.

Firstly, to model steel and textile reinforcements, one-dimensional beam elements were used in created FE models. Modeling of reinforcements embedded in concrete matrix can be implemented by using two methods; shared nodes and constraint method (Schwer, 2014). To provide independence to the element size of the reinforcements, steel, and textile reinforcement bars were embedded in the concrete matrices by using Constrained Lagrange in Solid (CLIS) method. This method is the most common in the literature due to its element size independence.

As mentioned earlier, numerical investigation is a versatile tool to acquire information about behavior of structures and members for particular designs and purposes. However, this type of analysis comes with a bill that needs to be paid off such as computational power and time. With the intent to reduce these costs, one quadrant of the testing conditions was only modeled owing to symmetrical boundary conditions of the testing facility. Additionally, as explained earlier, each support at the testing facility contains a high-strength steel bar, passing through the specimen and providing constraints by two steel plates at the bottom and top faces of specimen. Instead of modeling the hallow section in concrete body and the high-strength steel bar at the support, support conditions were mimicked by means of two rigid plates with translational constraints in every direction. It should be noted here that anti-symmetric modes formed during impact events are ignored by modeling one quadrant model. However, when the behavior and damage levels of tested specimens are considered,

these modes are negligible. The contribution of these modes should be checked when the impact behavior is in linear ranges. Due to non-linear behavior, only symmetric modes are considered to be activated, and therefore the quarter model is assumed to be sufficient.

Similar to the slab specimens, the striker was also modeled as a quadrant of the actual striker employed in the tests. The striker was created by using eight-node hexahedral solid elements as in concrete and rigid parts of the model. The overall view of a model can be seen in Figure 5.1.

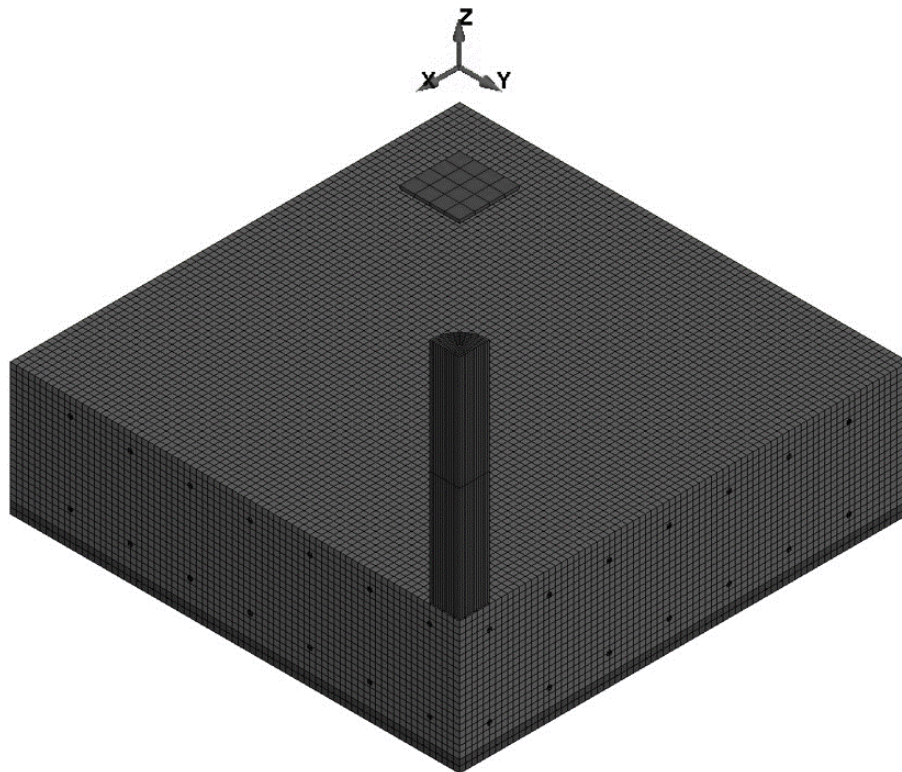


Figure 5.1. A quadrant of a slab specimen modeled in LS-DYNA

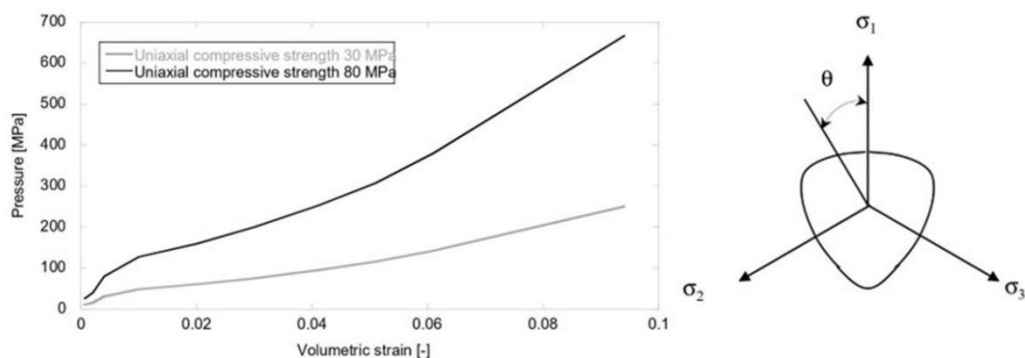
### 5.1.1. Material Models

LS-DYNA comprises a material library with a generous variety of material models. In the literature, material models with so-called “simple-input” requirements are generally preferred by many researchers and engineers on account of available experimental information for material characteristics. In this regard, concrete models such as Karagozian & Case Concrete Model (MAT\_72R3), Winfrith Concrete Model (MAT\_84/85), and Continuous Surface Cap Model (MAT\_159) are widely used in the

literature for impact and blast phenomena on RC structures. These concrete models have the ability to generate default material parameters by using basic material properties such as unconfined concrete strength  $f'_c$ , Poisson's ratio  $\nu$ , unit weight,  $\rho$ , and aggregate size. Among these models, Winfrith Concrete Model is the only one that can generate and present the crack mapping depending on its fracture energy.

In the light of literature, all three concrete models were employed for impact tests to make a comparison between material models. However, the performed simulations by using MAT\_72R3 and MAT\_159 exhibited unreasonable behavior and resulted in instability problems. Therefore, Winfrith Concrete Model was used for the concrete sections.

Winfrith Concrete Model was originally developed to simulate impact tests on RC structures performed by Nuclear Electric in the UK (Broadhouse, 1995; Broadhouse & Attwood, 1993). In this model, the stress state in concrete is separated as a hydrostatic state and a deviatoric state. The hydrostatic stress state is defined as a relationship between pressure and volumetric change of concrete which is defined as a dimensionless compaction curve in the model (LS-DYNA User's Manual, 2014). This defined curve can be also defined by user. The deviatoric stresses are determined by using the Ottosen yield surface (Ottosen, 1977). On the deviatoric plane, the higher hydrostatic stresses cause a smoother (circular-like) failure surface, including the strain rate effects based on CEB formulations (CEB, 1988). The compaction curve and the shape of the Ottosen yield surface can be seen in Figure 5.2.



a) Compaction curves given in MAT\_84

b) Ottosen yield surface

Figure 5.2. The compaction curves and the shape of Ottosen yield surface employed in Winfrith Concrete Model (source: Alonso (2013))

In the literature, two types of material models, Plastic-Kinematic Model (MAT\_03) and Piecewise Linear Plasticity Model (MAT\_024) are widely used for modeling steel reinforcing bars. In this study, Plastic-Kinematic Model (MAT\_03) was employed for steel and textile reinforcements. This model is bilinear, accounting for the strain rate effects (see Figure 5.3). Similar to concrete models, selected reinforcement material model requires basic mechanical characteristics such as yield stress,  $\sigma_y$ , Young's modulus,  $E$ , Poissons's ratio,  $\nu$ , unit weight,  $\rho$ .

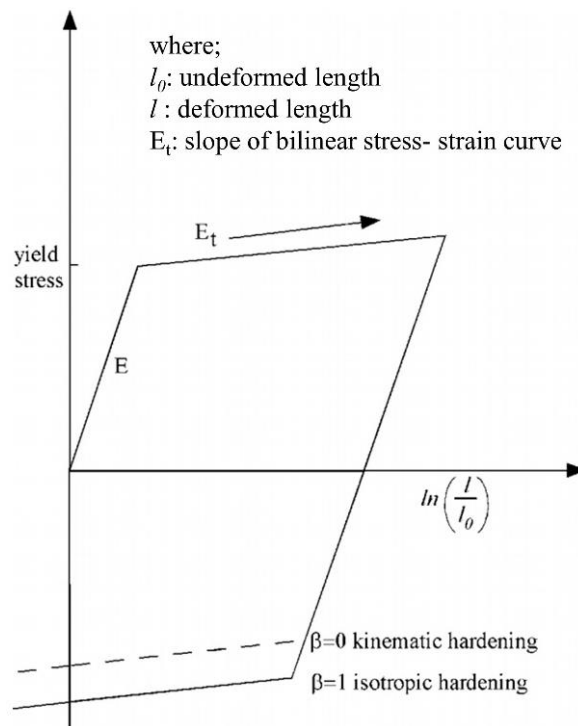


Figure 5.3. Elastic-plastic behavior with kinematic and isotropic hardening (source: LS-DYNA User's Manual, 2020)

Lastly, in the finite element simulations, the rigid material model (MAT\_020) was used for the striker, and the plates on both faces of specimen at the supports. This material model is very cost-efficient because the history variables are not stored in the memory during the computational analysis. Similar to concrete and reinforcement material models, rigid material model is also so-called "simple-input" material model that requires basic material properties such as Young's Modulus,  $E$ , and Poisson's Ratio,  $\nu$ , with the intent of calculating interactions between contacts.

### 5.1.2. Erosion Criteria

The determination of erosion criteria is one of the controversial parameters in the numerical investigations of RC structures in the literature. Yet, it can be said that the general consensus of the erosion algorithm in numerical investigations is to avoid detrimental effects on the accuracy of results. Additionally, numerical erosion is an unavoidable parameter not only to represent reality in some cases but also to satisfy numerical stability depending on the computational code such as Lagrangian. To obtain the response of structural dynamics problems with limited deformations, Lagrangian description (where the mesh is embedded in material and deforms with it) is preferred in FE analyses (Zukas, 2004).

Erosion can be described as the deletion of an element from numerical calculation when a predefined limit is reached. When the element undergoes extreme deformations in the case of erosion algorithm's absence, this may cause "lock-up" which leads to numerical instabilities (Zukas, 2004). To overcome this challenge, different types of erosion limits are made available in FE tools. These limits are summarized into three main criteria: (i) stress-based, (ii) strain-based, and (iii) damage-based (Luccioni et al. (2013); Nagendra Babu (2016))

In the literature, different types of erosion limits were employed by researchers with the intent to validate the numerical investigations on RC members subjected to different types of dynamic loading conditions (e.g. impact, blast, seismic) and ballistic tests. For instance, Sangi (2011) performed a numerical study on impact behavior of beams and slabs under low-velocity falling-weight impacts. In this study, two types of concrete models, Concrete Damage (MAT\_72) and Winfrith (MAT\_084) were used and presented. Plastic Kinematic Model (MAT\_03) was employed for the steel reinforcements. Additionally, mesh sensitivity analyses were performed to reveal the influence on displacement histories by using Winfrith Concrete Model. It is shown that peak displacements were increasing as the meshes were getting finer. The erosion algorithm based on maximum principal strain was used and assigned as 0.10 and 0.20 for concrete and steel material models, respectively.

A study on small-scale RC beams subjected to high-velocity impact loads was investigated both experimentally and numerically by Changiz Rezaei (2011). A total of 26 beams with varying transverse reinforcement ratios were tested and modeled by

using LS-DYNA software. According to this study, the concrete elements modeled with Winfrith Concrete Model were set to erode when the principal tensile strain exceeded 0.05.

Another numerical study on both normal and high strength concrete panels reinforced with high strength vanadium reinforcements was performed by Vasudevan (2012). In this study, the Karagozian & Case and the Winfrith Concrete Models were employed and compared with varying mesh sizes. Similar to the previous studies, the peak deformations were increasing as the meshes were getting finer with a constant erosion parameter. The erosion limit was defined for concrete material as a maximum principal tensile strain of 0.01.

Thai and Kim (2014) performed a finite element study on punching capacities of RC walls subjected to missile impacts. In this study, FE models were verified by the occurrence of perforation of the missile and scabbing area of RC wall specimens. Similar to the previous studies, Winfrith Concrete Model and Plastic Kinematic Model were used for concrete and steel reinforcements. The failure strain criterion in the erosion algorithm was employed as maximum principal strain and set as  $\pm 0.075$  and 0.20 for concrete and steel reinforcements, respectively.

Thai et al. (2018) carried out a parametric study on RC panels with different longitudinal and transverse shear reinforcements subjected to impacts with velocities in the range of 50 m/s – 250 m/s. In this study, Winfrith Concrete Model and Plastic Kinematic Model were used for concrete and steel reinforcements, respectively. According to this study, it is reported that the scabbing area of concrete and the residual striker velocity were sensitive to concrete erosion parameter when it is set in the range of 0.05-0.10 principal strain. The erosion criterion was selected based on a trial-and-error analysis, validating the FE analyses by using existing tests in the literature.

As it can be seen from these summarized studies, the erosion algorithm and its limits for concrete material are still blurry, and there is a need for further continuum damage mechanics investigations under dynamic loading conditions. Accounting for the studies and recommendations from the literature, the failure criteria of the materials used in the tests were determined by trial-and-error analyses. As a result of these analyses, the erosion limits were fixed as maximum principal strain in this study and they were set as 0.10 and 0.20 for concrete and steel reinforcements, respectively. The strain limits for textile reinforcements were used the same as their ultimate tensile strain capacities which are previously given in Chapter 3.

### 5.1.3. Mesh Sensitivity Investigations

To obtain the most accurate and the most efficient mesh size, several models with different meshes were created and examined in the LS-DYNA FE tool. Starting from a coarse mesh with  $20.0 \text{ mm} \times 20.0 \text{ mm} \times 20.0 \text{ mm}$  element size (one-tenth of the slab thickness), finer meshes were created and examined to the full extent of computational power. The computational capability is afforded by a designated workstation with an 8-core Intel Xenon 4110 2.10 GHz processor and 64 GB installed memory (RAM) capacity. Among these analyzed models, two of them with different mesh sizes are presented here. These two models had the same modeling parameters except the element size in the concrete sections.

The first model, named Mesh#1, and its cross-sectional view for the unstrengthened specimen is depicted in Figure 5.4. In this mesh, the element size remained constant as  $10.0 \text{ mm} \times 10.0 \text{ mm} \times 10.0 \text{ mm}$  (one-twentieth of the slab thickness) in each direction. The model with Mesh#1 consisted of 113911 elements in total.

The second model with varying element sizes is presented in Figure 5.5. This mesh was created as two separate parts; (i) an assumed punching cone region around the impact vicinity, (ii) the rest of the slab. A box section was created as an assumed punching cone region, starting from the midpoint of the specimen where impact incident occurs. In this region, the element size of the mesh remained constant as  $5.0 \text{ mm} \times 5.0 \text{ mm} \times 5.0 \text{ mm}$  along the 300 mm of slab specimen in x and y directions. Beyond this point, the element sizes in the x and y directions were increasing gradually with the 1.01 growth rate. The aim of creating a gradual mesh (Mesh#2) is not only to reveal the element size effect at the impact vicinity but also to overcome high computational demands and time cost. The number of total elements for Mesh #2 was 577411.

The overall views of the slab specimen for Mesh #1 and Mesh#2 can be seen in Figure 5.6.

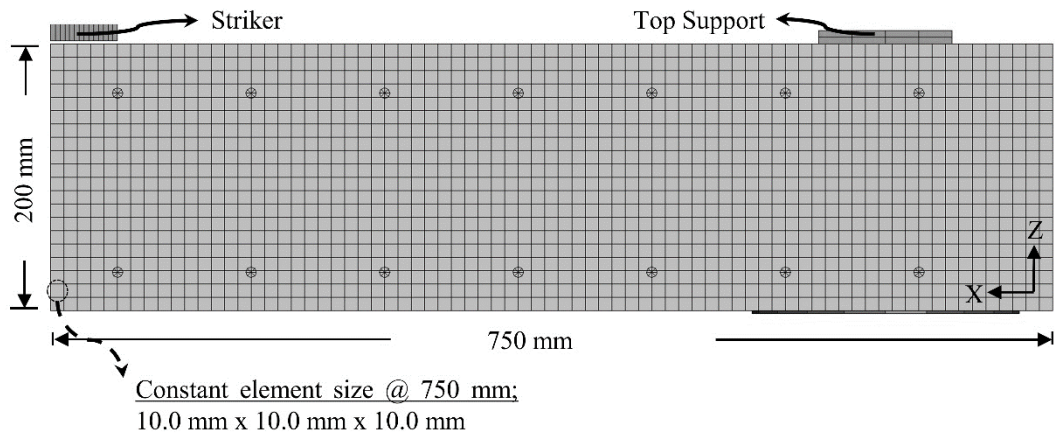


Figure 5.4. The model with Mesh#1

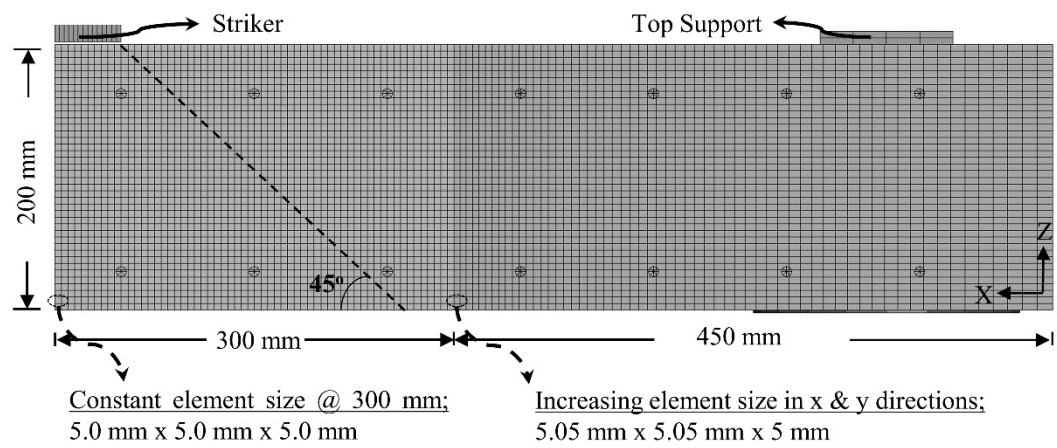
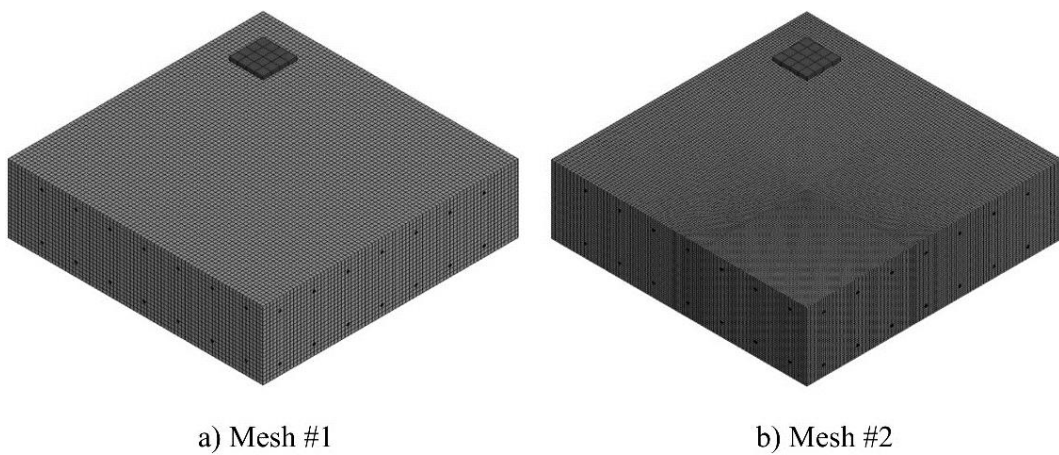


Figure 5.5. The model with Mesh#2



a) Mesh #1

b) Mesh #2

Figure 5.6. The created models with varied element sizes

### 5.1.3.1.S1T0 Specimen

The created models of S1T0 specimen by using the two different meshes were analyzed, as explained before. The displacement-time histories of the created meshes of S1T0 specimen for the first and second impacts are presented in Figure 5.7. As it can be clearly seen from Figure 5.7a, the maximum displacements were 8.0 mm and 8.2 mm and the residual displacements at rest were 2.5 mm and 2.6 mm for Mesh#1 and Mesh#2, respectively. However, the model with the finer mesh reached higher peaks compared to the coarse mesh in the post-impact phase until specimens rested at 100 milliseconds.

At the second impact, the difference between maximum midpoint displacements of the meshes increased to approximately 10 mm, whereas the residual displacements of these meshes were the same. However, both meshes employed in the models predicted lower peaks at the midpoint compared to the test. It should be noted here that the captured displacement signals were not trustworthy after 15 milliseconds due to spalling of concrete (Figure 5.7b) which was explained earlier.

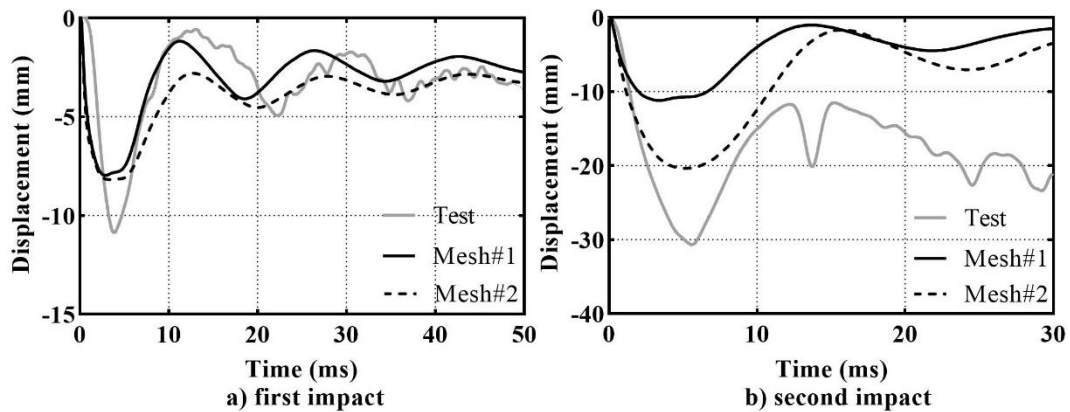


Figure 5.7. The midpoint displacement-time histories of S1T0 for the analyses and tests

The total reaction force-time histories of the analyzed models and tests for the first and second impacts of S1T0 specimen are depicted in Figure 5.8. In both impacts, the models overestimated the total reaction forces in compression developed at the very beginning of the impact history. As it can be seen in Figure 5.8a, the overshoot in calculated compressive reactions (negative region) for the first impacts was more than fivefold compared to tests, whereas they decreased for both models in the second impacts where inherited damage existed (Figure 5.8b). Beside these overestimations, it

can be said that both models were in good agreement with the rest of the total reaction responses in both tests. In general, the models created with Mesh#1 and Mesh#2 achieved to estimate the total reaction responses for the first and second impacts, considering the number of cycles in the response and the peak values in the post-impact phases.

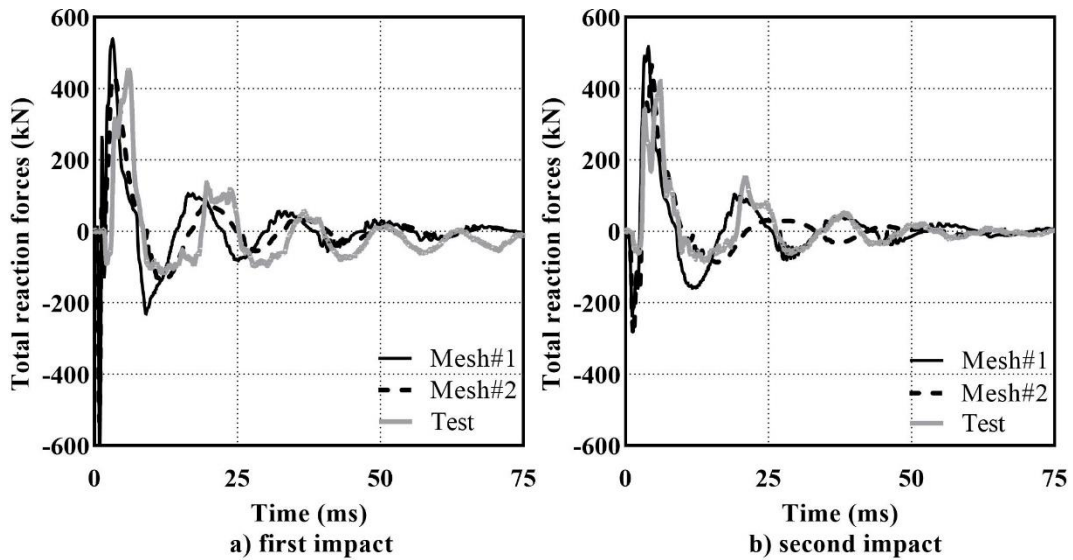


Figure 5.8. The total reaction force-time histories of S1T0 for the analyses and tests

To make a visual comparison and damage pattern examination between FE analyses and tests, the cross-sections of the models and the specimen were compared. As it can be seen in Figure 5.9, the punching cone boundaries drawn by the eroded elements are fairly obvious in Mesh#2 compared to Mesh#1. This can be explained as an effect of the number of eroded elements which is higher due to assigned element size. Similarly, higher penetration depth occurred in Mesh#2 due to a higher number of eroded elements in contact with the striker compared to Mesh#1. The total penetration depths from the analyses were 24.8 mm and 9.4 mm for Mesh#1 and Mesh#2, respectively whereas the measured total penetration from the test was 20.0 mm. When the accuracy of the striker penetration depth is considered, Mesh#1 was 80% accurate whereas the accuracy of Mesh#2 was 47% in total after the second impacts.

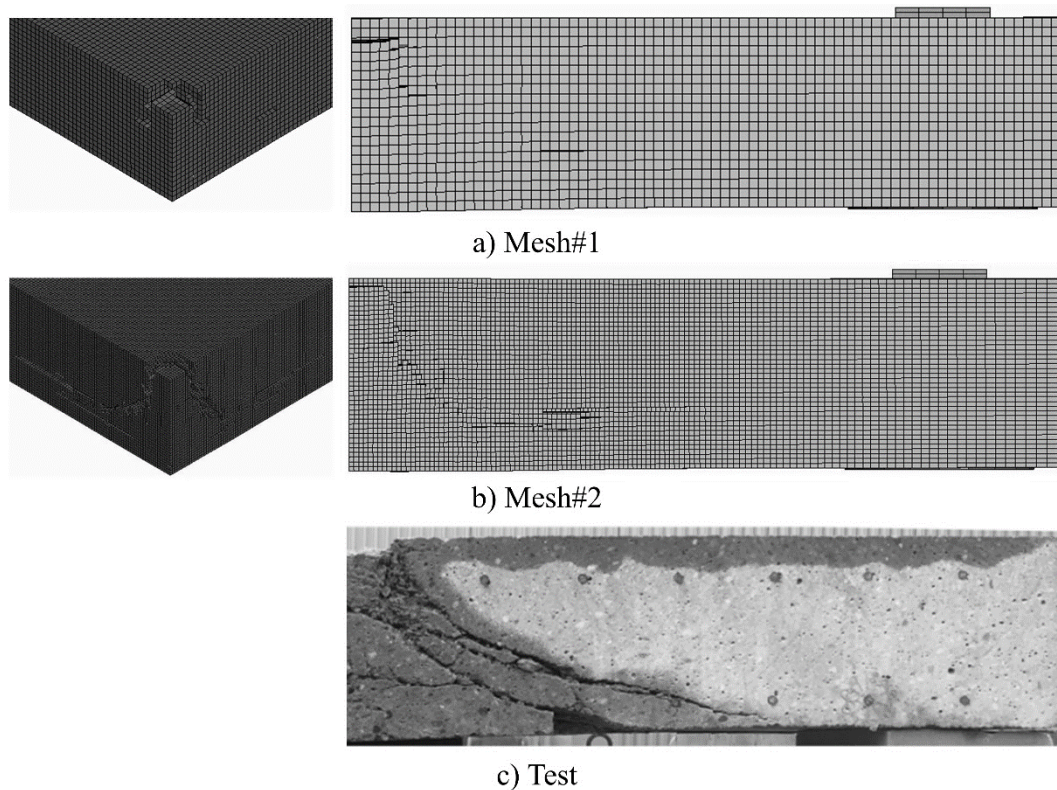


Figure 5.9. Punching cone formations in test and models for S1T0 specimen

### 5.1.3.2. S2T0 Specimen

The displacement-time histories of the following unstrengthened specimen, S2T0, are presented in Figure 5.10a and Figure 5.10b. It should be reminded that the S2T0 specimen was subjected to impact loads by means of the same striker with a higher contact velocity. Unlike the predicted maximum and residual displacements in the previous specimen impact tests, Mesh#1 and Mesh#2 predicted different maximum and residual displacements at the first impact. The maximum and residual displacements were 9.9 mm and 2.9 mm for Mesh#1, respectively, whereas they were 12.0 mm and 3.9 mm for Mesh#2.

As a result of the difference in damage levels suffered from the first impacts, the displacement profiles of Mesh#1 and Mesh#2 also differentiated from each other. The model with the finer mesh, Mesh#2, had higher maximum and residual displacements than the coarser mesh, Mesh#1, resulting in a higher damage level (Figure 5.10b). However, it can be said that this inherited damage level within the Mesh#2 caused extreme deflection at the midpoint and excessive damage level around the punching cone in the analysis of the following impact compared to the test. It should be reminded

here that the collected displacement signals after 15 ms in the second impact test were not trustworthy due to the blocking of signals by debris and scabbed concrete. Additionally, the penetration of the striker for both meshes is approximately the same, having around 80% accuracy.

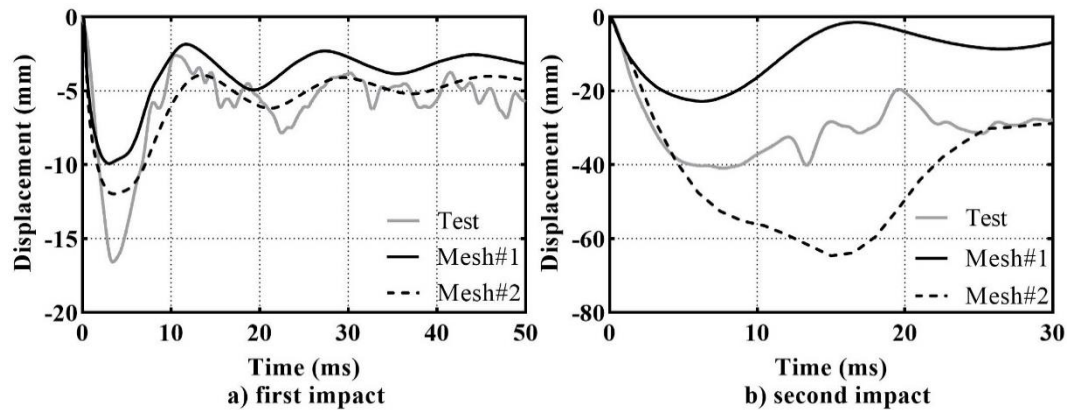


Figure 5.10. The midpoint displacement-time histories of S2T0 for the analyses and tests

The total reaction forces computed from the models and obtained from the test are presented in Figure 5.11. As depicted in Figure 5.11a, the models overestimated the forces in compression developed in the first few milliseconds similar to the models of the previous specimen. Furthermore, the reaction force responses of both models were in good agreement in the post-impact phase of the first impact. However, the models were not able to estimate the total reaction response fairly in the second impact (Figure 5.11b). The FE model with Mesh#1 computed the peak reaction approximately twice the peak reaction force measured in the test. Similarly, the model with Mesh#2 estimated a 50% higher peak reaction force than the peak at the test. Moreover, in the post-impact phase, Mesh#1 estimated higher peak values in the following cycles, whereas Mesh#2 computed lower peaks until the rest. Similar to the previous specimen, the computed reaction forces in compression for both models decreased in the second impacts which were still far from the actual compression forces measured from the test.

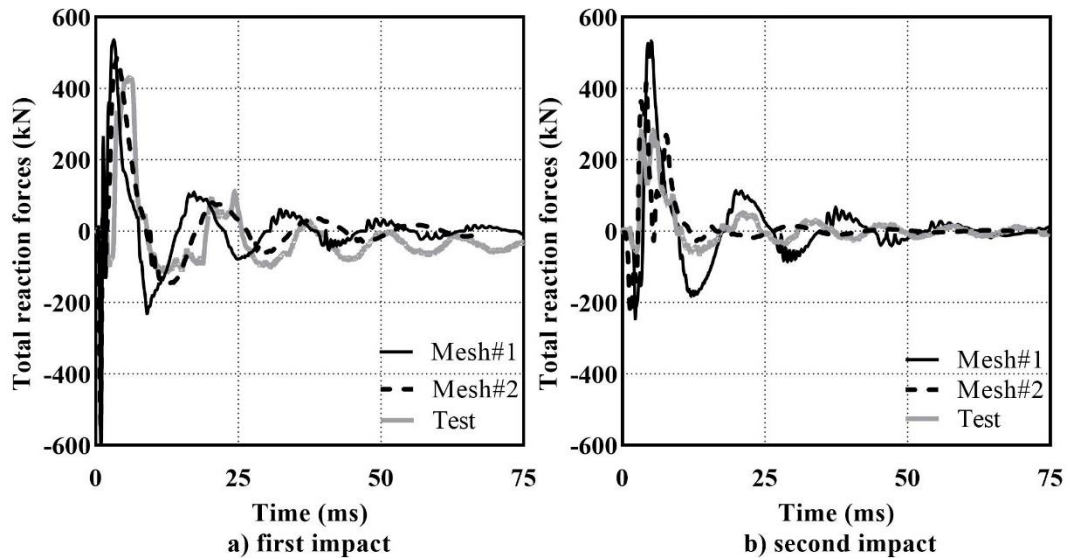


Figure 5.11. The total reaction force-time histories of S2T0 for the analyses and tests

With the intent to compare the FE models with the tested S2T0 specimen visually, the cross-sectional views of models and test specimen are displayed in Figure 5.12. As it can be seen from the figure, the eroded element numbers in Mesh#1 were not as high as element numbers in Mesh#2 at the punching cone vicinity, causing higher damage levels in the specimen body. When the visual comparison is made between FE models and tested specimen, it can be said that the model with Mesh#2 is more analogous with the specimen in terms of damaged or decomposed concrete parts in the body. However, both models were able to predict the perforation depths with an accuracy of 80 % in total.

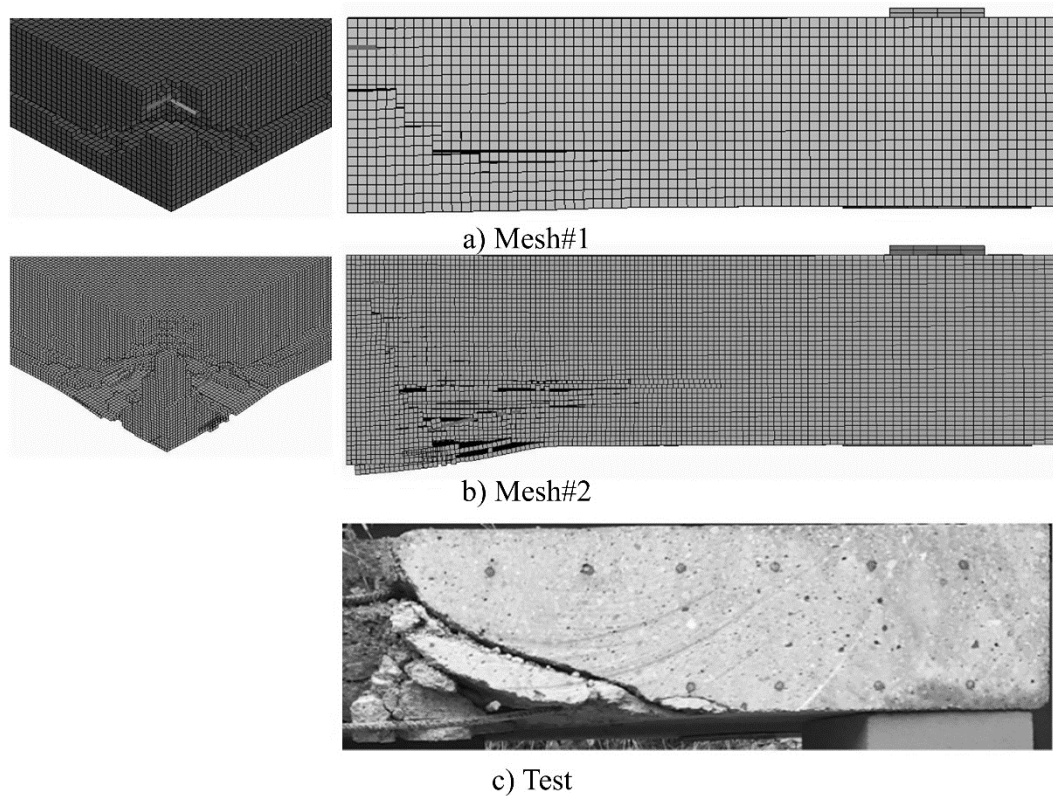


Figure 5.12. Punching cone formations in test and models for S2T0 specimen

### 5.1.3.3. S3T1 Specimen

The displacement-time histories of the strengthened specimen with the least textile reinforcement ratio, S3T1, can be seen for the first and second impact tests in Figure 5.13a and Figure 5.13b. It should be noted here that the S3T1 specimen was tested under the same impact loading four times until perforation occurred. However, at the third and fourth impacts, the laser sensor located at the midpoint was not able to capture reasonable measurements due to debris created in the course of tests. Therefore, the midpoint displacement-time histories are presentable merely for the first and second impact tests. Additionally, with the developing cracks at the bottom face of the specimens during the impacts, unreasonable peaks appeared on the displacement profiles. These discrepancies are presented as gray-scale dotted lines in Figure 5.13a. Similar to the S1T0 specimen's displacement-time history at the first impact test, both created models predicted the same peak midpoint displacement as 6.8 mm, whereas the oscillations beyond the peak displacements differentiated from each other. Mesh#2 reached the peaks at higher values in the post-impact cycles, resulting in higher residual displacement. Similar to peak deflection prediction at the midpoint, the striker

penetrations were quite close to each other, 2.8 mm and 3.5 mm for Mesh#1 and Mesh#2, respectively.

At the second impact, it can be said that the predicted displacement responses of both meshes were the same, contrary to the displacement profiles of the models for the S1T0 specimen at the second impact. However, as it can be seen from Figure 5.13b, both created models predicted lower displacement response when the comparison is made between the models and test. Despite having low accuracy on the displacement response prediction of Mesh#2, the depth of striker penetration in the FE model with Mesh#2 had 70 % accuracy. Even though Mesh#1 had a similar displacement-time history with Mesh#2, the penetration depth was 25 % of the actual penetration depth at the second impact test.

As explained before, the midpoint displacement responses are presentable and comparable for only the first and second impacts. On the other hand, both created models employed in simulations predicted that the specimens can survive after three repeated impacts and can be perforated at the fourth impact.

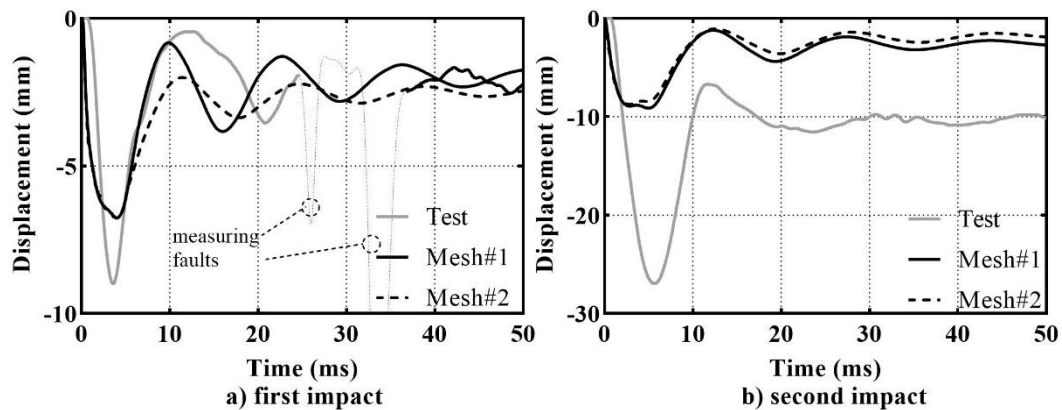


Figure 5.13. The midpoint displacement-time histories of S3T1 for the analyses and tests

The total reaction force-time histories of FE models and the tests are depicted in Figure 5.14. The reaction responses in the created models were generally in good agreement with the response measured in the test for the first impact of S3T1 specimen (Figure 5.14). Similar to the unstrengthened specimens, the FE models for both meshes estimated unreasonable high compression forces at the beginning of impact events compared to the forces measured in the test. In the following impacts, the over-estimated compression forces in the models were decreasing in accordance with the

increase in the damage levels of the specimen. In the second impact, both FE models were able to predict the full reaction response very well as depicted in Figure 5.14b. In the following impact, the peak reactions were estimated by the models with good accuracy, whereas the computed forces dissipated quickly in the models compared to the measured reaction in the post-impact phase (Figure 5.14c). The models predicted relatively higher peak reactions compared to the measured reaction in the fourth impact, as displayed in Figure 5.14d. It should be reminded here that the S3T1 specimen was perforated at the fourth impact.

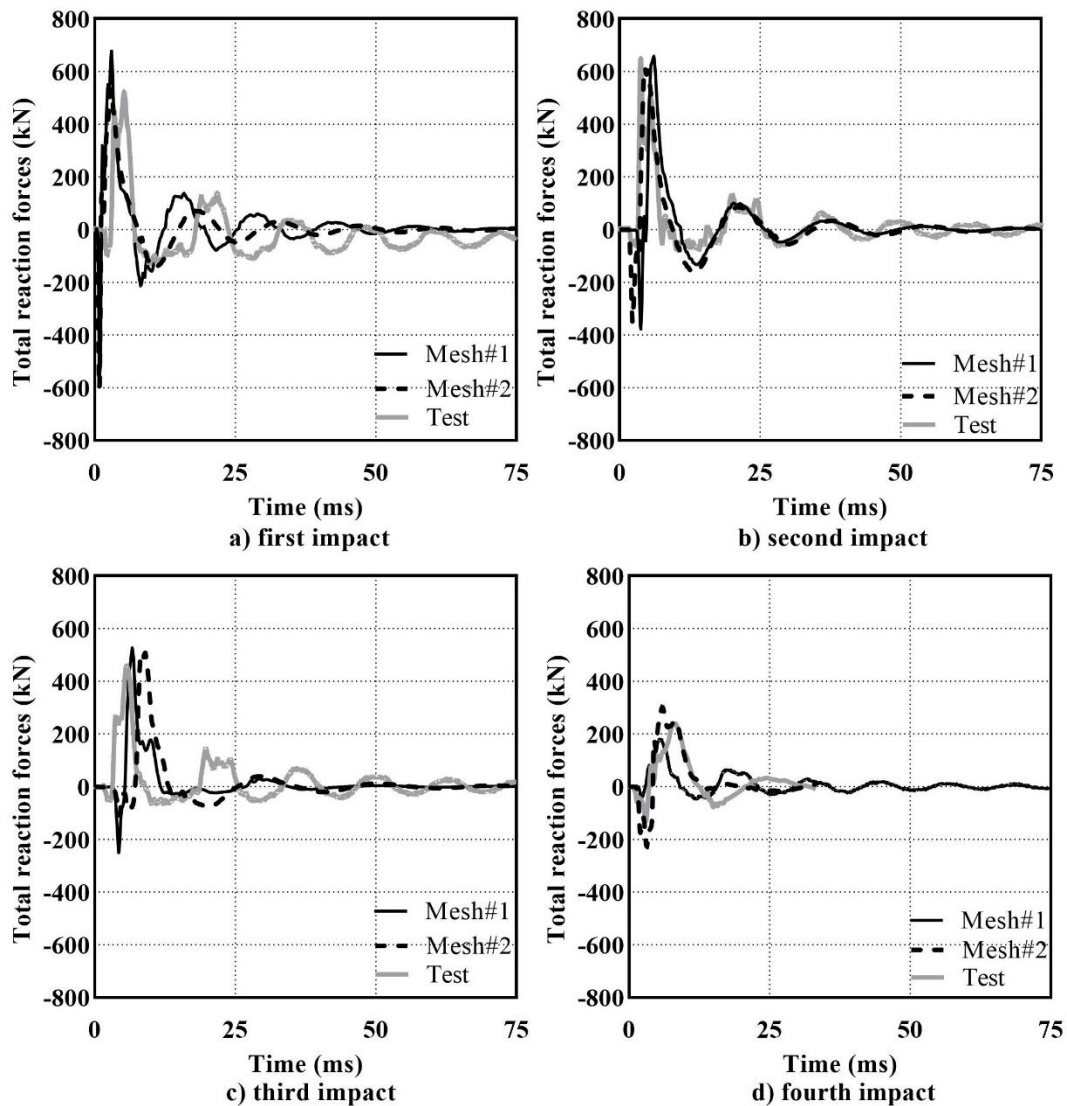


Figure 5.14. The total reaction force-time histories of S3T1 for the analyses and tests

The final states of the FE models of S3T1 specimen after four impacts showed the highest dissimilarity between each other among the analyses of employed specimens. As it can be seen from Figure 5.15, the model with the Mesh#2 had a higher number of elements disconnected from the bottom surface. However, it can be said that both models were able to predict punching cone geometry and possible concrete scabbing around the punching cone, whereas they predicted higher penetration depths until perforation failure.

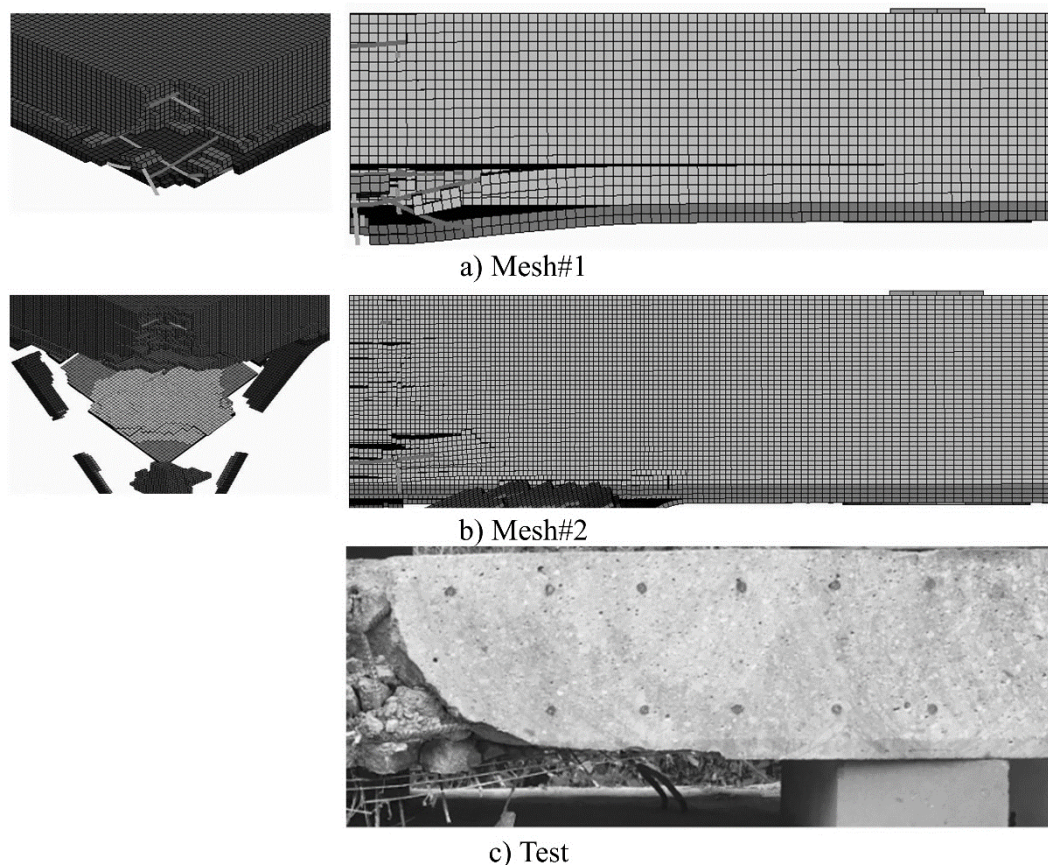


Figure 5.15. Punching cone formations in test and models for S3T1 specimen

#### 5.1.3.4. S4T2 Specimen

The displacement-time histories of S4T2 specimen which had the highest textile reinforcement ratio are presented in Figure 5.16. Similar to the S1T0 and S3T1 specimens, the created models with both meshes predicted 6.2 mm peaks at the midpoints in the first impacts but the displacement response differentiated from each other in the post-impact cycles until resting (Figure 5.16a). The predicted residual displacements after the first impacts were quite close to each other with 90% accuracy.

At the second impacts, the predicted peaks at the midpoints of both meshes were very close whereas the accuracy of the models for both meshes was lower, 50 %. Similar to the peak displacement predictions, both models insufficiently predicted residual displacements with 50 % accuracy (Figure 5.16b).

The predicted displacement-time histories of the models started to differentiate, starting from the third impact. Despite the peak midpoint displacements were predicted equally by both models as 12.0 mm, a delay between the peaks was observed, and the residual displacement at rest for Mesh#1 was higher than Mesh#2 (Figure 5.16c). Also, starting from the third impacts, the predicted penetration depths were quite higher than the actual measurement obtained from the third impact test.

As it is presented, both models predicted more conservative peak displacements at the midpoint until the fourth impacts. Starting from the fourth impact, the damage levels in the models were increasing significantly. In parallel with the damage levels, the predicted deflections and penetration depths were significantly higher than test measurements. As it can be seen in Figure 5.16d, the predicted peak midpoint displacement of Mesh#1 was 30% higher than the test. Moreover, the increase in damage level in Mesh#2 caused excessive element deletion in the vicinity of the midpoint. Therefore, due to erosion, the midpoint displacement-time history of this mesh cannot be presented.

Due to the damage levels in both meshes inherited from the fourth impacts, the fifth impact was the final straw for both meshes and a perforation failure occurred at the fifth impacts. It should be reminded here that the tested specimen, S4T2, could resist the fifth impact and it was perforated in the sixth impact test.

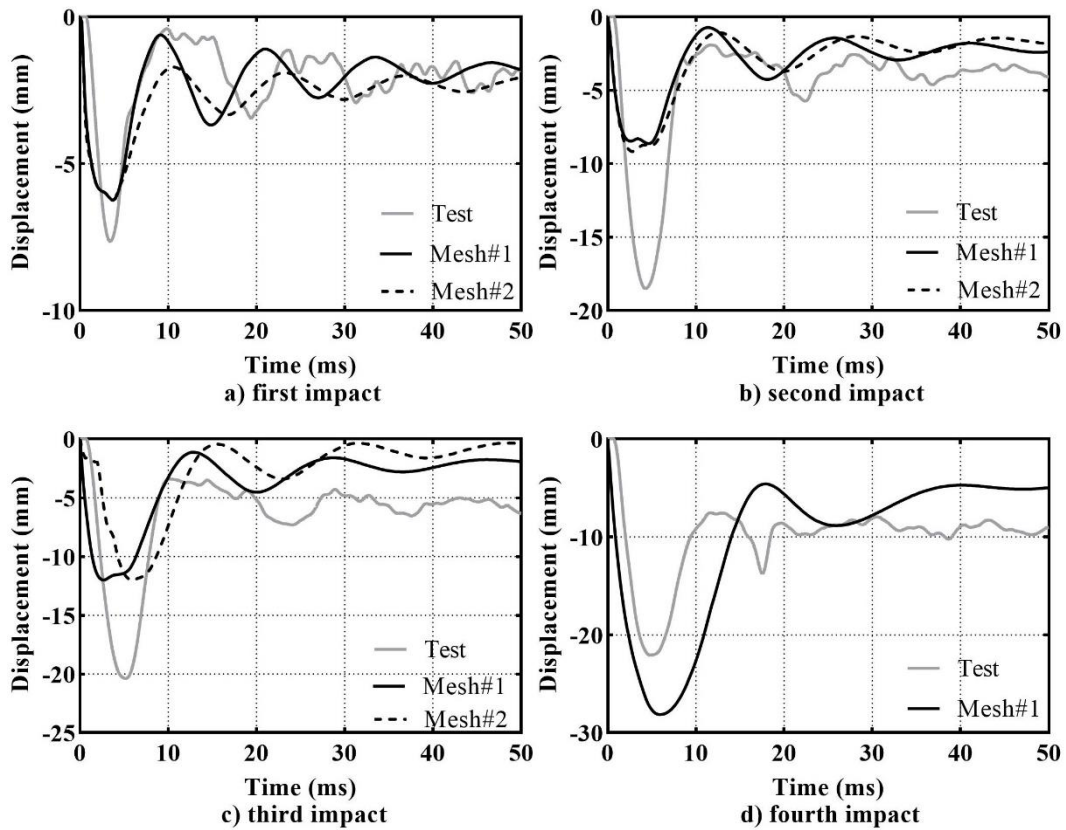


Figure 5.16. The midpoint displacement-time histories of S4T2 for the analyses and tests

The total reaction-time histories computed from FE analyses and measured from tests are displayed in Figure 5.17. Similar to the previous specimens, in the first impacts, the created models by using Mesh#1 and Mesh#2 had good agreement with the overall response measured in the tests with the accurate peak reactions in the order of 80 to 90 % (Figure 5.17a). Similar to the other specimens, the FE model had overestimated compression reactions in the first few milliseconds. Nevertheless, as in the other specimens' reaction responses, the degree of overestimation was decreasing inversely related to the damage level in the specimen. In the following impact, the models were able to predict the peak reactions until the rest (Figure 5.17b). However, in the third impact, the reaction response computed by the model with Mesh#1 showed good agreement with the measured response, whereas the model with Mesh#2 was not able to catch the peak reaction in the course of impact (Figure 5.17c). Similarly, the model with Mesh#1 computed better reactions than the other model in the fourth impact, as it can be seen in Figure 5.17d. The reaction responses for both models failed to predict the response for the fifth impact. It should be noted here the FE models were

perforated in the fifth impact, whereas the S4T2 specimen was perforated in the sixth impact.

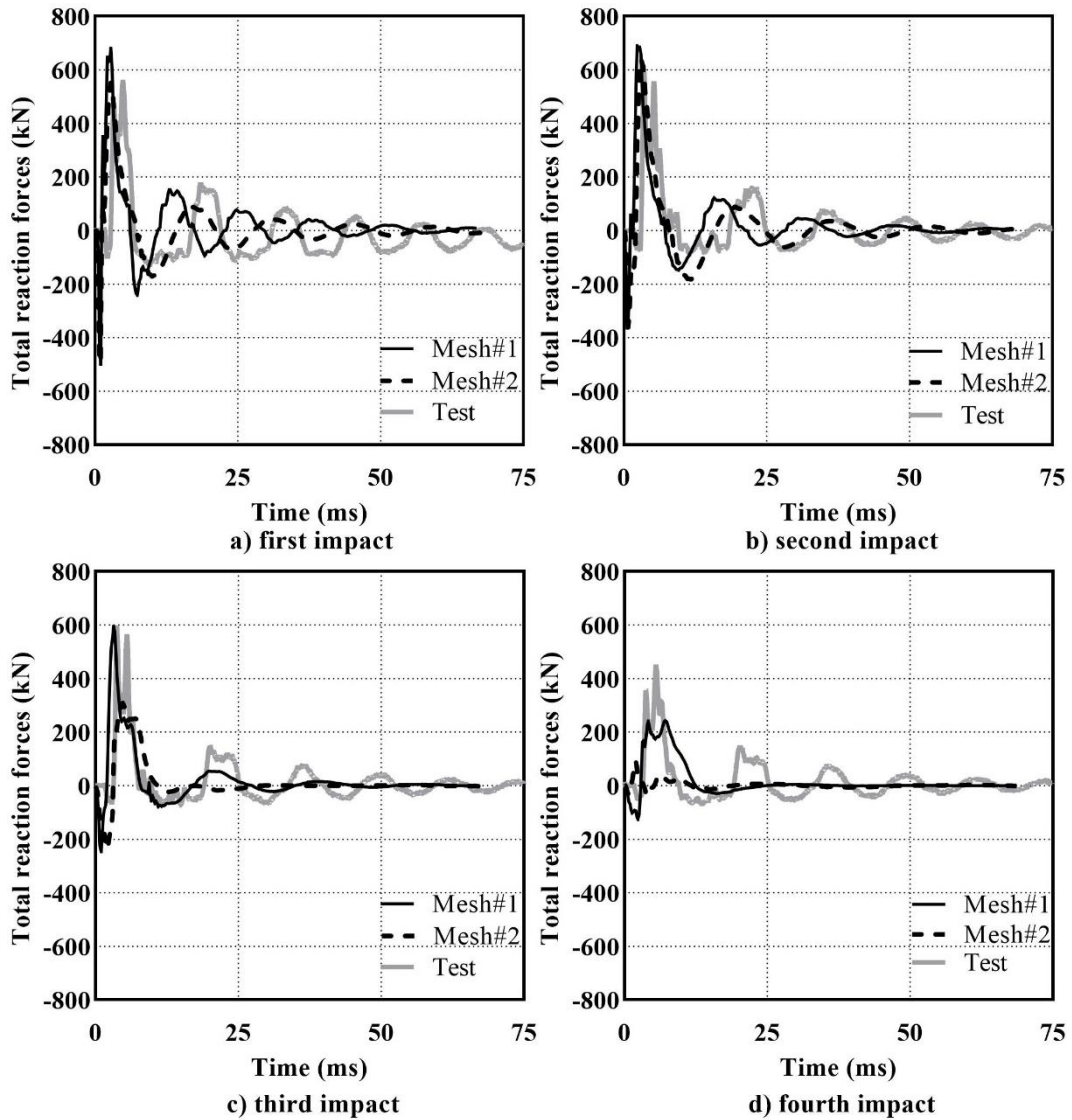


Figure 5.17. The total reaction force-time histories of S4T2 for the analyses and tests

To make a visual comparison after final impacts, the cross-sectional views of the FE models and tested specimen are displayed in Figure 5.18. Similar to the unstrengthened specimens, the created FE models were able to predict the punching cone geometry. However, the predicted penetration depths for both models were not accurate enough in each impact, resulted in perforation failure earlier than the test.

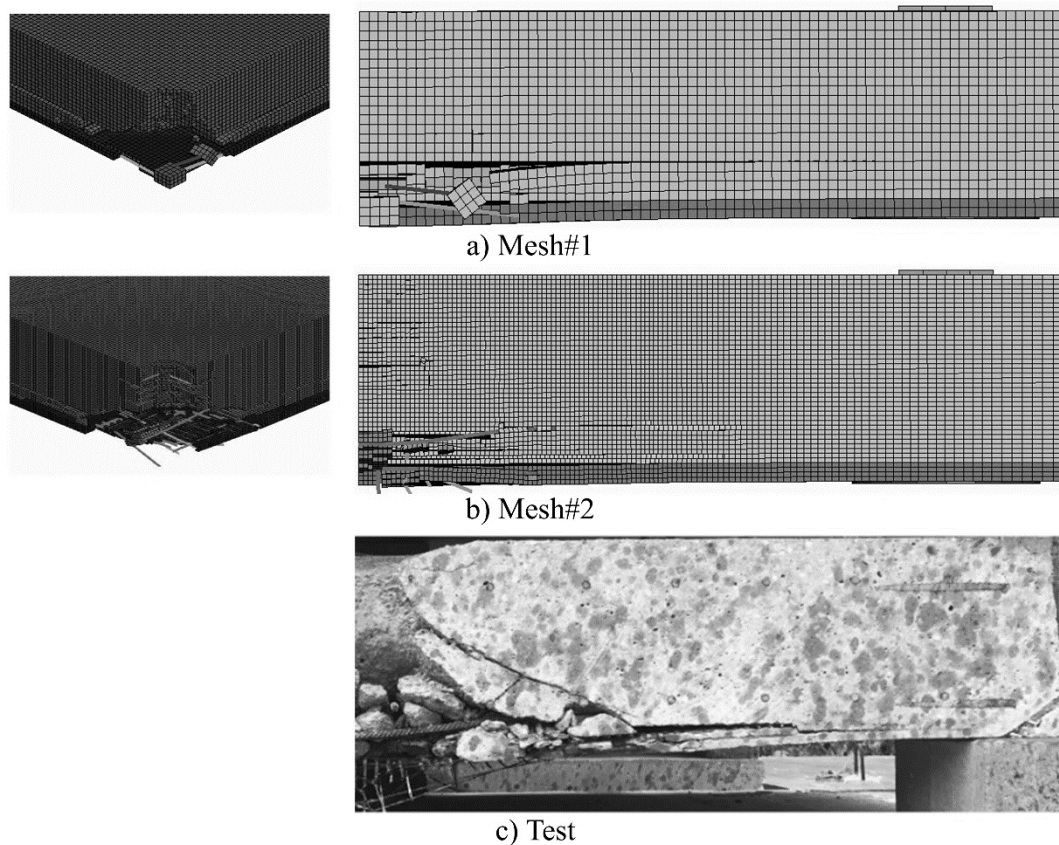


Figure 5.18. Punching cone formations in test and models for S4T2 specimen

### 5.1.3.5. Summary of Finite Element Modeling Investigations

As explained earlier, the thesis presented herein is aiming to contribute to the literature on the impact behavior of carbon-textile reinforced RC members in various ways. One of the goals is to provide well-documented data sets by using a well-instrumented testing program. The next goal is to implement a numerical study by using a finite element tool to present properly validated simulations for further studies and investigations. Therefore, several FE models were created with different parameters such as varied mesh sizes and different material models and employed in LS-DYNA FE software. Among these models, two of them, Mesh#1 and Mesh#2, were worth to be considered as candidates for further inspections. Thus, they were examined in detail for proper validation. To do that, results obtained from these models are presented in terms of displacement-time histories, reaction force-time histories, and damage patterns for each specimen after each impact. However, before comparing the structural benchmarks, the reliability of the simulations must be checked.

As mentioned earlier, eight-node hexahedron solid elements were employed for solid sections. The volume integration of each solid element was acquired by Gaussian quadrature with a one-point integration method. This method is extremely time-saving in FE solutions and gives accurate results if hourglass modes are controlled. The hourglass mode is caused by the unchanged dimension of the element despite the element undergoes deformation. To overcome hourglassing, the number of integration points in the element formulation can be increased, which can lead to higher computational demands. Refining the mesh is an alternative solution to overcome hourglass modes. The hourglass energy is expected to be remained under 10% of the internal energy in the simulations to provide stable solutions (LS-DYNA, 2006). Therefore, after completing each analysis, the energy levels were checked to prevent non-negligible effects on the results. The hourglass energy for each impact test was below the indicated limit. The typical energy levels for both created meshes are displayed in Figure 5.19.

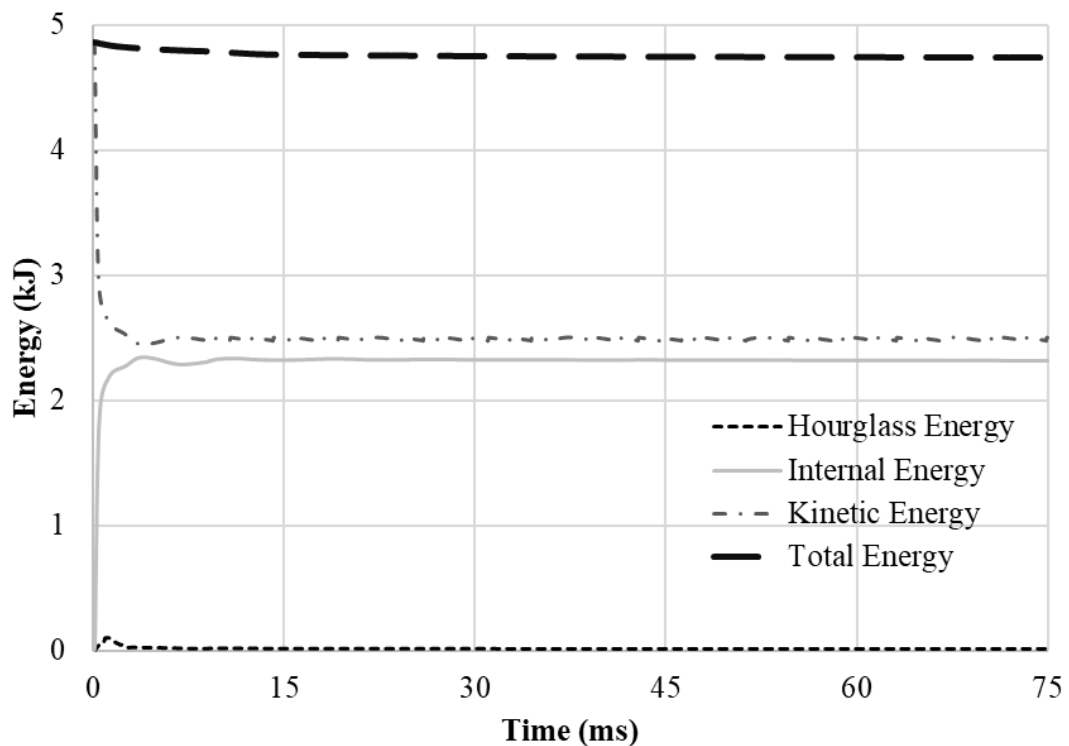


Figure 5.19. The typical energy levels in the models

As presented earlier, the displacement profiles at the midpoint were examined for each impact, and comparisons were made between the created FE models and the test data. All midpoint displacement results from FE analyses and measured data from

the tests are tabulated in Table 5.1. It can be said that both meshes predicted the peak midpoint displacements with high accuracies in the first impact tests. Similarly, the accuracies were high in predicting residual displacements. However, starting from the second impact tests, the accuracies were decreasing for both meshes. It should be noted here that with the increase of damage level in the specimens, the decrease in the accuracy levels of the predictions in the subsequent impact tests was expected to be observed due to the complex impact behavior mechanisms such as localization at the impact vicinity and plastic behavior of materials after peak levels.

Table 5.1. The midpoint displacements from the FE analyses and tests

Slab - Impact #	Midpoint displacements* (mm)									
	Peak					Residual				
	Test	FE Analysis				Test	FE Analysis			
		Mesh#1	M1/T <sup>†</sup>	Mesh#2	M2/T <sup>†</sup>		Mesh#1	M1/T <sup>†</sup>	Mesh#2	M2/T <sup>†</sup>
S1T0-1	11.2	8.0	0.71	8.2	0.73	3.3	2.5	0.76	2.6	0.77
S1T0-2	31.2	11.2	0.36	20.4	0.65	N/A	2.0	-	2.2	
S2T0-1	16.5	9.9	0.60	12.0	0.73	4.9	2.9	0.59	3.9	0.80
S2T0-2	41.0	22.9	0.56	64.6	1.58	N/A	4.0	-	29.4	-
S3T1-1	9.0	6.8	0.76	6.8	0.76	2.1	1.9	0.90	2.4	1.14
S3T1-2	27.0	9.1	0.34	8.8	0.33	10.1	2.5	0.25	1.6	0.16
S3T1-3	N/A	25.0	-	14.4	-	N/A	2.6	-	0.8	-
S3T1-4	Perf.	Perf.	-	Perf.	-	Perf.	Perf.	-	Perf.	-
S4T2-1	7.7	6.2	0.81	6.2	0.81	2.0	1.9	0.95	2.1	1.05
S4T2-2	18.6	8.6	0.46	8.7	0.47	4.0	2.1	0.53	1.7	0.43
S4T2-3	20.4	12.0	0.59	12.0	0.59	6.0	1.7	0.28	0.5	0.08
S4T2-4	22.2	28.0	1.26	N/A	-	9.0	3.4	0.38	N/A	-
S4T2-5	16.7	Perf.	-	Perf.	-	11.8	Perf.	-	Perf.	-
S4T2-6	Perf.	-	-	-	-	Perf.	-	-	-	-

\* Displayed for the individual impacts, not accumulated from the previous events

† Mesh-to-test ratio

With the intent to summarize the predicted and measured penetration depths, results are tabulated in Table 5.2. Similar to midpoint displacements, created models were able to estimate the penetration depths with high accuracy in the first impacts for each specimen. In the following impacts, Mesh#1 predicted penetration depths with lower accuracy, whereas Mesh#2 was able to catch the penetration depths with higher accuracy. It can be said that the element size had an influential effect on the accuracy due to the number of eroded elements in Mesh#2 interacted with the steel striker.

Table 5.2. The penetration depths of the striker from the FE analyses and tests

Slab-Impact#	Penetration Depth* (mm)				
	Test	FE Analysis			
		Mesh#1	M1/T <sup>†</sup>	Mesh#2	M2/T <sup>†</sup>
S1T0-1	5.0	2.8	0.56	3.9	0.78
S1T0-2	15.0	22.0	1.47	5.5	0.37
S2T0-1	7.0	3.1	0.44	5.6	0.80
S2T0-2	56.0	75.0	1.34	43.5	0.78
S3T1-1	5.0	2.8	0.56	3.5	0.70
S3T1-2	5.0	20.1	4.02	3.5	0.70
S3T1-3	19.0	81.0	4.26	47.0	2.47
S3T1-4	Perf.	Perf.	-	Perf.	-
S4T2-1	6.0	2.4	0.40	3.5	0.58
S4T2-2	4.0	21.2	5.30	3.0	0.75
S4T2-3	8.0	40.0	5.0	65.0	8.13
S4T2-4	16.0	143.0	8.94	102.5	6.41
S4T2-5	76.0	Perf.	-	Perf.	-
S4T2-6	Perf.	N/A	-	N/A	-

\* Displayed for the individual impacts, not accumulated from the previous events

† Mesh-to-test ratio

The total reaction responses from FE analyses and tests were compared earlier, and peak reaction values are tabulated in Table 5.3 for both models and tests. As it can be seen from the table, the peak reaction forces were predicted with good accuracy in the first impacts. For the following impacts, FE models created for S1T0 and S3T1 specimens showed better results. However, accuracies of the total peak reactions were decreasing with the increase in damage levels as observed in the midpoint displacement predictions.

Table 5.3. The total peak reactions from the FE analyses and tests

Slab - Impact #	Total peak reactions* (kN)				
	Test	FE Analysis			
		Mesh#1	M1/T <sup>†</sup>	Mesh#2	M2/T <sup>†</sup>
S1T0-1	451.0	539.0	1.20	433.0	0.96
S1T0-2	420.0	513.0	1.22	466.0	1.11
S2T0-1	433.0	533.0	1.23	486.0	1.12
S2T0-2	283.0	533.0	1.88	415.0	1.5
S3T1-1	522.0	675.0	1.29	533.0	1.47
S3T1-2	653.0	657.0	1.01	614.0	0.94
S3T1-3	457.0	524.0	1.15	509.0	1.11
S3T1-4	182.0	240.0	1.32	302.0	1.66
S4T2-1	556.0	646.0	1.16	494.0	0.89
S4T2-2	592.0	690.0	1.17	641.0	1.08
S4T2-3	595.0	594.0	1.00	309.0	0.52
S4T2-4	445.0	241.0	0.54	92.0	0.21
S4T2-5	218.0	13.0	0.06	15.0	0.07
S4T2-6	47.0	N/A	N/A	N/A	N/A

\* Displayed for the individual impacts, not accumulated from the previous events

<sup>†</sup> Mesh-to-test ratio

As previously mentioned, the numerical analyses of structures can be charming for engineers and researchers due to several reasons. However, these investigations demand computational power, time, and model validation. With the aim of validation, two models with varied mesh sizes were performed. In the course of performing these investigations, the demands and costs are tabulated in Table 5.4 in terms of computational time and data sizes. It should be reminded here that the designated workstation computer with an 8-core Intel Xenon 4110 2.10 GHz processors and 64 GB installed memory (RAM) capacity was employed to the full extent of the hardware capacity.

Table 5.4. The computational demands and sizes of the FE models

Slab	Number of elements		Total comp. time (h)		Data size (GB)	
	Mesh #1	Mesh #2	Mesh #1	Mesh #2	Mesh #1	Mesh #2
S1T0	113911	577411	8.2	19.0	4.6	11.7
S2T0	113911	577411	8.2	19.0	5.2	12.2
S3T1	129087	638937	19.3	62.5	8.0	29.5
S4T2	132249	642099	36.0	94.0	17.5	27.7

In this chapter of this thesis, the findings of employed models by using a powerful FE software program are presented and compared with the tested specimens in qualitatively and quantitatively. In the light of these investigations, the following conclusions can be derived:

- i. The created three-dimensional FE models by using the aforementioned material models are mesh-dependent. Therefore, element size selection accompanied with erosion criteria on material models should be chosen meticulously,
- ii. The employed models have the ability to predict the midpoint displacement and total reaction force responses with good accuracy in the first impacts. However, the accuracy decreases for both models in the following impacts as the damage levels increase,
- iii. The element size selection has a very influential effect on estimating the penetration depth in parallel with the mesh dependency.
- iv. The FE models are able to illustrate the damage states after each impact in good agreement with the observations made from the tests.

## CHAPTER 6

### PARAMETRIC INVESTIGATION

As explained earlier, the objectives of this thesis are categorized into three main groups, covering multiple targets in each group. Up to this chapter, the planned targets are tried to be achieved by presenting a well-documented impact testing program and implementing the benchmarking FE investigations. To cover the main target of the thesis, the parametric investigations are presented in this chapter to reveal the contribution of carbon textile reinforcement to the impact behavior of RC slabs. It can be said that this parametric study presented herein is the epicenter of this thesis by outlining the impact parameters for efficient employment of carbon textile reinforcement under impact loads. For this purpose, one of the FE models presented in the previous chapter was selected to be employed in these parametric investigations. As explained earlier in detail, both FE models are able to predict the midpoint displacements, peak reactions, and damage patterns in the first impact loading with reasonable accuracy. Due to the computational demands and time cost, the model with Mesh#1, the coarser mesh, was selected. Therefore, in this chapter, the specimens used for the parametric investigations consisted of hexagonal cubic elements in concrete sections with a constant size of 10.0 mm. Additionally, the parameters and methods for specimen modeling were kept same as in the model with Mesh#1 presented in the previous chapter. By using this model, thirty slab specimens were made up and classified according to their thicknesses.

#### 6.1. Fictitious Specimens for Parametric Investigations

To investigate different parameters of impact phenomenon and reveal the contributions of carbon textile reinforcement to impact behavior, two different fictitious specimen families were created with different parameters such as varied steel bar reinforcement and carbon textile reinforcement ratios, total specimen thickness, striker velocity, and diameter of striker. Therefore, firstly, nine slab specimens having the same thickness as the specimens employed in the testing stage were created as Family#1. These specimens were subjected to the same impact loads as in the tests by means of

using the same steel striker with 26 m/s contact velocity until total perforation failure occurred. Following these FE analyses, twenty-one slab specimens were created as Family#2. The specimens in this family were designed to be thinner than the specimens in Family#1, and they were subjected to low-velocity impact loads with varied striker mass and diameter. These two fictitious specimen families consist of 30 slab specimens in total with varied thicknesses, whereas all of them have the same dimensions of  $1.50 \times 1.50$  m in the x- and y- directions, same as in the tests. All these fictitious specimens were created by using the FE model with Mesh#1 presented in the previous section and analyzed in LS-DYNA FE software.

In a similar manner to the specimen geometry selection, the mechanical characteristics of steel reinforcement, carbon textile reinforcement, normal concrete, and fine-grained concrete employed in the FE models were selected to be the same as in the specimens used in the testing phase. However, to reveal the effects of reinforcements, the spacings between the steel bars and the spacings between rovings of the carbon textile reinforcement were varied. For computational convenience, only one layer of carbon textile reinforcements with identical properties in both orthogonal directions was employed as a strengthening reinforcement in these FE investigations. As presented earlier, the Type 1 carbon textile reinforcement has identical geometrical properties with 25.4 mm spacing between rovings in each direction. In addition to Type 1 reinforcement, two types of carbon textile reinforcements were created with the same mechanical properties as Type 1 textile reinforcement but having a varied spacing between rovings. Each textile reinforcement was embedded in a fine-grained concrete section with a constant thickness as a strengthening layer with 20 mm thickness same as in tests. Two types of steel bars were used in the specimens with different bar diameters. In Family#1,  $\phi 8$  steel bars were employed as in the tests, whereas  $\phi 6$  steel bars were used for the thinner specimens in Family#2. In both families, the spacings of the steel reinforcements were varied as 100 mm, 150 mm, and 200 mm.

With the intent of providing insight into the varied parameters pertaining to the specimens, the slabs were named according to their steel reinforcement and carbon textile spacing, and total height of the specimen. A typical specimen naming convention is displayed in Figure 6.1.

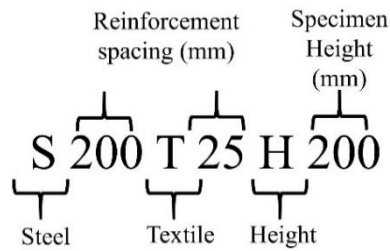


Figure 6.1. Naming conventions for fictitious specimens

### 6.1.1. Specimens in Family #1

As explained earlier, Family#1 consisted of nine 1.5 m square slab specimens with 0.22 m thickness in total, accounting for the strengthening layer (Figure 6.2). These specimens can be categorized into three main groups according to their steel reinforcement spacing. In these groups, the spacing of steel reinforcing bars were varied as 100 mm, 150 mm, and 200 mm, whereas the diameter of the steel bars remained unchanged and  $\phi 8$  steel bars were used in each specimen. In addition to steel bar spacing variation, each group consisted of specimens strengthened with carbon textile reinforcements with varying ratios. The employed carbon textile reinforcements in each group had different spacing between textile rovings. The spacings between rovings were changing as 12 mm, 16 mm, and 25 mm whereas the cross-sectional area of the rovings were the same,  $1.83 \text{ mm}^2$ . It should be reminded here that the employed carbon textile reinforcement had identical geometry in each direction as in the Type 1 carbon textile reinforcement used in the tests.

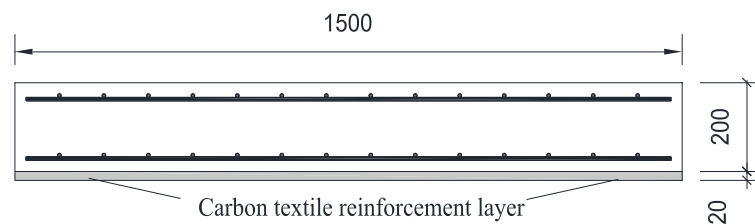


Figure 6.2. The cross-section of the specimens in Family#1

Family#1 was aimed to be an extension of the tested slab specimens. Therefore, all slab specimens in Family#1 were analyzed by using the same steel striker and the contact velocity employed in the tests. The kinetic energy of this striker is denoted as  $E_{\text{test}}$ . The members of Family#1 created for the analyses are tabulated in Table 6.1.

Table 6.1. Specimens in Family#1

Slab	Steel Rebar		Textile reinforcement		Height		Striker		Energy
	Rebar	Spacing (mm)	Spacing (mm)	$A_{roving}$ (mm <sup>2</sup> )	H (mm)	V (m/s)	d (mm)	m (kg)	
S100T12H220			12						
S100T16H220	Φ8	100	16	1.83	220	26	100	21.6	
S100T25H220			25						
S150T12H220			12						
S150T16H220	Φ8	150	16	1.83	220	26	100	21.6	$E_{test}$
S150T25H220			25						
S200T12H220			12						
S200T16H220	Φ8	200	16	1.83	220	26	100	21.6	
S200T25H220			25						

### 6.1.2. Specimens in Family #2

To investigate the performance of carbon textile reinforcement under low-velocity impacts, twenty-one slab specimens for Family#2 were designed to be thinner than the specimens in Family#1, intending to have a more flexural response at first the impacts. Similar to Family#1, all square specimens had a dimension of 1.5 m in x- and y- directions, whereas the total thickness was reduced to 0.08 m, including the strengthening layer (Figure 6.3). In this family, with the intent to minimize or prevent localized damage, the specimens were subjected to impact loads by means of a steel striker having lower velocity and higher mass compared to the previous family analyses and the test program. Also, the effect of the striker geometry was investigated by doubling the contact surface of the striker. Therefore, this family can be categorized into three main groups according to impact parameters. Similar to the previous family, each group consisted of the specimens having varied steel bar spacing as 100 mm, 150 mm, and 200 mm, whereas  $\phi 6$  steel reinforcing bars were used and kept unchanged for every specimen. Additionally, each group had a specimen that remained unstrengthened as a control specimen, unlike the previous family. These control specimens were created as identical as the other members in the family except for a strengthening layer of carbon textile reinforcements embedded in fine-grained concrete.

In the first group, the carbon textiles were varied as 10 mm and 30 mm. Through the combinations of the steel and carbon textile reinforcements, nine slab specimens

were created and subjected to the 146 kg of steel striker with 5 m/s velocity and 100 mm contact diameter until they were perforated.

In the following simulations of Family#2, the specimens were created with the same steel reinforcement variation, whereas only one type of carbon textile reinforcement was employed for the specimens in the second and third groups. Additionally, the specimens in these groups were subjected to impacts by means of a steel striker with a 200 mm contact diameter. In these FE analyses, the striker mass was kept same as in the first group as 146 kg, whereas the striker mass for the last group was doubled. The velocities of the strikers remained constant in the course of analyses and were assigned as 5 m/s. All the members of Family#2 are tabulated according to the impact parameters and their reinforcement types and presented in Table 6.2.

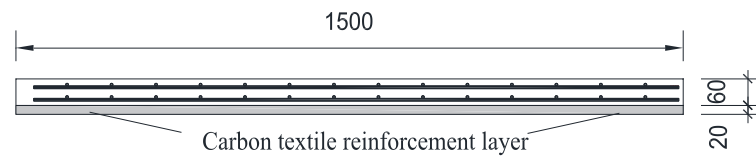


Figure 6.3. The cross-section of the specimens in Family#2

Table 6.2. Specimens in Family#2

Slab	Steel Rebar		Textile reinforcement		Height		Striker		Energy
	Rebar	Spacing (mm)	Spacing (mm)	$A_{roving}$ (mm <sup>2</sup> )	H (mm)	V (m/s)	d (mm)	m (kg)	
S100TnoH80			-						
S100T10H80	Φ6	100	10	1.83	80	5	100	146	
S100T30H80			30						
Group #1	S150TnoH80		-						
	S150T10H80	Φ6	150	10	1.83	80	100	146	0.25E <sub>test</sub>
	S150T30H80			30					
	S200TnoH80		-						
	S200T10H80	Φ6	200	10	1.83	80	100	146	
	S200T30H80			30					
Group #2	S100TnoH80	Φ6	100	-	1.83	80	200	146	
	S100T10H80			10					
	S150TnoH80			-					
	S150T10H80	Φ6	150	10	1.83	80	200	146	0.25E <sub>test</sub>
	S200TnoH80			-					
Group #3	S200T10H80	Φ6	200	10	1.83	80	200	146	
	S100TnoH80	Φ6	100	-	1.83	80	200	292	
	S100T10H80			10					
	S150TnoH80			-					
	S150T10H80	Φ6	150	10	1.83	80	200	292	0.50E <sub>test</sub>
S200TnoH80			-						
S200T10H80	Φ6	200	10	1.83	80	200	292		

### 6.1.3. Theoretical Static Capacities of Specimens

Understanding of mechanisms governed in RC sections during impact loadings is very important to identify impact parameters for design purposes. To reveal these mechanisms, experimental studies on impact behavior of RC members were carried out by several researchers and it is shown that the shear-failure mechanisms dominate the failure modes. For instance, punching shear failure modes were observed from experimental studies on RC slabs by Xiao et al. (2016). Also, Saatci and Vecchio (2009) presented the importance of shear mechanisms under impact loading even for the flexural-critical members. As mentioned in previous chapters, with the aim of revealing the efficiency of the carbon textile reinforcement and its contribution to the impact

behavior as a strengthening layer, the specimens without shear reinforcement were tested in the testing phase of this study. After carrying out the testing program, it is concluded that punching cone mechanisms were governed in the first impacts and the specimens with the carbon textile reinforcements were able to withstand the subsequent impacts and keep the structural integrity up to the excessive damage levels. In the light of literature, when the impact parameters of the tests such as the velocity of the striker and the striker diameter-to-specimen thickness ratio are considered, shear mechanisms are expected to be governed in the tests. In parallel to this expectation, the performance of the carbon textile reinforcements as a strengthening layer was aimed to be revealed in particular to the shear-deficient slabs. Furthermore, in the literature, relatively fewer studies examined and presented the impact performance of shear-deficient members (Nghiem & Kang, 2020). Therefore, in accordance with the specimens tested for this study, shear-critical slab members were created to investigate the performance of the carbon textile reinforcement under varied impact loadings. To do that, the theoretical flexural and punching capacities of each specimen were calculated for defining the critical failure mechanisms of these fictitious slab specimens.

The theoretical flexural and punching capacities were determined by using a simple code written in the MATLAB programming environment, taking the textile reinforcements into account as well. This code was also verified by using Response 2000 (Bentz & Collins, 2000) sectional analysis tool for theoretical flexural moment capacities of unstrengthened RC specimens. To determine the flexural moment capacity of RC members strengthened with textile reinforcements, simplified calculation methods were presented by Schladitz et al. (2012) and, these methods were taken into consideration while flexural moment capacities were calculated. After obtaining the ultimate sectional moment capacities of the slabs, the maximum flexural load capacities were calculated by applying yield line theory mechanisms for the specimens. The examined yield line patterns for each specimen are presented and tabulated in Appendix B.

With the intent to determine the punching shear capacities, four current design codes, Turkish (TS500-2000), American (ACI 318-19), European (EC2), and Canadian (CSA A23.3-04) standards were employed for each specimen in Family#1 and Family#2. All these design codes require basic geometrical properties of the sections and the mechanical properties of the materials used. One of the geometrical parameters used in the calculations is the effective depth of the section. Effective depth is defined

as the distance from the top fiber of the section to the bottom steel reinforcement center considered as bending reinforcement under static loading conditions. However, in presence of extra reinforcement as a strengthening layer such as textile reinforcement or glass fiber-reinforced polymer (GFRP) laminates, the effective depth should be calculated. To calculate the punching shear strength of slabs strengthened with GFRP laminates, Chen and Li (2005) performed an experimental study and proposed an analytical approach to obtain modified effective depth and reinforcement ratio to be used in design code expressions. According to this study, the equivalent effective depth,  $d_{eqv}$ , and the equivalent reinforcement ratio,  $\rho_{eqv}$ , can be obtained by using the distributions shown in Figure 6.4, and expressed as in Eq. (6.1 and Eq. (6.2).

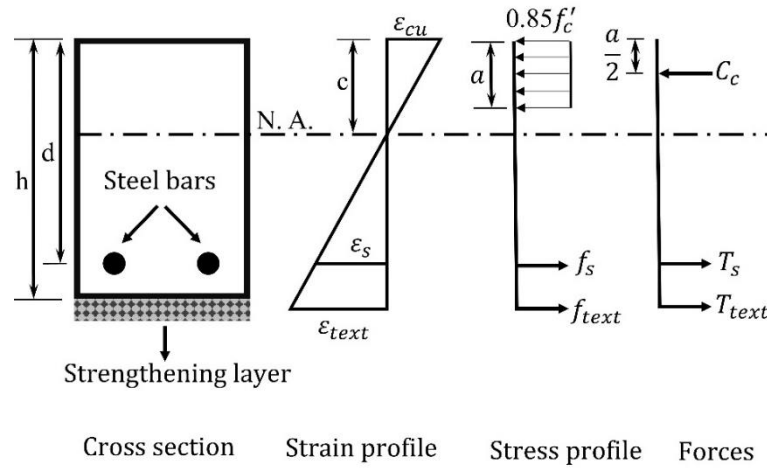


Figure 6.4. Strain, stress, and force distribution in section. (Redrawn from Chen and Li (2005), and modified for textile reinforcement)

$$d_{eqv} = \frac{M_{nf}}{T_s + T_f} + \frac{a}{2} \quad (6.1)$$

$$\rho_{eqv} = \frac{T_s + T_f}{bd_{eqv}f_s} \quad (6.2)$$

where;

$d_{eqv}$ : equivalent effective depth

$\rho_{eqv}$ : equivalent reinforcement ratio,

$M_{nf}$ : flexural strength including textile reinforcement effect

$T_s$ : tension force in steel reinforcement

$T_s$ : tension force in textile reinforcement

After obtaining the ultimate flexural capacities of the specimens for both families, a simple MATLAB code was also written for calculations of equivalent effective depth and reinforcement ratio by using the equations. When the equivalent effective depths and equivalent reinforcement ratios are obtained, the punching cone strength capacities were calculated by using each design code provision for the members in Family#1 and Family#2. The calculated capacities of each specimen are presented in Table 6.3 and Table 6.4 for each family. As it can be seen in Table 6.3, calculated punching capacities according to Eurocode2 are the highest among the code provisions for all specimens in Family#1. Therefore, punching capacities obtained from Eurocode2 were employed to determine the punching-to-flexural capacity ratios. According to these ratios, it is found that all members of Family#1 are shear-critical.

Table 6.3. The calculated capacities of the specimens in Family#1

Specimen	Moment capacity $M_u$ (kN.m)	Flexural capacity, $F_{flex}$ (kN)	Punching capacity, $V_r$ (kN)				$V_{r,EC2} /$ $F_{flex}$
			TS500	EC2	ACI	CSA	
S100T12H220	127	1016	383	532	361	415	0.5
S100T16H220	106	848	373	520	351	405	0.6
S100T25H220	84	672	354	460	334	385	0.7
S150T12H220	114	912	399	556	375	432	0.6
S150T16H220	92	736	388	512	366	422	0.7
S150T25H220	70	560	370	448	349	401	0.8
S200T12H220	108	829	405	548	382	439	0.7
S200T16H220	85	680	392	485	370	426	0.7
S200T25H220	63	504	382	447	361	415	0.9

Similar to Family#1, punching-to-flexural capacity ratios of the members in Family#2 were obtained by using Eurocode2. As it can be seen in Table 6.4, Eurocode2 estimated the lowest punching capacities for the unstrengthened members, whereas it estimated the highest punching capacities for the members strengthened with textile reinforcements. This can be explained as the contribution of reinforcements to punching capacity which is accounted by only Eurocode2 among the code provisions.

Table 6.4. The calculated capacities of the specimens in Family#2

Specimen	Moment capacity $M_u$ (kN.m)	Flexural capacity, $F_{flex}$ (kN)	Punching capacity, $V_r$ (kN)				$V_{r,EC2} /$ $F_{flex}$
			TS500	EC2	ACI	CSA	
S100TnoH80 <sup>†</sup>	10	78	71	67	67	77	0.9
S100T10H80	42	325	75	105	71	82	0.3
S150TnoH80 <sup>†</sup>	7	55	71	58	67	77	1.1
S150T10H80	36	272	78	101	74	85	0.4
S200TnoH80 <sup>†</sup>	5	42	71	53	67	77	1.3
S200T10H80	32	231	82	103	77	88	0.4

<sup>†</sup>Tno indicates the specimens without carbon textile reinforcement

## 6.2. Finite Element Modeling Results

As presented in Table 6.3 and Table 6.4 in the previous section, almost all the specimens in both families were shear-critical members which were expected to fail due to the shear mechanisms. However, as mentioned earlier, it is reported that shear-failure mechanisms were observed from the impact tests in the literature even if the members were flexural-critical (Saatci and Vecchio (2009)). Moreover, when the imparted impact load is considered, it is highly expected that as the impact velocity increases, the possibility of shear-failure mechanisms developing in member increase, as well as the possibility of localized damage. On the other hand, in the lower-velocity impact cases, members may collapse in a flexural-failure or mixed mode of flexural-shear failure (Kishi et al. (2002); Nghiem and Kang (2020)).

As mentioned earlier, one of the aims of the thesis presented herein is to reveal the contributions of the carbon textile reinforcement to the impact behavior of the slabs. To figure out the efficiency of carbon textile reinforcements under impacts, two types of specimen families were created and simulated under low-velocity and high-velocity impacts. According to the theoretical static capacities of the members in Family#1 and Family#2, all members were expected to fail due to the shear-failure mechanisms in the light of literature.

As a result of shear-failure mechanisms in RC members, punching cones or, in other words, shear plugs were observed around the impact vicinity from the impact tests in the literature and the tests presented in this thesis. When the shear-plug formation

developing in the course of impact is considered, it can be said that the key factor for defining the damage or failure is the deformation capacity. Therefore, to exhibit the effects of the carbon textile reinforcement on the impact behavior of the slabs, the midpoint displacement-time histories are presented and compared with each other consistent with the relevant parameters.

### **6.2.1. The Midpoint Displacements of the Specimens in Family#1**

As presented earlier in this chapter, Family#1 consisted of nine slab specimens with 220 mm total thickness, having varied steel and carbon textile reinforcements. All these specimens were subjected to consequent impacts by the same steel striker used in the tests until total perforation occurred. It should be also reminded here the S100T25H220 specimen was identical to the specimen named S3T1.

The midpoint displacement-time histories of the specimens were grouped according to their steel reinforcement ratios and presented in Figure 6.5 for the first impacts. It can be said that almost all specimens had a similar displacement response at the first impacts. As it can be seen from Figure 6.5a, the maximum midpoint displacements of the specimens with the highest steel reinforcement ratio had approximately the same for all, except for specimen S100T25H220 which had the lowest carbon textile reinforcement ratio, reaching a slightly higher value. In the post-impact phase, however, three specimens showed an identical response, resulting in the same residual displacements.

Similarly, the midpoint displacement-time histories of the specimens with 150 mm steel reinforcement spacing coincided with each other at the first impacts, independent of their carbon textile reinforcement ratios (Figure 6.5b). Additionally, these specimens could reach the maximum value as the S100 specimen series reached. However, the S150 series had lower recovery capacity that caused higher residual midpoint displacements.

The S200 specimen series which had the lowest steel reinforcement ratio suffered the most at the first impacts. As it can be seen from Figure 6.5c, these specimens had the highest peak midpoint displacements and the highest residual displacements among the other series of specimens. Nonetheless, when the displacement values are considered, it can be said that the differences in the midpoint

displacement responses of the specimens are very minor. Hence, it can be interpreted as neither the carbon textile reinforcements nor the steel reinforcements had significant effects on the displacement behavior of the specimens under the first impact of a 21.6 kg striker with the 26 m/s velocity.

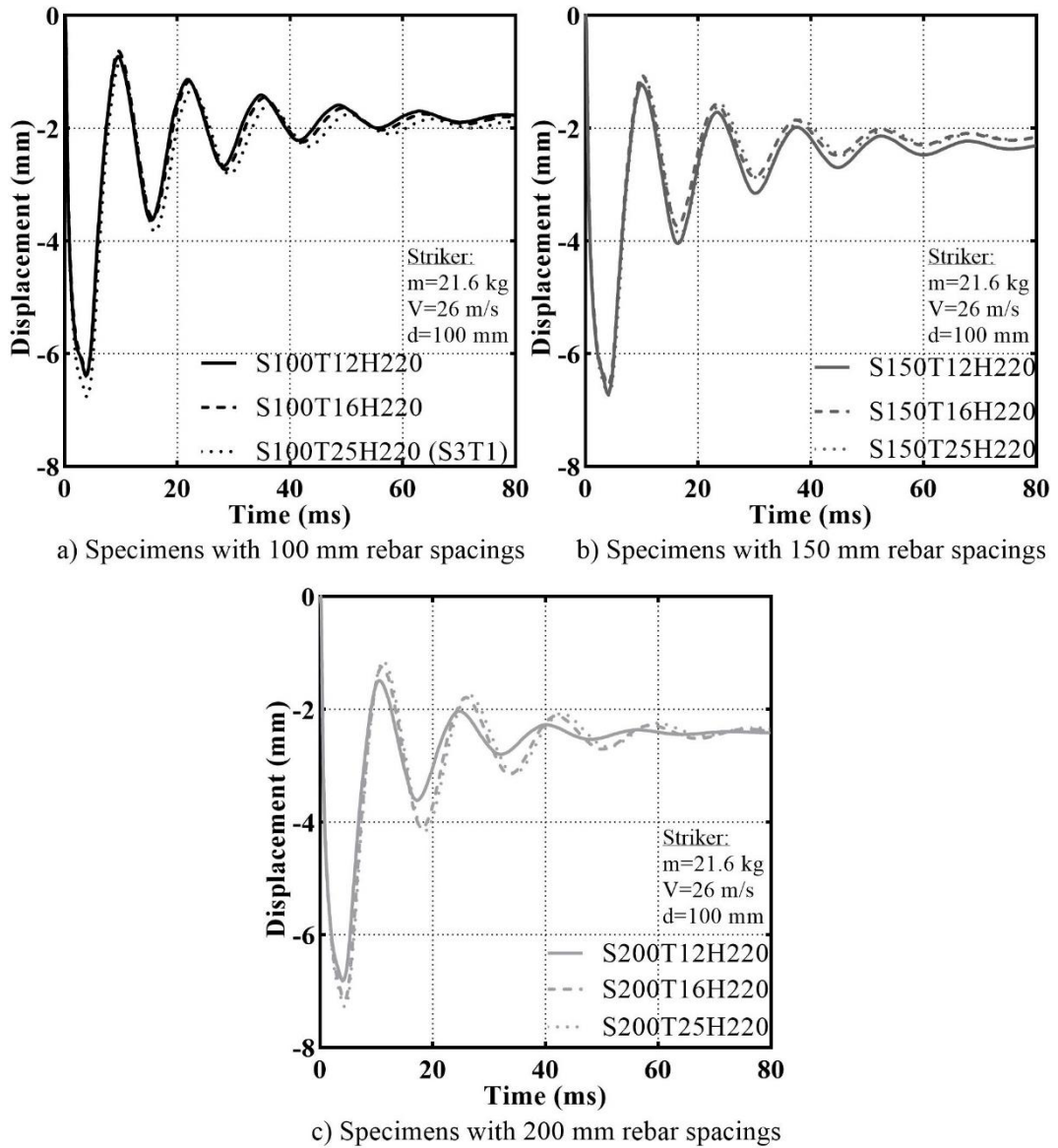


Figure 6.5. The midpoint displacement-time histories of specimens for the first impacts in Family#1

As previously mentioned, all the created specimens were simulated in the FE model until they were perforated by the striker. In the second impacts, the midpoint displacement responses of the specimens were quite similar as in the first impact responses. For this reason, the midpoint displacement-time histories of the specimens

pertaining to the second impacts are skipped, and third impact simulations are presented in Figure 6.6. As the damage inherited from the previous impacts increased, the displacement responses of the specimens differentiated. As it can be seen from Figure 6.6a, the effects of the carbon textile reinforcement ratio became prominent as limiting both peak and residual displacements. As expected, the specimen with the highest textile reinforcement showed the minimum peak and residual displacement at the third impact. However, other specimens, S100T16H220 and S100T25H220, had similar residual deformation in spite of their different carbon textile reinforcement ratios.

At the third impact analyses of the S150 series, the specimen with the highest carbon textile reinforcement ratio showed the minimum peak displacement and residual deformation, as expected (Figure 6.6b). Contrary to the specimens of the S100 series with 16 mm and 25 mm textile reinforcement spacing, the displacement-time histories of the S150T16H220 and S150T25H220 were quite similar, having approximately the same values as peak and residual displacements.

The specimens of the S200 series suffered enough from the third impact of the striker, and all the specimens belonging to this series were perforated, regardless of their carbon textile reinforcement ratio (Figure 6.6c). It should be also noted here that the rest of the members for the S100 and S150 series were perforated at the fourth impact simulations.

To show the effects of carbon textile and steel reinforcements on the impact behavior of the slab specimens, nine slab specimens were modeled and analyzed by using the impact parameters used in the testing phase of this study. As it can be concluded from these simulations, both of the reinforcements had not influential effects on the members for the first impact tests. However, in the subsequent impacts, the effects of steel and carbon textile reinforcements came into the picture. When the number of impacts that the specimens could withstand is considered, the specimens with the least steel reinforcement ratio failed earlier than the other specimens, regardless of their textile reinforcement ratio. It can be said that under these impact circumstances, employing a higher steel reinforcement ratio is advantageous over the carbon textile reinforcement employment, and the steel reinforcement ratio plays a determinant role in the displacement response of the slab specimen subjected to relatively higher impact loads.

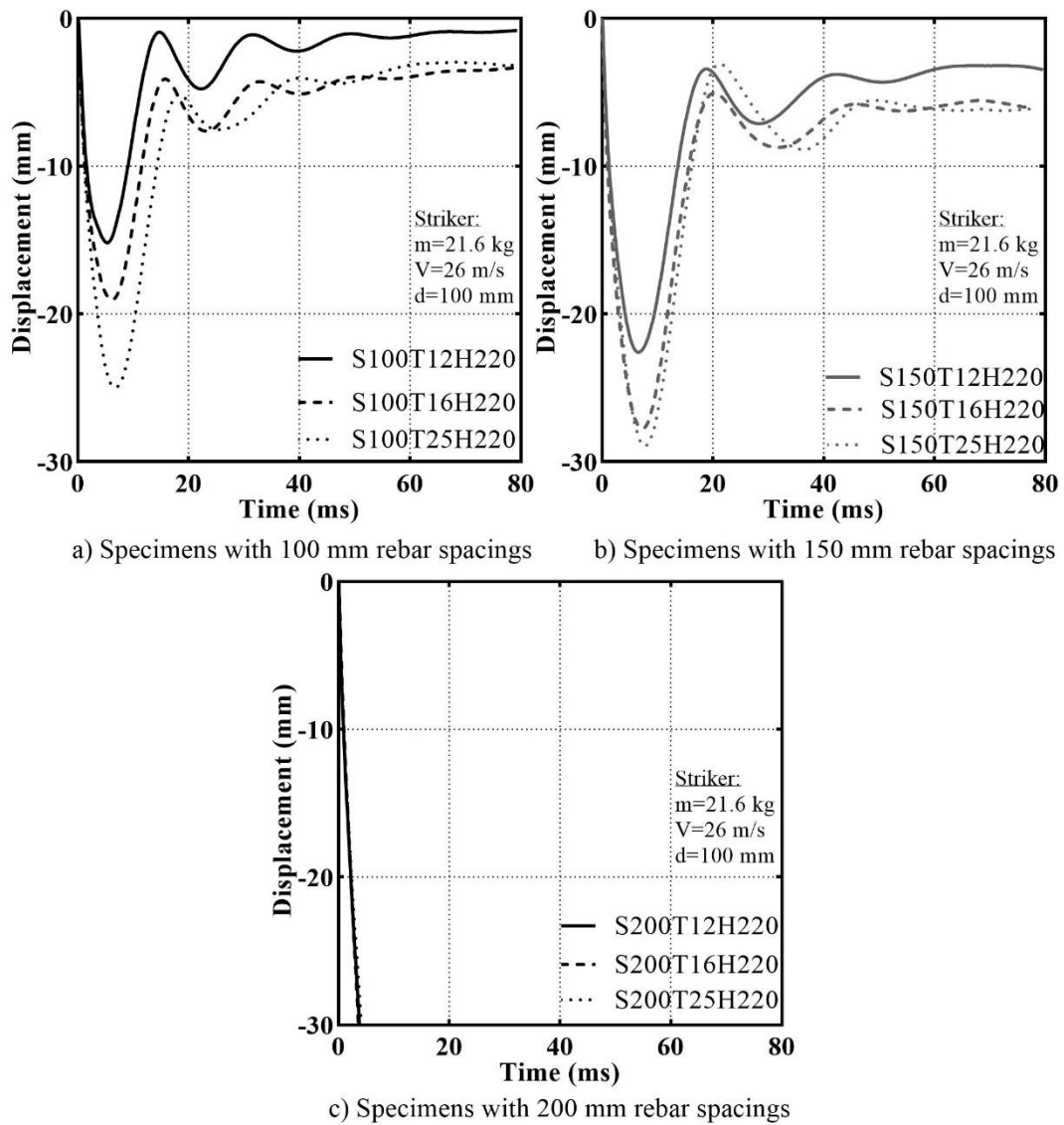


Figure 6.6. The midpoint displacement-time histories of specimens for the third impacts in Family#1

### 6.2.2. The Midpoint Displacements of the Specimens in Family#2

As presented previously in Table 6.2, twenty-one slab specimens with 80 mm total thickness were created for Family#2. As opposed to the specimens in the testing phase and analyses of Family#1 where the punching shear mechanism was dominating the overall behavior, the members of Family#2 were designed to be subjected to relatively low-velocity high-mass impact loads to reveal the contribution of the carbon textile reinforcements to the global response of the specimens. This family was divided into three groups according to the design of the striker parameters. The velocity of the striker was assigned as 5 m/s for all specimens in the family whereas the striker mass

and contact diameter were varied. Also, all the specimens in this family had the same steel reinforcement variation as the previous family, whereas the spacings of the textile reinforcements were changed. In Group#1, the spacings of textile reinforcements were assigned as 10 mm and 30 mm, whereas in Group#2 and Group#3, the textile reinforcements with 10 mm spacing were only used. Additionally, Family#2 possessed control specimens in each group that had no carbon textile reinforcement as a strengthening layer.

### **6.2.2.1. The Midpoint Displacements of the Specimens in Group#1**

The midpoint displacement-time histories are depicted in Figure 6.7 for the first impacts of the specimens in Group#1. The members of this group were analyzed under impact loads by means of a 146 kg striker with 5 m/s contact velocity and 100 mm contact diameter, as explained before. Similar to the previous family, the displacement responses of the members were categorized according to the steel reinforcement spacings. The displacement-time histories of the members with the highest steel reinforcement ratio are displayed in Figure 6.7a. The member with the highest textile reinforcement ratio exhibited the lower peak and residual displacements as expected. However, unexpectedly, the specimen with a lower carbon textile reinforcement amount, S100T30H80, showed a higher value at the peak compared to the specimen S100TnoH80 which had no textile reinforcement. Yet, S100T30H80 specimen showed higher recovery capacity and resulted in lower residual displacement.

Similar to the specimens of the S100 series, the displacement-time histories for the specimens of the S150 and S200 series exhibited similar during the impacts. As it can be seen from Figure 6.7b and Figure 6.7c, the specimens with the highest textile reinforcement ratio showed the lowest peak and residual displacements. Again, the specimens with the 30 mm textile reinforcements showed approximately the same peak values as the specimens without textiles. However, the textile reinforcements were able to decrease the residual displacements compared to the ones without textiles.

After employing all specimens under the same impact loads, the peak and residual displacements of the slabs were lower in the presence of textile reinforcement. However, the textile reinforcement amount has a more influential role in limiting the peaks in the course of impacts. As a consequence of these analyses for the first impacts,

it can be interpreted that the textile reinforcements can be an alternative or substitution for steel reinforcements. For instance, when the displacement profiles of the S100TnoH80 and S200T10H80 respectively shown in Figure 6.7a and Figure 6.7c are compared, it can be said that the residual displacements are approximately the same, and the peak values are quite close.

Similar to the specimens in Family#1, all slabs were analyzed until total perforation occurred. It should be noted here the specimens for S100 and S150 series could resist two subsequent impacts, and perforation occurred at the third impacts. However, due to the excessive damage, element deletion in other words, in the punching cone area, the displacement responses are not presentable. Additionally, it should be noted here the S200 series was perforated at the second impact.

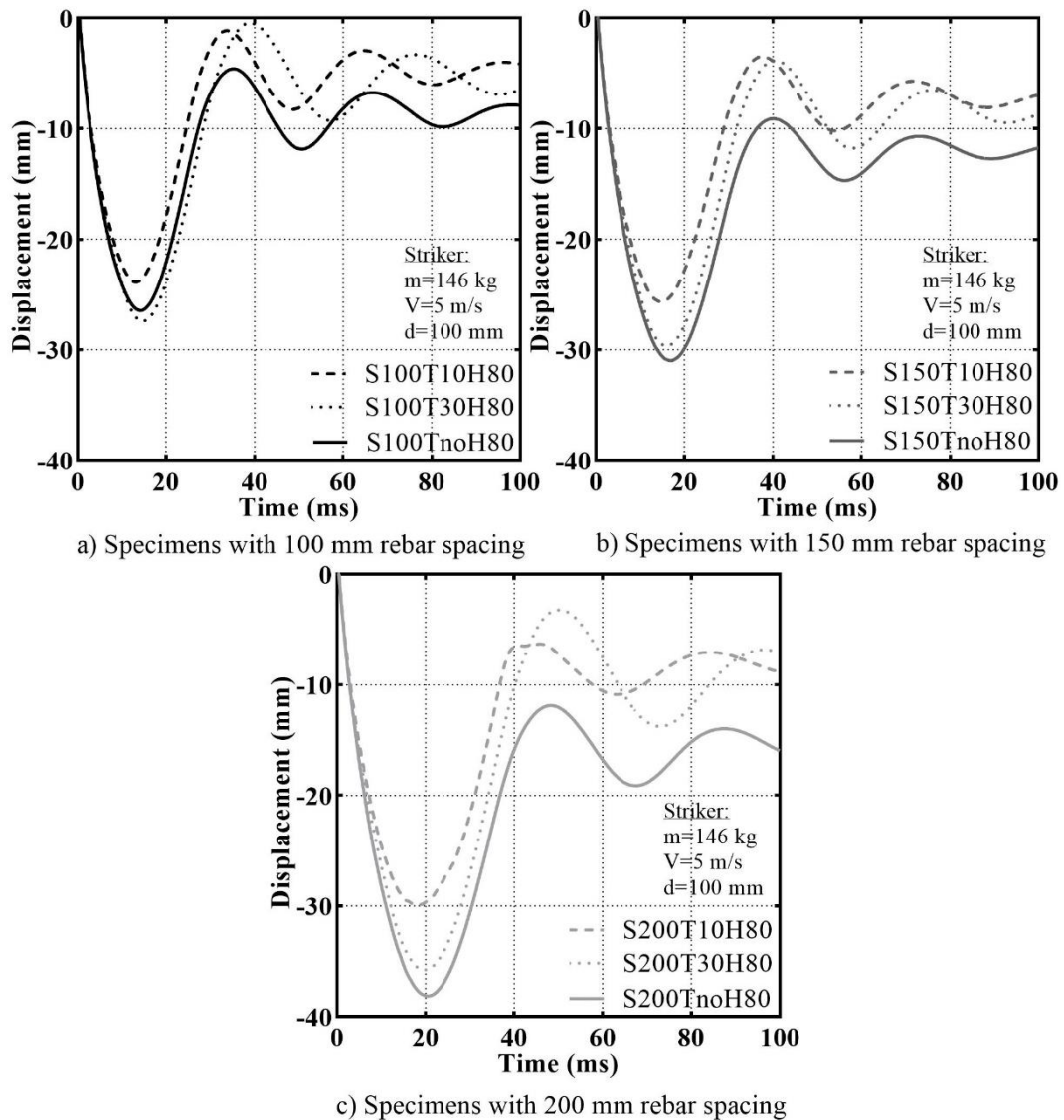


Figure 6.7. The midpoint displacement-time histories of specimens for the first impacts in Group#1

### 6.2.2.2. The Midpoint Displacements of the Specimens in Group#2

In the following analyses of Family#2, the specimens in Group#2 were subjected to the striker with the same mass and velocity as in the previous group, whereas the striker diameter was increased from 100 millimeters to 200 millimeters. Additionally, only one type of textile reinforcement was selected as 10 mm and employed in the specimens. The displacement-time histories of the specimens of the S100, S150, and S200 series are displayed in Figure 6.8 for the first impact analyses.

As it is clearly seen from Figure 6.8a to Figure 6.8c, the specimens with the textile reinforcements showed lower peak and residual displacements for all series of

S100, S150, and S200, shown respectively. Also, similar to the previous group, the difference in the displacements between the specimens with and without textile reinforcements are increasing with the increase of the steel reinforcing bar spacing.

Up to the analyses of the Group#1, the striker contact diameter employed in the tests and analyses were selected as 100 mm and the striker diameter-to specimen ratio was relatively lower. Considering the previous analyses, it can be said that the specimens in the series of S100 and S150 showed similar or close predictions in regards to the peak and residual displacements. Distinctly from the previous analyses, the specimen with the textile reinforcements in the S150 and S200 series had similar displacement-time histories which had close residual deformations to the specimen in the S100 series. It can be interpreted as the carbon textile reinforcements were able to perform better for overall response under impacts, and they were capable of compensating the steel reinforcement deficiency regarding residual deformations.

In the analyses of Group#2, the striker diameter was doubled to obtain more global responses of slabs compared to the responses obtained from the impacts with the smaller diameter. In other words, the localized damage effects were aimed to be minimized or prevented by increasing the striker diameter-to-slab thickness ratio. As purposed, the specimens subjected to the same impact loads with the doubled contact surface area responded more globally, and the local damages were not observed up to the eighth impact analyses. It is observed that these specimens could have resisted even more than that. Due to the high durations until the eighth analyses, the further impacts were considered unnecessary, they were terminated after the eighth impact. It also should be noted here that the effects of the carbon textile reinforcements on the midpoint displacement responses were similar to the first impact responses. Therefore, the subsequent impacts after the first ones are not presented herein in an effort to avoid redundancy.

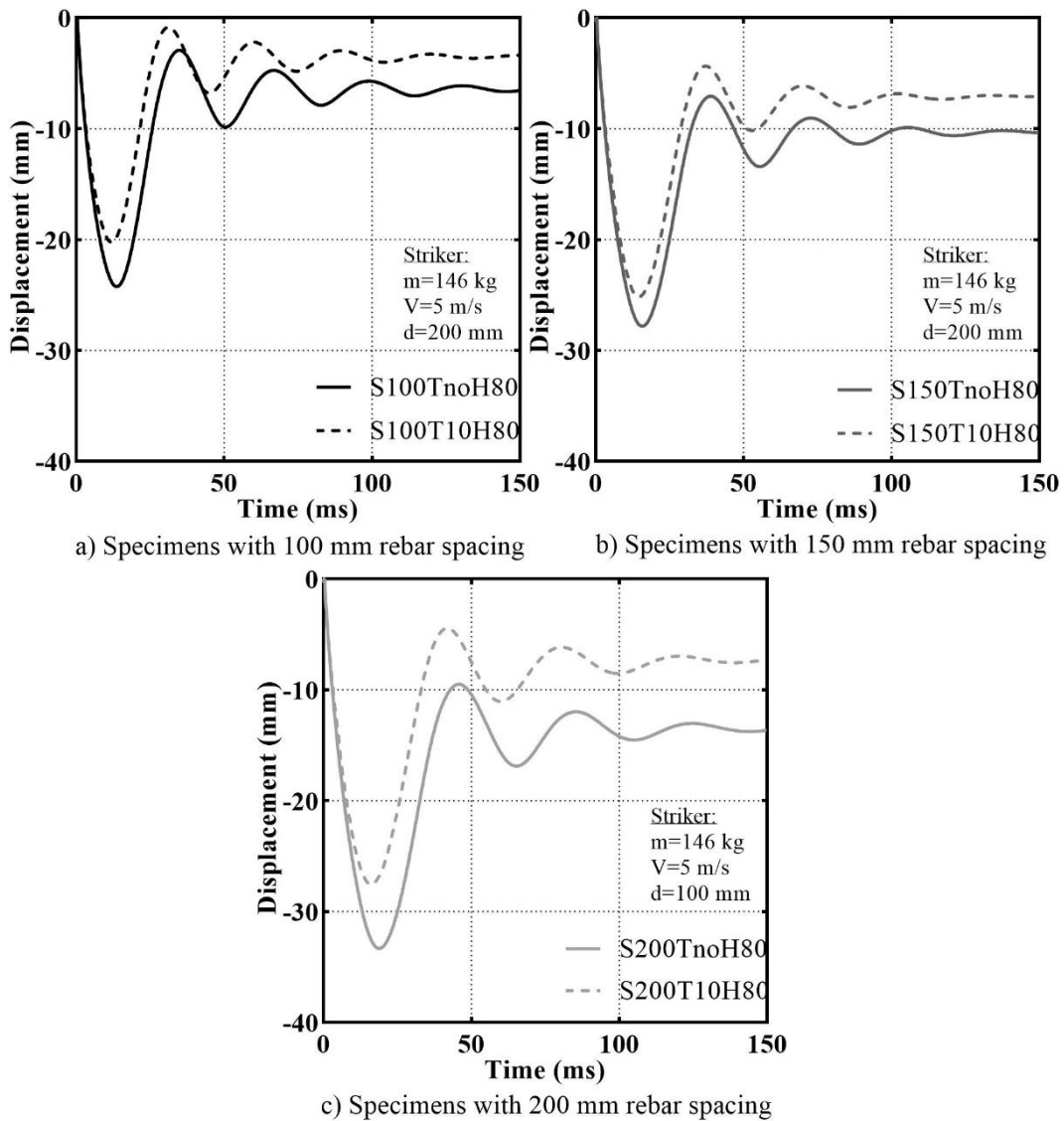


Figure 6.8. The midpoint displacement-time histories of specimens for the first impacts in Group#2

### 6.2.2.3. The Midpoint Displacements of the Specimens in Group#3

The same specimens analyzed in the previous group were employed for Group#3 as the next and final destination of this parametric study. In the analyses of these groups, similar to previous analyses, the specimen series of S100, S150, and S200 with and without carbon textile reinforcement were subjected to the striker with the same velocity and contact diameter but the increased mass. In these analyses, the mass of the striker was doubled from 146 kilograms to 292 kilograms in an effort to observe again the overall response of the specimens under impacts, yet to reach failure in a few analyses. Thanks to the increased striker mass, the specimen series of S100 and S150

were perforated at the third impacts, whereas the specimens for the S200 series could not resist the second impacts. Due to the excessive damage and element deletion around the midpoint vicinity, the second impacts for the S100 and S150 series cannot be presented. The displacement responses of the employed specimens for the first impacts can be seen in Figure 6.9.

As it can be clearly seen in Figure 6.9, similar to the previous analyses, the best performance was given by the specimen with the highest steel and textile reinforcement ratio, as expected. Until here, in all analyses of this parametric study, the textile reinforcements were able to limit the peak displacement in the responses, regardless of the textile reinforcement spacing, or in other words, the textile reinforcement ratio. However, in the analyses of Group#3, the specimens with and without textile reinforcements reached the same peaks in S100 and S150 series. It can be interpreted as the presence of the textile reinforcement did not affect limiting peak displacements under prescribed impact conditions when the specimens had steel reinforcement ratios at certain levels. At the same time, the textiles had a major influence on the residual deformations for both specimen series of S100 and S150 (Figure 6.9a and Figure 6.9b). This influence on the residual deformations became more prominent in the analyses of S200 series. The difference in residual deformations between the S200 specimens increased compared to the other specimen series in the case of containing lower steel reinforcement ratios (Figure 6.9c).

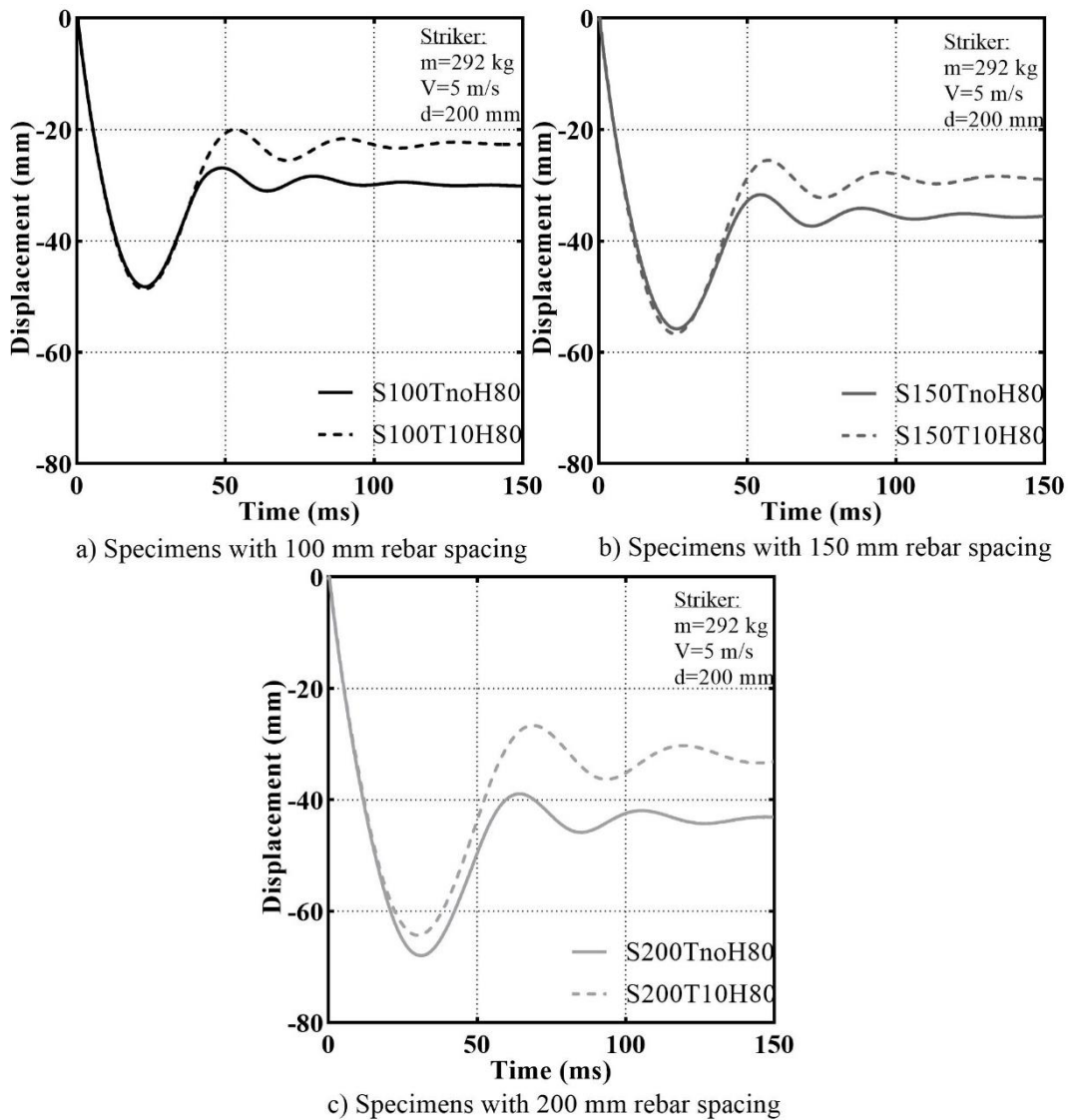


Figure 6.9. The midpoint displacement-time histories of specimens for the first impacts in Group#3

### 6.3. Summary of the Parametric Investigations

As mentioned earlier, the main goal of this parametric study is to investigate the influence of the textile reinforcements on the displacement response and the efficient employment under the different impact conditions and parameters. To reach this goal, the FE model presented in the previous chapter was employed for these fictitious specimens. To define the failure criteria of the specimens, theoretical shear and flexural capacities were calculated and examined, taking the textile reinforcements into accounts as well. As presented earlier, most of these specimens were designed as shear-critical members and expected to be failed due to the shear mechanisms. Additionally, in the

light of literature, it can be stated as the shear mechanisms are dominant in the course of impact loading, even for flexural-critical members. When this phenomenon is considered during impacts, the textile reinforcements may have a considerable role in the impact behavior of shear-deficient members. Therefore, starting from the impact parameters used in the testing program of this thesis, different factors and parameters were examined with the help of FE simulations. As a result of the analyses, the displacement responses of the specimens that can be accepted as the key factor for defining the failure are presented. Based upon the predicted midpoint displacement responses from these FE analyses, the following conclusions are drawn:

- i. The specimens subjected to the relatively high-velocity low-mass impacts had very similar responses in the first impacts, regardless of the carbon textile and steel reinforcement ratios. However, in the following impacts, the employment of a higher steel reinforcement ratio was advantageous over the carbon textile reinforcement when the total imparted impact energy is considered. The textile reinforcement was not able to compensate for the steel reinforcement deficiency under the prescribed impact parameters,
- ii. Under high-mass low-velocity conditions, carbon textile reinforcements were able to limit peak displacements during the impacts, and more importantly, they were very effective for limiting the residual deformations. It can be said that, in some cases, the carbon textile reinforcements may be used instead of steel reinforcement as a substitution or compensation,
- iii. It is observed from the analyses that the striker diameter-to-member thickness ratio had a significant effect on the member response under impacts. The specimens were able to resist higher impact energies by increasing the striker diameter-to-member thickness ratio. For the sake of a higher diameter-to-thickness ratio, more global behavior observed from the analyses,
- iv. In parallel with the increase in global responses of the specimens, the textile reinforcement efficiency increased in regards to the limitation on the residual deformations, and the specimens could resist higher impact energies generated by the striker with the same velocity but higher mass.

## CHAPTER 7

### CONCLUSIONS AND RECOMMENDATIONS

The main objective of this thesis was to uncover the performance of the carbon textile reinforcement used for an additional strengthening layer of RC slab members subjected to impact loads. To do that, the study presented herein was planned to accomplish multi-directional missions, and these missions were collected under the head titles of the experimental and finite element investigations, principally. Therefore, for the sake of clarity, the conclusions and recommendations are presented separately for the experimental and numerical investigations.

#### 7.1. Conclusions

As explained in the first chapter of the thesis, textile reinforced concrete (TRC) elements have been employed by researchers to enhance the capacities of RC members under static or cyclic loading conditions for retrofitting and/or strengthening purposes. However, in the literature, the behavior of RC members strengthened with the mesh-form TRC elements under high-rate loadings is barely investigated or explained. Therefore, with the intent to fill this gap, a well-instrumented experimental program was designed to supply detailed data sets not only for the understanding of impact behavior but also for implementing the benchmarking FE investigations.

A total of 14 impact tests were carried out by employing two unstrengthened and two strengthened specimens with TRC elements with the help of an advanced testing facility. In the light of collected data and observations made from these tests, the following conclusions can be drawn:

- i. The crack formations developed after the first impacts were a combination of radial cracks around impact vicinity and linear cracks on the diagonals and middle axes for each specimen, regardless of the carbon textile reinforcement entity. However, the strengthened specimens had more continuous crack formation compared to the unstrengthened specimens. Also, narrower cracks developed in the

strengthened specimens. With the increase of carbon textile reinforcement ratio, the width of cracks decreased whereas the number of cracks increased and they were more distributed. Therefore, it can be said that the use of carbon textile reinforcement leads to better crack control in RC slabs subjected to impact loads,

- ii. Even though the unstrengthened specimens were tested with varied impact loads, the measured reactions were very similar in the first impact tests. In subsequent impacts, due to the inherited damage, the transmission of impact forces to the supports was differentiated for unstrengthened specimens. However, the measured reactions after the first impacts of strengthened specimens were close to each other until excessive damage occurred around the impact vicinity. The TRC layers were successful to transmit the impact loads after the first impacts until excessive damage occurs in the specimens,
- iii. Increasing the carbon textile reinforcement ratio had highly influential effects on limiting the peak displacement and residual deformation, as well as the penetration depth and concrete scabbing. In parallel with the increase of the carbon textile reinforcement ratio, the number of impacts resisted by the specimens increased,
- iv. Until total perforation of the strengthened slab specimens, an apparent bulging was observed around the punching cone region, and the specimens failed due to perforation of the carbon textile reinforcements. In parallel with damage levels in the punching cone, debonding of strengthening layers was observed. However, beyond the punching cone region, a malfunction of strengthening layers due to the bonding problems was not observed and these layers were successful to transmit impact loads to the supports up to certain damage levels.

In the following steps of the thesis, numerical investigations were conducted by using the LS-DYNA FE tool. Two models, one with a coarse mesh and one with a finer mesh, were created. To verify the employed FE models, the data collected from the tests series were used employed for benchmarking analyses, and then, a parametric study was performed with aim of figuring out the parameters for efficient employment of the

carbon textile reinforcements under impact loads. The following conclusions were made after these investigations:

- i. Both investigated FE models were mesh-dependent. The selection of element size and erosion criteria had considerable effects on the member response under impacts. On the other hand, although somewhat less accurate than the finer one, coarser mesh was found to be sufficiently accurate. Considering the significantly longer computation time required in finer mesh, the coarser mesh was found to be a more reasonable choice for further investigations,
- ii. The created FE models were able to perform well regarding the predicted midpoint displacement response, total reaction response, and damage patterns in the first impacts. However, the degree of accuracy decreased with the increase of damage levels in the subsequent impacts,
- iii. As a result of parametric investigations, in the high velocity-low mass impact events, the response of the slabs was not sensitive to the reinforcements' ratio in the first impacts. The employment of higher steel reinforcement is advantageous over the carbon textile reinforcements for the subsequent impacts,
- iv. The carbon textile reinforcements showed better performance under low-velocity high-mass impact events in regards to limit peak displacements and residual deformations,
- v. The striker diameter-to-member thickness ratio had a very influential effect on the response type of the member. With the increase of this ratio, the member responded more globally, and it is observed that the carbon textile reinforcements performed better in parallel with the increase in the global response.

## **7.2. Recommendations for Future Studies**

Throughout investigations for the thesis presented herein, some deficiencies and limitations were detected. It is believed that identification of the drawbacks is beneficial

for further investigations to overcome possible problems in advance. To provide information for future studies, the following recommendations were made:

- i. As presented in Chapter 5, the capacity of the accelerometers located in the midpoint of the back face of the specimens could not capture the peak accelerations due to their inadequate capacity. The increase in the capacity, as well as the number of accelerometers employed in the tests, would be very beneficial to reveal the inertial responses throughout impact tests,
- ii. The contactless sensors are very useful to capture data with higher frequencies. However, due to the cracking or scabbing of concrete, a problematic signal occurred during the impacts. This type of signaling issue should be double-checked before testing to prevent data loss. For this purpose, high-speed camera footages were significantly helpful to ensure data reliability,
- iii. In the finite element investigations, only one type of concrete material model was employed and presented in this study because of the stability problems caused by other concrete models. Putting more effort into other material models would increase the accuracy of response,
- iv. Implementing a comprehensive impact test program is no easy task due to the vast number of combinations and possibilities of the impact parameters. Yet, experimental data would be very supportive for the extended parametric investigations.

## REFERENCES

- ACICommittee318. (2019). Building Code Requirements for Structural Concrete (ACI 318-19) and Commentary (ACI318R-19). In. Farmington Hills, MI.
- ACICommittee549. (2013). Guide to Design and Construction of Externally Bonded Fabric Reinforced Cementitious Matrix (FRCM) Systems for Repair and Strengthening Concrete and Masonry Structures (ACI 549.4R-13). In. Farmington Hills, MI.
- Al-Salloum, Y. A., Siddiqui, N. A., Elsanadedy, H. M., Abadel, A. A., & Aqel, M. A. (2011). Textile-Reinforced Mortar versus FRP as Strengthening Material for Seismically Deficient RC Beam-Column Joints. *Journal of Composites for Construction*, 15(6), 920-933. doi:10.1061/(Asce)Cc.1943-5614.0000222
- Alkloub, A. A. K. (2015). *Behavior of Reinforced Concrete Panels Subject to Impact by Non-deformable Projectiles*. (Doctoral Dissertation), Purdue University, West Lafayette, IN.
- Alonso, G. (2013). *Experimental and Numerical Analysis of Reinforced Concrete Elements Subjected to Blast Loading*. (Doctoral Dissertation), Universidad Politécnica de Madrid, Madrid, Spain.
- Arsan, Y. (2014). *Effects of Shear Reinforcement on the Impact Behavior of Reinforced Concrete Slabs*. (Master's Thesis), Izmir Institute of Technology, Izmir, Turkey.
- ASTM. (2002). C 348: Standard Test Method for Flexural Strength of Hydraulic-Cement Mortars. In. West Conshohocken, PA.
- ASTM. (2008). C109/C 109M: Standard Test Method for Compressive Strength of Hydraulic Cement Mortars. In. West Conshohocken, PA.
- Batarlar, B. (2013). *Behavior of Reinforced Concrete Slabs Subjected to Impact Loads*. (Master's Thesis), Izmir Institute of Technology, Izmir, Turkey.
- Batarlar, B., Hering, M., Bracklow, F., Kühn, T., Beckmann, B., & Curbach, M. (2020). Experimental investigation on reinforced concrete slabs strengthened with carbon textiles under repeated impact loads. *Structural Concrete*. doi:10.1002/suco.201900319
- Beckmann, B., Frenzel, M., Lorenz, E., Schladitz, F., & Rempel, S. (2015). Flexural Behaviour of textile reinforced concrete Slabs. *Beton- Und Stahlbetonbau*, 110, 47-53. doi:10.1002/best.201400117

- Beckmann, B., Hummeltenberg, A., Weber, T., & Curbach, M. (2012). Strain Behaviour of Concrete Slabs under Impact Load. *Structural Engineering International*, 22(4), 562-568. doi:10.2749/101686612x13363929517893
- Bentz, E. C., & Collins, M. P. (2000). Response 2000 [Computer Software].
- Broadhouse, B. J. (1995). The Winfrith Concrete Model in LS-DYNA3D. Report No. SPD/D (95) 363. Atomic Energy Authority, Winfrith Technology Centre, Dorset, UK.
- Broadhouse, B. J., & Attwood, G. J. (1993). *Finite element analysis of the impact response of reinforced concrete structures using DYNA3D*. Paper presented at the Transactions of the 12. international conference on Structural Mechanics in Reactor Technology (SMiRT), Stuttgart, Germany.
- Bruckner, A., Ortlepp, R., & Curbach, M. (2006). Textile reinforced concrete for strengthening in bending and shear. *Materials and Structures*, 39(8), 741-748. doi:10.1617/s11527-005-9027-2
- Canadian Standard Association. (2014). Design of Concrete Structures (CSA A23. 3-14). In *CSA Group*. Mississauga, Canada.
- CEB. (1988). Concrete Structures under Impact and Impulsive Loading. In *Synthesis report: Comite Euro-International Du Beton*.
- Changiz Rezaei, S. H. (2011). *Response of reinforced concrete elements to high-velocity impact load* (Doctoral Dissertation), Purdue University, West Lafayette, IN.
- Chen, C. C., & Li, C. Y. (2005). Punching shear strength of reinforced concrete slabs strengthened with glass fiber-reinforced, polymer laminates. *Aci Structural Journal*, 102(4), 535-542.
- Chen, Y., & May, I. M. (2009). Reinforced concrete members under drop-weight impacts. *Proceedings of the Institution of Civil Engineers-Structures and Buildings*, 162(1), 45-56. doi:10.1680/stbu.2009.162.1.45
- Dancygier, A. N., & Yankelevsky, D. Z. (1996). High strength concrete response to hard projectile impact. *International Journal of Impact Engineering*, 18(6), 583-599. doi:10.1016/0734-743x(95)00063-G
- Dassault Systèmes. (2017). ABAQUS [Computer Software]. Waltham, MA.
- Deutsches Institut für Normung. (2009). DIN 488-1:2009 Reinforcing Steels-Part1:Grades, Properties, Marking. In Berlin, Germany.

- Dinic, G., & Perry, S. H. (1990). Shear Plug Formation in Concrete Slabs Subjected to Hard Impact. *Engineering Fracture Mechanics*, 35(1-3), 343-350. doi:10.1016/0013-7944(90)90213-Z
- EN1992-1-1. (2004). Eurocode2: Design of concrete structures-Part 1-1: General rules and rules for buildings. In Brussels, Belgium.
- Hering, M., Bracklow, F., Kuhn, T., & Curbach, M. (2020). Impact experiments with reinforced concrete plates of different thicknesses. *Structural Concrete*, 21(2), 587-598. doi:10.1002/suco.201900195
- Hering, M., Bracklow, F., Scheerer, S., & Curbach, M. (2020). Reinforced Concrete Plates under Impact Load-Damage Quantification. *Materials*, 13(20). doi:10.3390/ma13204554
- Holmquist, T. J., Johnson, G. R., & Cook, W. H. (1993). *A computational constitutive model for concrete subjected to large strains, high strain rates, and high pressures*. Paper presented at the Proceedings of the Fourteenth International Symposium on Ballistics, Quebec City, Canada.
- Hrynyk, D. (2013). *Behaviour and Modelling of Reinforced Concrete Slabs and Shells under Static and Dynamic Loads*. (Doctoral Dissertation), University of Toronto, Toronto, Canada.
- Hrynyk, T. D., & Vecchio, F. J. (2014). Behavior of Steel Fiber-Reinforced Concrete Slabs under Impact Load. *Aci Structural Journal*, 111(5), 1213-1223.
- ICC Evaluation Service. (2011). Acceptance Criteria for Masonary and Concrete Strengthening Using Fiber-Reinforced Cementitious Matrix (FRCM) Composite Systems (AC434). In *A Subsidiary of the International Code Council*.
- Kishi, N., Komuro, M., Kawarai, T., & Mikami, H. (2020). Low-Velocity Impact Load Testing of RC Beams Strengthened in Flexure with Bonded FRP Sheets. *Journal of Composites for Construction*, 24(5). doi:10.1061/(Asce)Cc.1943-5614.0001048
- Kishi, N., Mikami, H., Matsuoka, K. G., & Ando, T. (2002). Impact behavior of shear-failure-type RC beams without shear rebar. *International Journal of Impact Engineering*, 27(9), 955-968. doi:10.1016/S0734-743x(01)00149-X
- Koutas, L. N., Tetta, Z., Bournas, D. A., & Triantafillou, T. C. (2019). Strengthening of Concrete Structures with Textile Reinforced Mortars: State-of-the-Art Review. *Journal of Composites for Construction*, 23(1). doi:10.1061/(Asce)Cc.1943-5614.0000882
- Kühn, T., & Curbach, M. (2015). *Behavior of RC-slabs under impact-loading*. Paper presented at the DYMAT 2015 - 11th International Conference on the Mechanical and Physical Behaviour of Materials under Dynamic Loading.

- Livermore Software Technology Corporation. (2006). LS-DYNA. In *Theory Manual*. Livermore, CA.
- Livermore Software Technology Corporation. (2019). LS-DYNA [Computer Software]. Livermore, CA.
- Livermore Software Technology Corporation. (2020). LS-DYNA. In *Keyword User's Manual* (Vol. Volume I-II). Livermore, CA.
- Luccioni, B., Aráoz, G. F., & Labanda, N. A. (2013). Defining erosion limit for concrete. *International Journal of Protective Structures*, 4(3), 315-340.
- Malvar, L. J., Crawford, J. E., Wesevich, J. W., & Simons, D. (1997). A plasticity concrete material model for DYNA3D. *International Journal of Impact Engineering*, 19(9-10), 847-873. doi:Doi 10.1016/S0734-743x(97)00023-7
- Mathworks Inc. (2018). MATLAB [Computer Software]. Natick, MA.
- Mougin, J. P., Perrotin, P., Mommessin, M., Tonnelo, J., & Agbossou, A. (2005). Rock fall impact on reinforced concrete slab: an experimental approach. *International Journal of Impact Engineering*, 31(2), 169-183. doi:10.1016/j.ijimpeng.2003.11.005
- Nagendra Babu, S. (2016). *Numerical Erosion in Continuum Damage Mechanics* (Master's Thesis), TU Delft, Delft, Netherlands.
- Nghiem, A., & Kang, T. H. K. (2020). Drop-Weight Testing on Concrete Beams and ACI Design Equations for Maximum and Residual Deflections under Low-Velocity Impact. *Aci Structural Journal*, 117(2), 199-210. doi:10.14359/51721316
- Othman, H., & Marzouk, H. (2016). Impact Response of Ultra-High-Performance Reinforced Concrete Plates. *Aci Structural Journal*, 113(6), 1325-1334. doi:10.14359/51689157
- Othman, H., & Marzouk, H. (2017). Finite-Element Analysis of Reinforced Concrete Plates Subjected to Repeated Impact Loads. *Journal of Structural Engineering*, 143(9). doi:10.1061/(Asce)St.1943-541x.0001852
- Ottosen, N. S. (1977). Failure Criterion for Concrete. *Journal of the Engineering Mechanics Division-Asce*, 103(4), 527-535.
- Saatci, S. (2006). *Behaviour and Modelling of Reinforced concrete Structures Subjected to Impact Loads*. (Doctoral Dissertation), University of Toronto, Toronto, Canada.
- Saatci, S., & Vecchio, F. J. (2009). Effects of Shear Mechanisms on Impact Behavior of Reinforced Concrete Beams. *Aci Structural Journal*, 106(1), 78-86.

- Sangi, A. J. (2011). *Reinforced Concrete Structures under Impact Loads*. (Doctoral Dissertation), Heriot-Watt University, Edinburgh, Scotland.
- Schladitz, F., Frenzel, M., Ehlig, D., & Curbach, M. (2012). Bending load capacity of reinforced concrete slabs strengthened with textile reinforced concrete. *Engineering Structures*, *40*, 317-326. doi:10.1016/j.engstruct.2012.02.029
- Schutze, E., Bielak, J., Scheerer, S., Hegger, J., & Curbach, M. (2018). Uniaxial tensile test for carbon reinforced concrete with textile reinforcement. *Beton- Und Stahlbetonbau*, *113*(1), 33-47. doi:10.1002/best.201700074
- Schwer, L. (2014). *Modeling rebar: The forgotten sister in reinforced concrete modeling*. Paper presented at the 13th International LS-DYNA® Users Conference.
- Soltani, H., Khaloo, A., & Sadraie, H. (2020). Dynamic performance enhancement of RC slabs by steel fibers vs. externally bonded GFRP sheets under impact loading. *Engineering Structures*, *213*. doi:10.1016/j.engstruct.2020.110539
- Tai, Y. S. (2009). Flat ended projectile penetrating ultra-high strength concrete plate target. *Theoretical and Applied Fracture Mechanics*, *51*(2), 117-128. doi:10.1016/j.tafmec.2009.04.005
- Thai, D. K., & Kim, S. E. (2014). Failure analysis of reinforced concrete walls under impact loading using the finite element approach. *Engineering Failure Analysis*, *45*, 252-277. doi:10.1016/j.engfailanal.2014.06.006
- Thai, D. K., Kim, S. E., & Bui, T. Q. (2018). Modified empirical formulas for predicting the thickness of RC panels under impact loading. *Construction and Building Materials*, *169*, 261-275. doi:10.1016/j.conbuildmat.2018.02.211
- Triantafillou, T. (2010). Innovative Textile-Based Composites for Strengthening and Seismic Retrofitting of Concrete and Masonry Structures. *Advances in Frp Composites in Civil Engineering*, 3-12.
- TS500. (2000). Requirements for Design and Construction of Reinforced Concrete Structures. In. Ankara, Turkey.
- Tzoura, E., & Triantafillou, T. C. (2016). Shear strengthening of reinforced concrete T-beams under cyclic loading with TRM or FRP jackets. *Materials and Structures*, *49*(1-2), 17-28. doi:10.1617/s11527-014-0470-9
- Vasudevan, A. K. (2012). *Finite element analysis and experimental comparison of doubly reinforced concrete slabs subjected to blast loads* (Master's Thesis), University of Missouri, Kansas City, MO.

- Xiao, Y., Li, B., & Fujikake, K. (2016). Experimental Study of Reinforced Concrete Slabs under Different Loading Rates. *Aci Structural Journal*, 113(1), 157-168.
- Xiao, Y., Li, B., & Fujikake, K. (2017). Behavior of Reinforced Concrete Slabs under Low-Velocity Impact. *Aci Structural Journal*, 114(3), 643-658. doi:10.14359/51689565
- Yasayanlar, Y. (2015). *Impact Resistance of Steel Fiber Reinforced Concrete Slabs*. (Master's Thesis), Izmir Institute of Technology, Izmir, Turkey.
- Yilmaz, T., Kirac, N., Anil, O., Erdem, R. T., & Sezer, C. (2018). Low-velocity impact behaviour of two way RC slab strengthening with CFRP strips. *Construction and Building Materials*, 186, 1046-1063. doi:10.1016/j.conbuildmat.2018.08.027
- Zukas, J. A. (2004). *Introduction to Hydrocodes*: Elsevier.

## APPENDIX A

### THE CRACK PROFILES OF THE TEST SPECIMENS

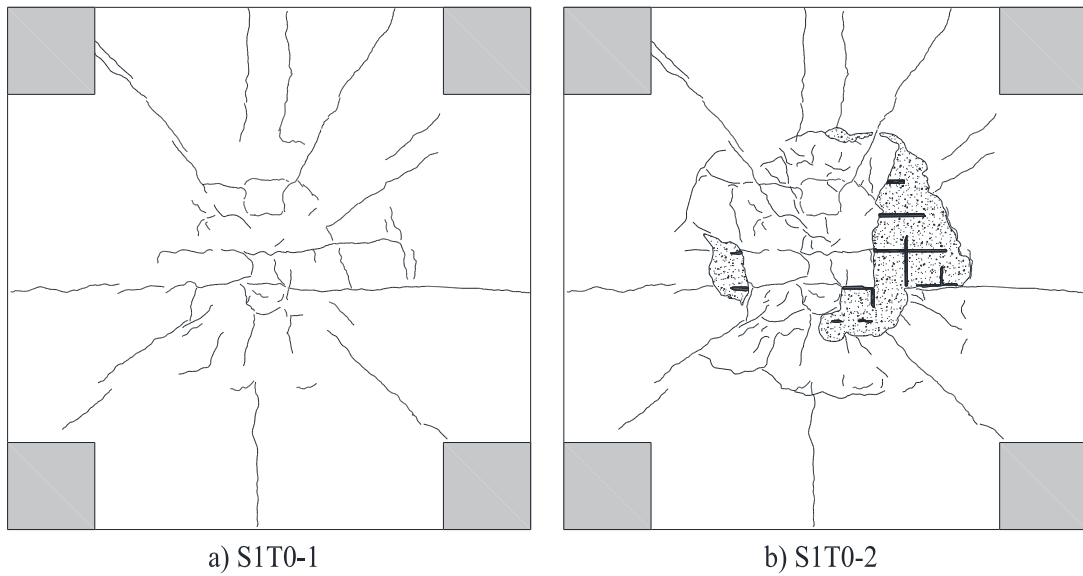


Figure A.1. S1T0 specimen bottom face crack profiles for each impact event

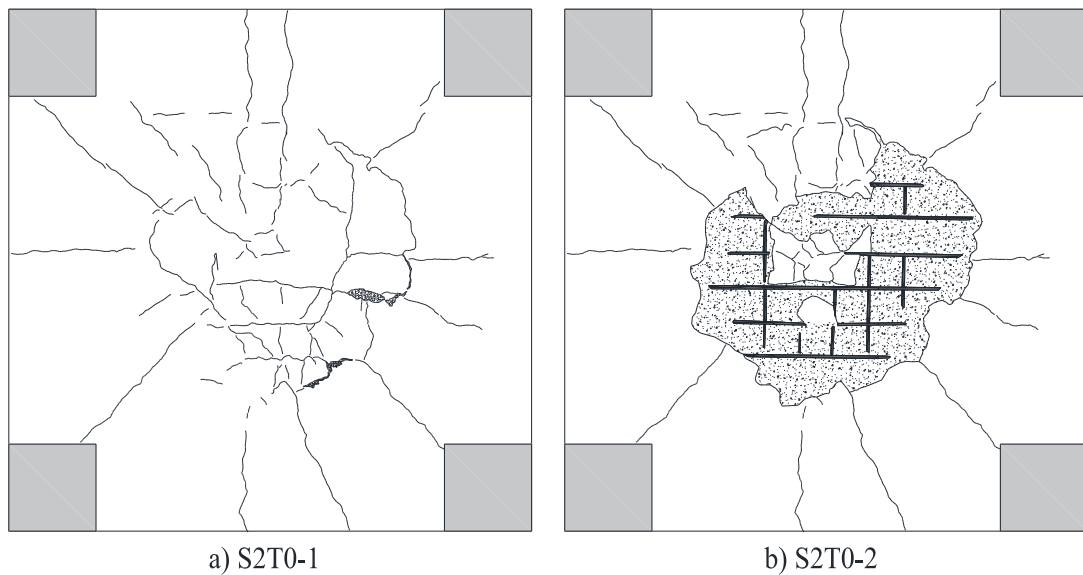


Figure A.2. S2T0 specimen bottom face crack profiles for each impact event

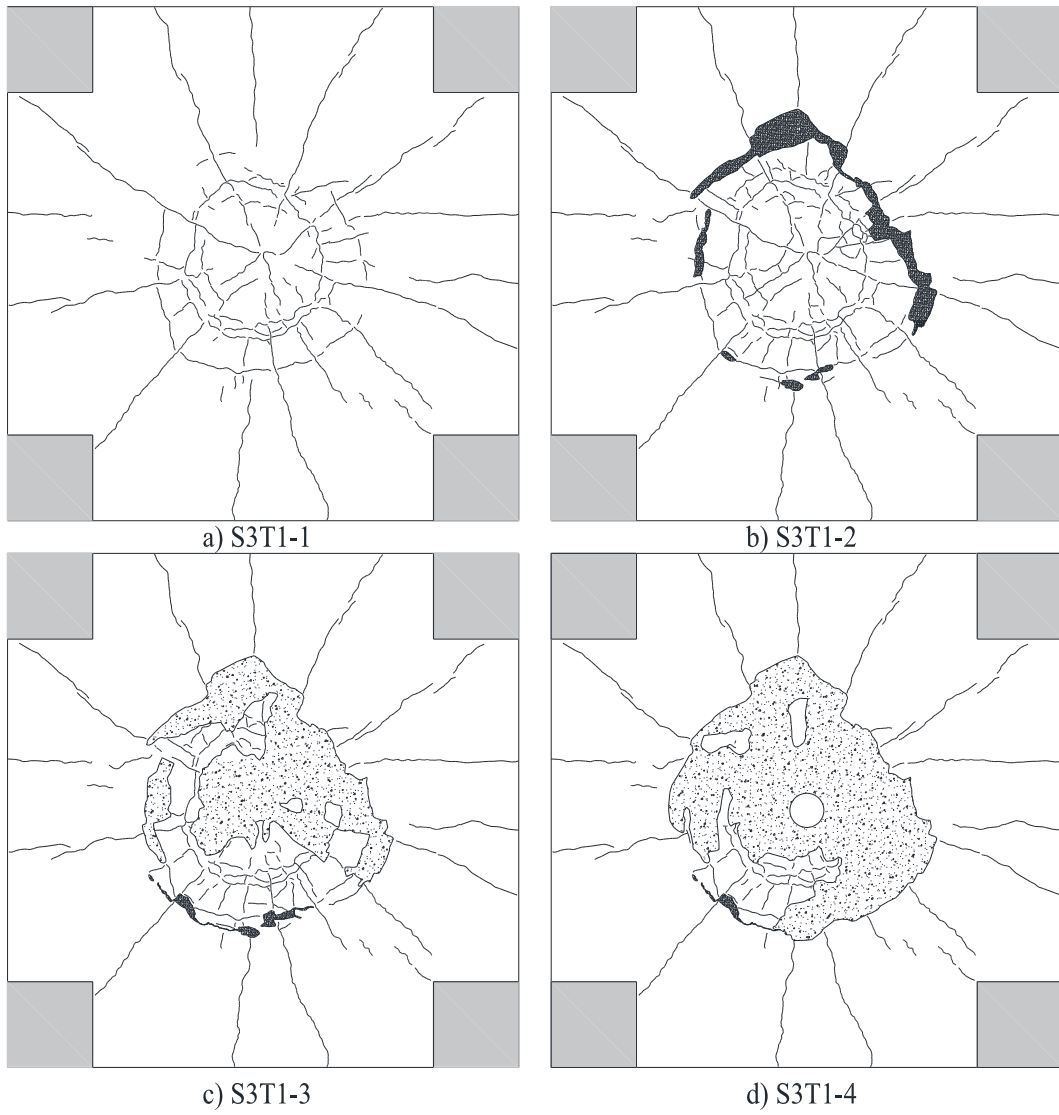


Figure A.3. S3T1 specimen bottom face crack profiles for each impact event

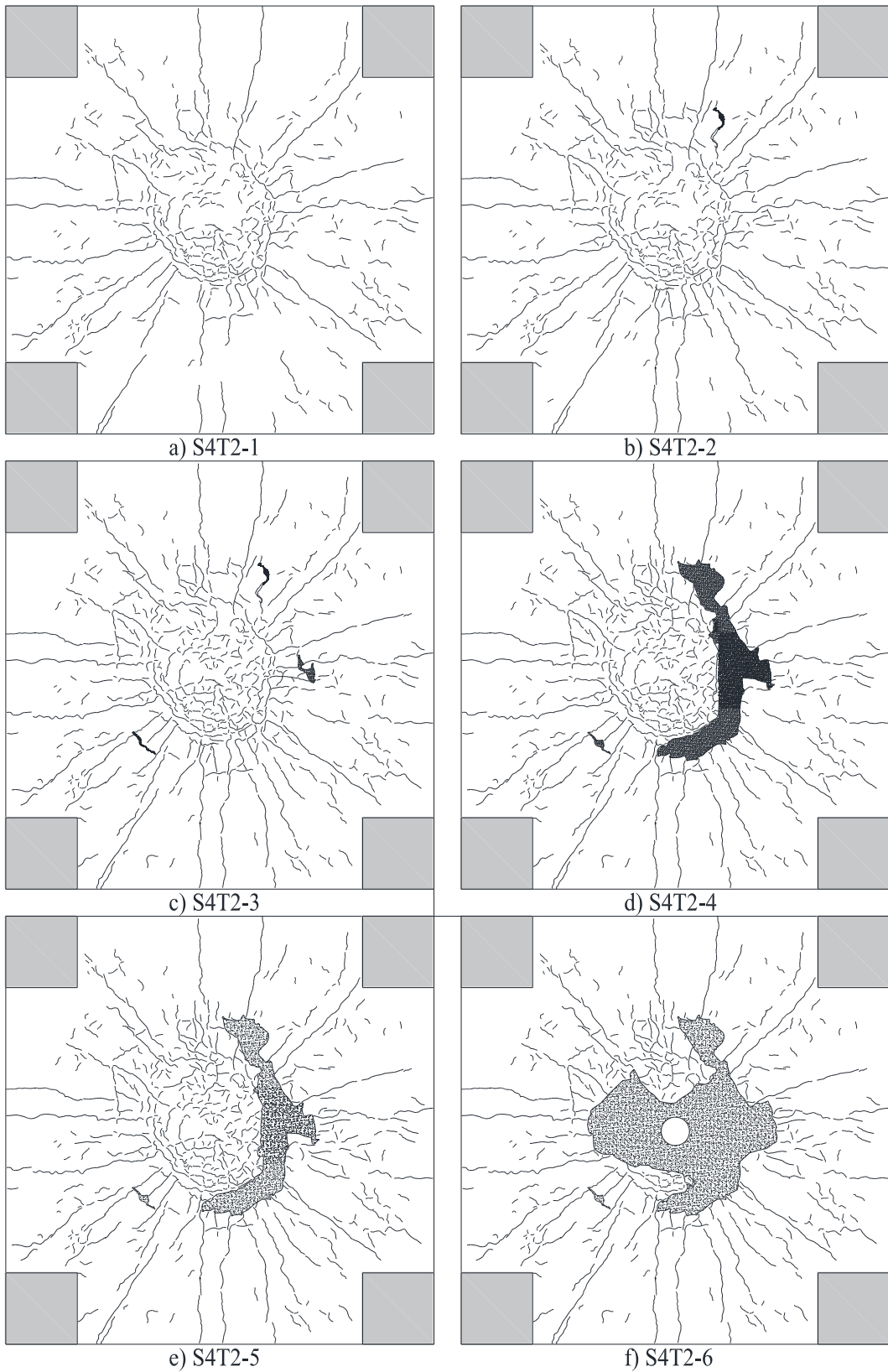


Figure A.4. S4T2 specimen bottom face crack profiles for each impact event

## APPENDIX B

### THE THEORETICAL STATIC CAPACITIES OF SLABS

To identify the failure mechanisms of the slab specimens under static loading conditions, the theoretical flexural and punching capacities of the specimens are required to be calculated. For this purpose, the patterns of yield line mechanisms for the flexural capacity examined. Additionally, the punching load capacities were calculated according to the Turkish (TS500-2000), American (ACI 318-19), European (EC2) and, Canadian (CSA A23.3-04) standards.

#### B.1. Yield Line Mechanisms

With the intent to obtain possible collapse mechanisms of the slab specimens with the compatible boundary conditions, three most likely collapse patterns were examined on the grounds of the virtual work method. These patterns were used to identify the most critical patterns for each slab specimen.

i. **Pattern#1**

Pattern#1 is assumed to be governed in the slab specimens by applying a point load at the midpoint, and the yield lines are expected to develop from the center to the free edges along the middle axes, as presented in Figure B.1. When the virtual work principles are applied by using the ultimate moment capacity in positive,  $M_u$ , the applied load,  $P$ , and the virtual displacement,  $\delta$ , the relations are calculated by using Eq. B.1 and Eq.B.2.

$$P\delta = 2[2M_u L] \frac{\delta}{L/2} \quad \text{B.1}$$

$$P = 8M_u \quad \text{B.2}$$

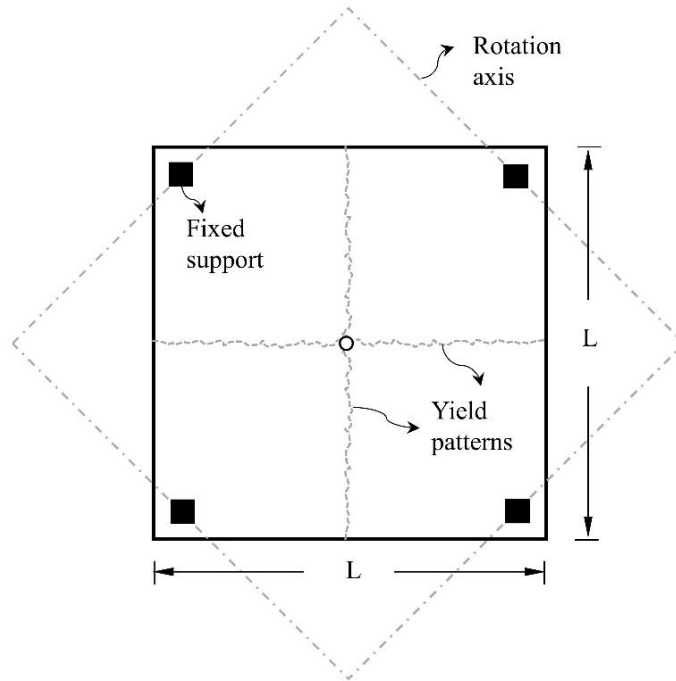


Figure B.1. Yield line mechanism - Pattern#1

ii. **Pattern#2**

Another mechanism formed under point load is presented in Figure B.2. It should be noted here that the ultimate moment capacities of the sections in negative,  $M'_u$ , and positive,  $M_u$ , are not identical due to the asymmetrical reinforcements in the slab sections. The calculated relations were given from Eq. B.2. to Eq. B.4.

$$M_u \neq M'_u \quad \text{B.2}$$

$$P\delta = 2[2M'_u + 4M_u]L \frac{\delta}{L} \quad \text{B.2}$$

$$P = 4M'_u + 8M_u \quad \text{B.3}$$

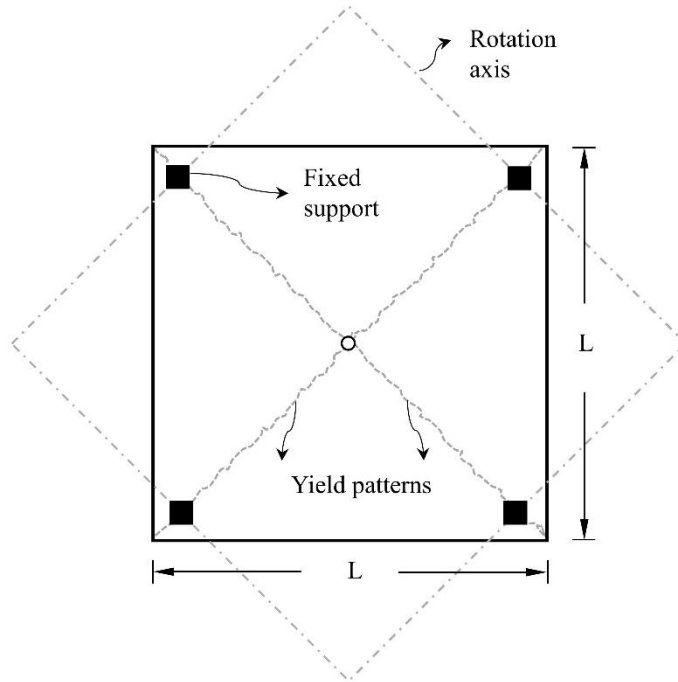


Figure B.2. Yield line mechanism - Pattern#2

iii. **Pattern#3**

The last examined pattern is formed by applied point load at the middle and the radial yield lines are expected to be governed (Figure B.3). Similar to the previous pattern, the moments in positive and negative are not equal to each other due to the asymmetric reinforcement in the sections. The obtained relations are presented from Eq.B.4 to Eq.B.6.

$$M_u \neq M'_u \quad \text{B.4}$$

$$P\delta = [M'_u + M_u]2\pi r \frac{\delta}{r} \quad \text{B.5}$$

$$P = 2\pi[M'_u + M_u] \quad \text{B.6}$$

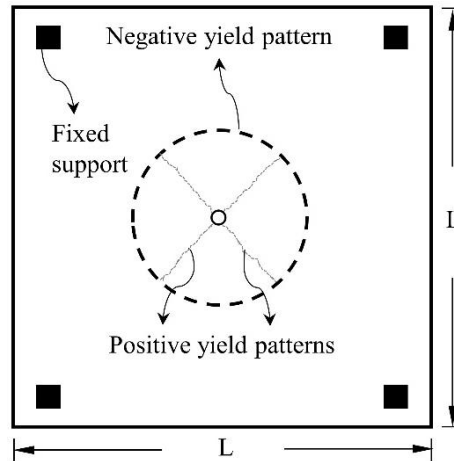


Figure B.3. Yield line mechanism - Pattern#3

As mentioned previously, all patterns were examined for each slab specimen and the most critical patterns were selected as the governing yield pattern. The calculated capacities and the governed yield patterns for the specimens in Family#1 and Family#2 are tabulated in Table B.1. and Table B.2., respectively.

Table B.1. Yield patterns of the specimen in Family#1

Slab	Steel Rebar		Textile reinforcement	Specimen height	Capacity			Yield line pattern
	Rebar	Spacing (mm)	Spacing (mm)	H (mm)	$M_u^*$ (kN.m)	$M_u^\dagger$ (kN.m)	$F_u$ (kN)	
S100T12H220			12		48	127	1016	Pattern#1
S100T16H220	Φ8	100	16	220	48	106	848	Pattern#1
S100T25H220			25		48	84	672	Pattern#1
S150T12H220			12		33	114	912	Pattern#1
S150T16H220	Φ8	150	16	220	33	92	736	Pattern#1
S150T25H220			25		33	70	560	Pattern#1
S200T12H220			12		25	107	829	Pattern#3
S200T16H220	Φ8	200	16	220	25	85	680	Pattern#1
S200T25H220			25		25	63	504	Pattern#1

\*  $M_u^*$  indicates negative moment; †  $M_u^\dagger$  indicates positive moment

Table B.2. Yield patterns of the specimen in Family#2

Slab	Steel Rebar		Textile reinforcement	Specimen height	Capacity			Yield line pattern
	Rebar	Spacing (mm)	Spacing (mm)	H (mm)	$M_u^*$ (kN.m)	$M_u^\dagger$ (kN.m)	$F_u$ (kN)	
S100TnoH80	Φ6	100	-	80	10	10	78	Pattern#1
S100T10H80			10		42	325	Pattern#3	
S150TnoH80	Φ6	150	-	80	7	7	55	Pattern#1
S150T10H80			10		36	272	Pattern#3	
S200TnoH80	Φ6	200	-	80	5	5	42	Pattern#1
S200T10H80			10		32	231	Pattern#3	

\*  $M_u^*$  indicates negative moment; †  $M_u^\dagger$  indicates positive moment

## B.2. Ultimate Punching Capacity

The ultimate punching capacities of the specimens were calculated by using the provisions of the four design codes, Turkish (TS500), American (ACI 318-19), European (EC2) and, Canadian (CSA A23.3-04) standards. To calculate ultimate punching capacities, the required geometrical properties of the slab sections are presented in Figure B.4. Additionally, assumed control perimeters according to each code are depicted in Figure B.5. It should be noted here that the calculation steps of the required parameters of the equivalent effective depth,  $d_{eqv}$ , and the equivalent reinforcement ratio,  $\rho_{eqv}$ , are presented in Chapter 6.

As a representative example, the calculation steps for each code are presented for only the S100T25H220 slab specimen.

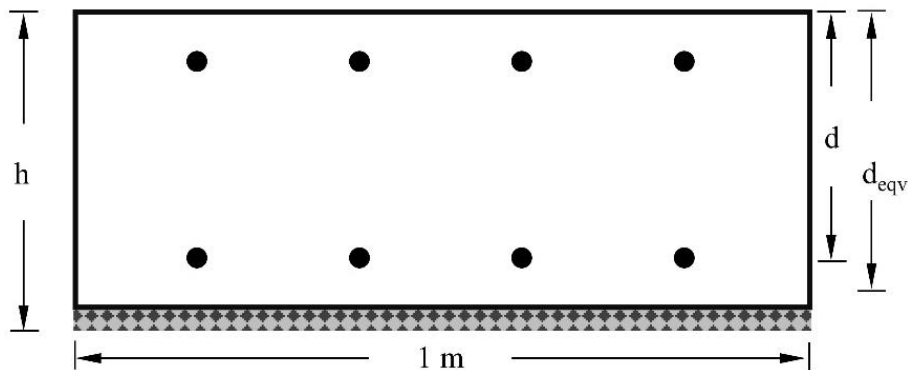


Figure B.4. Unit strip illustration for a strengthened RC slab

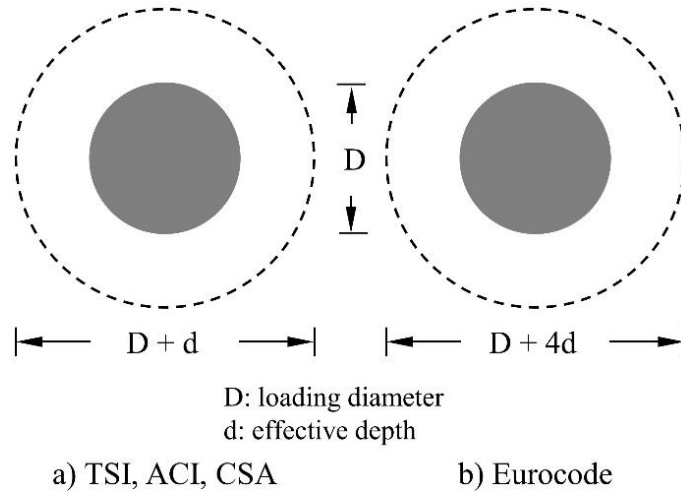


Figure B.5. Control perimeters according to the design codes

### B.2.1. TS500 (Turkish Standards Institution, 2000)

The ultimate punching capacity of a member is expressed by Turkish Standards as given in B.7 and B.8. By using these calculations, the ultimate punching capacity was obtained in Eq.B.9.

$$V_{pr} = f_{ctd} U_p d \quad \text{B.7}$$

$$f_{ctk} = 0.35 \sqrt{f_{ck}} \quad \text{B.8}$$

where;

$f_{ctd}$ : design tensile strength of concrete in MPa

$U_p$ : control perimeter

$f_{ck}$ : characteristic compressive strength of concrete in MPa

$d$ : effective depth of slab

$$V_{pr} = 0.35 \sqrt{33} \pi (292) 192 = 354 \text{ kN} \quad \text{B.9}$$

### B.2.2. EUROCODE 2 (European Committee for Standardization, 2004)

Unlike the other presented codes, Eurocode2 is the only one that takes the reinforcement ratio into account. Additionally, the control perimeter of the section is

higher than the other codes. The calculation steps from Eurocode2 are presented from Eq.B.10 to Eq.B.16.

$$V_{Rd,c} = 0.18k(100\rho f_{ck})^{1/3} b_0 d \geq v_{min} b_0 d \text{ kN} \quad \text{B.10}$$

where;

$\rho$ : flexural reinforcement ratio,  $\rho \leq 0.02$

$b_0$ : control perimeter

$f_{ck}$ : characteristic compressive strength of concrete in MPa

$d$ : effective depth of slab

$k$ : size effect factor

$$k = 1 + \sqrt{\frac{200}{d}} \leq 2.0 \quad \text{B.11}$$

$$v_{min} = 0.0035k^{3/2} f_c^{1/2} \quad \text{B.12}$$

$$k = 1 + \sqrt{\frac{200}{192}} \leq 2.0 \therefore k = 2.0 \quad \text{B.13}$$

$$v_{min} b_0 d = 0.0035(2^{3/2})33^{1/2}(\pi 868)(192) = 29.8 \text{ kN} \quad \text{B.14}$$

$$\rho = \rho_{eqv} = 0.0046 \quad \text{B.15}$$

$$V_{Rd,c} = 0.18(2)((100)(0.0045)(33))^{1/3}(\pi 868)(192) = 460 \geq 29.8 \text{ kN} \quad \text{B.16}$$

### **B.2.3.ACI 318M-19 (American Concrete Institute, 2019)**

The ultimate punching capacity of a section is expressed as three different equations in American Standards. The smallest value from these equations should be assigned as the ultimate punching capacity. These equations are presented from Eq.B.17 to Eq.B.19. By applying the Eq. B.20 and B.21 into these equations, the ultimate punching capacity of the given section selected from Eq.B.22 to Eq. B.24.

$$V_c = 0.33\lambda_s\lambda\sqrt{f'_c}b_0d \quad \text{B.17}$$

$$V_c = \left(0.17 + \frac{0.33}{\beta}\right)\lambda_s\lambda\sqrt{f'_c}b_0d \quad \text{B.18}$$

$$V_c = \left(0.17 + \frac{0.083\alpha_s d}{b_0}\right)\lambda_s\lambda\sqrt{f'_c}b_0d \quad \text{B.19}$$

where;

$\lambda$ : modification factor to reflect the reduced mechanical properties of lightweight concrete relative to normal weight concrete of the same compressive strength

$\lambda_s$ : factor used to modify shear strength based on the effects of member depth, commonly referred to as the size effect factor

$f'_c$ : compressive strength of concrete in MPa

$b_0$ : control perimeter

$d$ : effective depth of slab

$\beta$ : ratio of long to short dimensions

$\alpha_s$ : constant value (the value of  $\alpha_s$  is 40 for interior columns, 30 for edge columns, and 20 for corner columns)

$$\lambda_s = \sqrt{\frac{2}{1 + 0.004d}} \leq 1.0 \quad \text{B.20}$$

$$\lambda_s = \sqrt{\frac{2}{1 + 0.004(192)}} \leq 1.0 \therefore \lambda_s = 1.0 \quad \text{B.21}$$

$$V_c = 0.33(1)(1)\sqrt{33}(\pi 292)(192) = 334 \text{ kN} \quad \text{B.22}$$

$$V_c = \left(0.17 + \frac{0.33}{1}\right)(1)(1)\sqrt{33}(\pi 292)(192) = 506 \text{ kN} \quad \text{B.23}$$

$$V_c = \left(0.17 + \frac{0.083(40)(192)}{\pi(292)}\right)(1)(1)\sqrt{33}\pi(292)(192) = 875 \text{ kN} \quad \text{B.24}$$

#### B.2.4.CSA A23.3-04 (Canadian Standards Association, 2004)

Similar to American Standards, the ultimate punching capacity of a section should be selected as the minimum of the equations given from Eq.B.25 to Eq.B.27. By applying Eq.B.28 and Eq.B.29, the ultimate punching capacity was obtained as the minimum of Eq.B.30, Eq.B.31, and Eq.B.32.

$$V_c = 0.38\lambda\phi_c\sqrt{f'_c}b_0d \quad \text{B.25}$$

$$V_c = \left(1 + \frac{2}{\beta_c}\right)0.19\lambda\phi_c\sqrt{f'_c}b_0d \quad \text{B.26}$$

$$V_c = \left(\frac{\alpha_s d}{b_0} + 0.19\right)\lambda\phi_c\sqrt{f'_c}b_0d \quad \text{B.27}$$

where;

$\lambda$ : factor to account for low-density concrete

$\phi_c$ : resistance factor for concrete

$f'_c$ : compressive strength of concrete in MPa

$b_0$ : control perimeter

$d$ : effective depth of slab

$\alpha_s$ : factor that adjusts  $V_c$  for support dimensions

$\beta_c$ : ratio of long side to short side of the column (Eq. B.28 for section with no transverse reinforcement)

$$\beta_c = \frac{230}{1000 + d} \quad \text{B.28}$$

$$\beta_c = \frac{230}{1000 + 192} = 0.193 \quad \text{B.29}$$

$$V_c = 0.38(1)(1)\sqrt{33}\pi(292)(192) = 385 \text{ kN} \quad \text{B.30}$$

$$V_c = \left(1 + \frac{2}{0.193}\right)0.19(1)(1)\sqrt{33}\pi(292)(192) = 2185 \text{ kN} \quad \text{B.31}$$

$$V_c = \left(\frac{(1)(192)}{\pi(292)} + 0.19\right)(1)(1)\sqrt{33}\pi(292)(192) = 404 \text{ kN} \quad \text{B.32}$$

The calculations steps for the ultimate punching capacity of the S100T25H220 specimen are only presented as a representative in this section. To obtain the ultimate capacities of the specimens created for the parametric study, a simple code was written in the MATLAB software. The equivalent reinforcement ratios and the equivalent effective depths of these specimens are presented in Table B. and Table B.. The calculated ultimate moment capacities of the specimens by using the method explained in Chapter 6 can be found in Table B. and Table B. as well.

Table B.3. The calculated parameters for the specimen in Family#1

Specimen	$\rho_{eqv}$	$d_{eqv}$	Moment capacity $M_u$ (kN.m)
S100T12H220	0.0064	201	127
S100T16H220	0.0055	198	106
S100T25H220	0.0045	192	84
S150T12H220	0.0055	206	114
S150T16H220	0.0046	203	92
S150T25H220	0.0036	197	70
S200T12H220	0.0050	208	108
S200T16H220	0.0038	204	85
S200T25H220	0.0032	201	63

Table B.4. The calculated parameters for the specimen in Family#2

Specimen	$\rho_{eqv}$	$d_{eqv}$	Moment capacity $M_u$ (kN.m)
S100TnoH80 <sup>†</sup>	0.0042	67	10
S100T10H80	0.0132	70	42
S150TnoH80 <sup>†</sup>	0.0028	67	7
S150T10H80	0.0102	72	36
S200TnoH80 <sup>†</sup>	0.0021	67	5
S200T10H80	0.0094	74	32

<sup>†</sup> Tno indicates the specimen without textile reinforcement